UNIVERSITA' DEGLI STUDI DI MILANO-BICOCCA

Doctorate in Materials Science

XXVII Cycle:

NOVEL APPROACHES TO SOLUTION-PROCESSABLE ORGANIC ELECTRONICS

Ph.D. Thesis of

Riccardo TURRISI

Tutor: Prof. Luca BEVERINA

Supervisor: Prof. Antonio Facchetti

March 2015

Table of Contents

hapter I:

Introduction

It was December the 23rd, 1947. It probably was not a dark and thunderous night. Probably it was not a night at all. Nonetheless, the stuff of which science fiction is made of was being cut and sewn into a new set of shiny clothes. That was the night (*the day*, more likely) which showed for the first time a working model of a transistor. Quite the Christmas present. This piece of technology, the heart and pulse of all logic circuitry, was first realized in the Bell Labs by Walter Houser Brattain and William Bradford Shockley. In 1956 these two fine gentlemen, together with John Bardeen, were awarded a Nobel prize in Physics "for their researches on semiconductors and their discovery of the transistor effect". Their seminal research allowed for the blooming of countless new applications, starting from new physics and electrical engineering and ending with the invention of circuitry logic.

Lots of things have happened since. Wars, mainly, and the end of wars. But also the invention of the first transistorized computer, in 1953, were the ubiquitous, bulky and sometimes unreliable vacuum tubes (which exploited thermionic effect as a source of current and metallic grids as current amplifiers) were substituted by silicon dioxide transistors. It was the birth of the silicon era, which ultimately led to the current state of electronics we are witnessing, the invention of smartphones and Facebook, and several generations of materials scientists who spent their careers trying to find alternatives to this overexploited material [just to be greeted by the recently ubiquitous graphene… but that's another story].

Dark and gloomy as this introduction may seem, our understanding of transistors and their inner workings has increased exponentially throughout the years. The continuous race towards miniaturization has led to nanoarchitectures which have greatly increased the number of transistor density on a single processor.

The history of computing was successfully prophesized by the empirical (in)famous Moore's law:

"The complexity for minimum component costs has increased at a rate of roughly a factor of two per year. Certainly over the short term this rate can be expected to continue, if not to increase. Over the longer term, the rate of increase is a bit more uncertain, although there is no reason to believe it will remain nearly constant for at least 10 years."[1]

As it happens, we are on the fast-track to a plateau on this seemingly linear relation. There is plenty of room at the bottom [cit.], but recent technology development in the area of silicon electronics has brought us to the brink of development sustainability. The continuous scale-down for single elements in processors has almost shrunk to the limit where it cannot be shrunk anymore without seriously affecting the performances of said element.

The need for new technologies in the electronics universe has skyrocketed in the last decades. If one was to neglect the necessity for an increase in sheer calculating power, still there are limitations for silicon-based logic circuitry. One of the most tantalizing promises of electronics is in fact fully-flexible, wearable and transparent logic circuitry. Characteristics which silicon and silicon dioxide, two of the main components of modern era electronics, are blatantly in short supply of.

So, is humankind on the verge of technological stagnancy? So it would seem, unless new processes and new materials are ushered into the limelight by an as-of-now unknown hero of science.

Enters the material scientist.

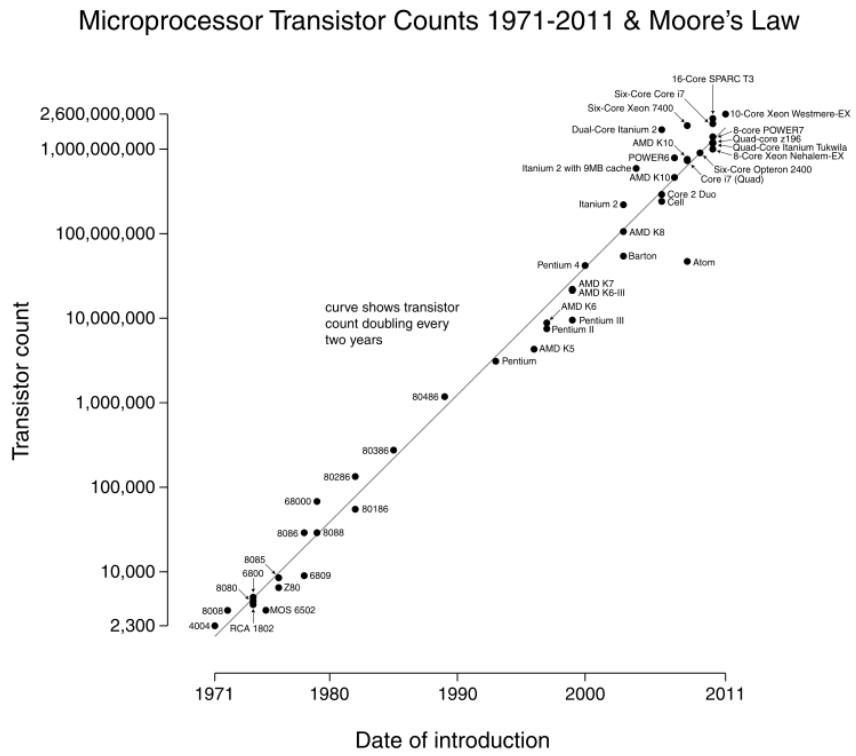

Figure 1: *Plot of CPU transistor counts against dates of introduction. Note the logarithmic vertical scale; the line corresponds to exponential growth with transistor count doubling every two years. Source: Wikimedia Commons.*

This rare and mythological beast, who has spent decades studying books describing every aspect of silicon and its several thousands of applications, can't wait to enter into a new field of technological progress where silicon is not the centerpiece of the collection. Branching out has always been the successful way into life, as evolutional theory clearly proves. One of the possible pathways of evolution of inorganic-based circuitry is the appeal of fully organic, possibly transparent and flexible electronics.

Organic (semi)conductors have been known for more than 150 years. The first report of a conductive material dates back to 1862 by Dr. Henry Letheby, when the anodic oxidation of anilinium sulfate in sulfuric acid yielded the first reproducible blue batch of polyaniline[2] (incidentally, this product was also among the first recognized examples of organic electrochromism. This is what ended up giving aniline its name, which originates from the Spanish *añil*, meaning indigo).

In his book *Conducting Polymers: a New Era in Electrochemistry*, Prof. Gyorgy Inzelt reports that in 1967, when the first report of polyanilines as organic conductors was announced at a ISE conference, the reaction from the scientific public was underwhelming and mild, at best[3]. Long years and a Nobel prize in Chemistry later, the importance of (semi)conductive polymers has been ascertained and new applications are blooming every other day.

In general, the market for organic electronics is ripening and swelling, as can be seen from the projected market analysis of Figure 2. It is a well known fact that sweetest fruits are also the most sought after, and that evolution pushes them to the biggest success (i.e. planting new ideas).

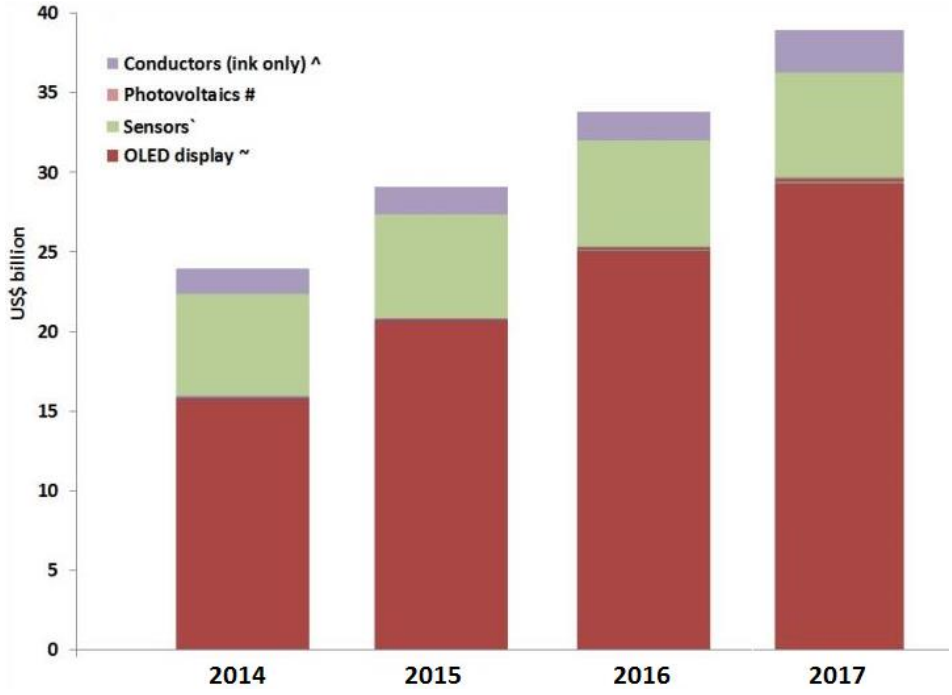

Figure 2: *projected market values for organic electronics in the next few years. Adapted from reference*[4]*.*

The organic electronics market is currently mostly interested in the production of OLED displays, since big players have already entered the field and have commercialized the technology for flat-panel curved displays. Remember, though: the scale of **Figure 2** is measured in billion dollars! Even a 1% increase (as is the case for photovoltaics) accounts for million dollars value. And the author or the institutes he has worked in are not rich enough to afford the hefty 5.000 $ price tag on the full report of reference[4]. It is noted, though, that the market for these applications will expand to almost 74$ billion dollars by 2025, ten years from now.

Those small segments that now are next to invisible will bloom into self-sustained markets with their own niches. Such is the way to technological development, where the need for specificity keens the minds and sharpens wits. It is in this era that research has to take place, tearing down the infamous “red brick walls” on the way to commercial production.

Under this point of view one of the most interesting possibilities is trying to come up with fabrication processes enabling us to get rid of expensive steps requiring expensive equipment. Due to the nature of the components we are willing to use, i.e. soluble organic materials, the fabrication process can be adapted to accommodate solution processing, in one of its many forms.

The laboratory technique to apply a thin film of organic material to a surface is called spin-coating, and consists of a vacuum chuck connected to the substrate. A solution of the desired material is dissolved in the desired solvent and after application of the solvent to the substrate, the substrate is spun at a certain

velocity until the coating is uniform and solvent evaporates. This and solution-grafting are the main techniques used throughout this thesis for solution processing.

This technique has two main disadvantages: the huge waste of often-expensive material (in the 90% range) and the total engineering unfeasibility of a rotative apparatus capable of sustaining the kind of torques which would make large-scale production possible.

Industrial alternatives include some of the following, often applied to roll-to-roll processes: doctorblading, spray-coating, slot-die, inkjet- or gravure- printing.

A brief rundown of these techniques follows:

Doctorblading[5]: basically the technologically-relevant equivalent of knife-spreading. A blade lifted from the surface is moved parallel to the substrate, forming a uniform layer of ink on the surface of the substrate, which dries forming a film on the substrate. Basic parameters are temperature, blade-substrate distance, relative blade-substrate velocity and viscosity of the solution.

Spray-coating[6]: imagine one of those fancy atomizers used for perfumes. Now substitute the perfume with a solution of an optoelectronically relevant component, and your face with a substrate. Propel with a pressurized gas, apply to the surface and serve cold. Contrary to doctorblading, the inks used for spray-coating dry immediately once the droplets hit the surface of the substrate, leading to somehow rougher films. Nonetheless, it is an impressive techniques for applications where surface roughness is not a concern (i.e. bottom-gate, bottom-contact organic field effect transistors[7]).

Slot-die[8]: in this technique a reservoir of ink provides the web of the roll-to-roll process with the material it needs. The presence of a mechanized pump inside the slot head allows for accurate control of deposition; the technique is inherently high-throughput, ranging in the hundreds of roll meters per minute. It is one of the most used coating processes in semi-industrial organic electronics environments.

Inkjet[9]: applying the technology and complexity of desktop inkjet printers to organic electronics has never been easier! Untrue. This technique is one of the most difficult to precisely control, because it heavily relies on the formulation of the ink to be accurate during printing. The shape and position of the drops are drastically controlled by the viscosity, boiling point and surface tension of the ink. The main difference with spray coating is the possibility to print complex patterns by drop-on-demand techniques and/or by electrostatic positioning of the droplets. Used for both organic[10] and inorganic materials[11].

Gravure-printing[12]: normally magazines are printed using gravure-printing processes because of their high reliability, speed and efficiency. The technique consists of two rolls, one of them dipping into the ink reservoir, the other one supporting the web. The former rotates into the ink and fills up the microcavities on its surface with the material while a blade removes the excess ink, whereas the second, softer roll

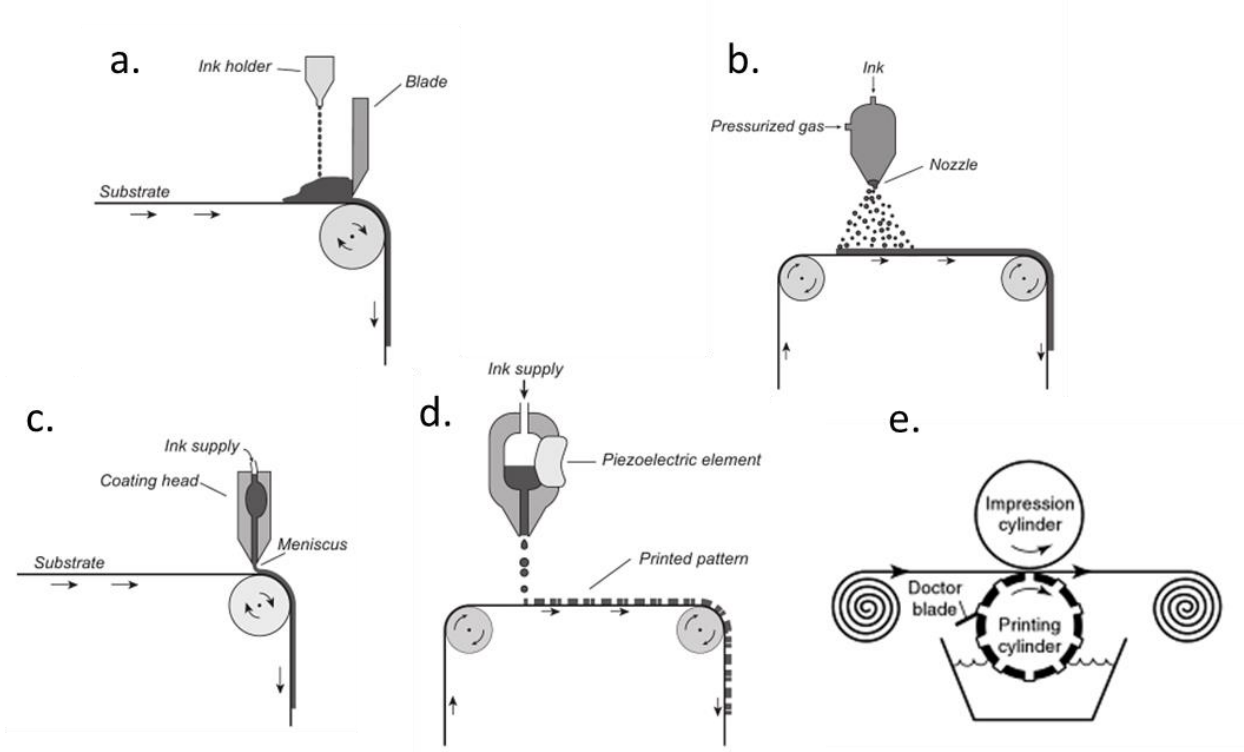

Figure 3: *non-exhaustive list of techniques for printable organic electronics: (a) doctorblading; (b) spraycoating; (c) slot-die coating; (d) inkjet printing; (e) gravure printing. Adapted from references*[12,13].

pushes the web against the pattern of microcavities, transferring the ink from one to the other, as per matching surface energies.

A graphic representation of the techniques is reported in **Figure 3**.

With such a plethora of amazing alternatives, some more performing than others, it is central to be able to obtain reliable and outstanding performances to allow electronics to make the next big step toward new exciting applications.

This thesis has been mainly dedicated to the betterment of existing and well consolidated technologies, which have been reblooming under the *aegis* of organic chemistry. Organic photovoltaic, electronic and photophysic applications are just some of the exciting technologies which we, as a generation, will be lucky to witness.

The span of the author's work experience has been kept as wide as possible, sacrificing the extreme specialization of the nowadays scientist for a wider perspective and a more generous approach to the issues at hand.

Thus, this work will be divided in three chapters: a chapter dealing with photovoltaics and the eternal struggle between polymers and small molecules (Chapter II), a chapter dealing with the shenanigans of self-assembled nanoelectronics and the possibilities hidden therein (Chapter III), and a last chapter dealing with the possibility of new ways to make our solar processes more efficient and our homes more colored (Chapter IV).

The *fil rouge* connecting these chapters is hidden, but hard as steel (red steel, that is): solution processing. All of the technologies analyzed in this thesis are strictly related to the exploitation of a cheap and fast way to fabricate the devices we yearn to control and master.

So our solar cells are solution-processed, our nanodielectric can be fabricated entirely from solution, and the solar concentrators can be cast from a liquid precursor, only requiring a bit of heat and a sprinkle of magic dust - AIBN.

Buckle up.

BIBLIOGRAPHY

(1) Moore, G. E. *Electron. Mag.* **1965**, *86*, 4.

(2) Letheby, H. *J. Chem. Soc.* **1862**, 161.

(3) Inzelt, G. *Conducting Polymers: a New Era in Electrochemistry*; 1st ed.; Springer Berlin Heidelberg, 2008; p. 282.

(4) Harrop, P.; Das, R. Printed, Organic & Flexible Electronics Forecasts, Players & Opportunities 2015-2025 http://www.idtechex.com/research/reports/printed-organic-and-flexible-electronics-forecasts-players-and-opportunities-2015-2025-000425.asp?viewopt=desc (accessed Feb 3, 2015).

(5) Padinger, F.; Brabec, C. J.; Fromherz, T.; Hummelen, J. C. *Opto-Electronics Rev.* **2000**, *8*, 280.

(6) Vak, D.; Kim, S.-S.; Jo, J.; Oh, S.-H.; Na, S.-I.; Kim, J.; Kim, D.-Y. *Appl. Phys. Lett.* **2007**, *91*, 081102.

(7) Yu, X.; Zhou, N.; Han, S.; Lin, H.; Buchholz, D. B.; Yu, J.; Chang, R. P. H.; Marks, T. J.; Facchetti, A. *J. Mater. Chem. C* **2013**, *1*, 6532.

(8) Sandström, A.; Dam, H. F.; Krebs, F. C.; Edman, L. *Nat. Commun.* **2012**, *3*, 1002.

(9) Teichler, A.; Perelaer, J.; Schubert, U. S. *J. Mater. Chem. C* **2013**, *1*, 1910.

(10) Basirico', L. Inkjet Printing of Organic Transistor Devices http://www.diee.unica.it/DRIEI/tesi/24_basirico.pdf (accessed Feb 4, 2015).

(11) Hennek, J. W.; Xia, Y.; Everaerts, K.; Hersam, M. C.; Facchetti, A.; Marks, T. J. *ACS Appl. Mater. Interfaces* **2012**, *4*, 1614.

(12) Klauk, H. *Organic Electronics II: More Materials and Applications*; John Wiley & Sons, 2012; p. 440.

(13) Logothetidis, S. *Handbook of Flexible Organic Electronics: Materials, Manufacturing and Applications*; Elsevier Science, 2014; p. 478.

Chapter II:

Functional photoresists for photovoltaic applications based on photopolymerizable squaraine compounds

THEORETICAL INTRODUCTION

Solar light is doubtlessly an ideal source of energy. The flux of electromagnetic radiations hitting the Planet's surface could cover 10.000 times the total energy need of our society. Moreover, solar light is found anywhere, is free and not susceptible to exploitation. Such an eagerness towards a sustainable way of life on our planet engendered different ways to harvest the same resource. This is how different kind of technologies to achieve the same goal were born.

Despite their differences, though, a common thread explains why and how solar cells work: p-n junctions. In a quantistical, nearly free-electron framework, total electron energy can be derived using Schroedinger equation

$$\hat{H}\Psi(\vec{r}) = E\Psi(\vec{r}),$$

where $\hat{H}$ is the electron hamiltonian, Ψ the electron wavefunction and E the electron total energy.

$\hat{H}$ comprises two distinct contributes: the kinetic energy K and the potential energy V(*r*), such that

$$\hat{H} = K + V(\vec{r}) = -\frac{\hbar}{2m}\vec{\nabla}^2 + V(\vec{r})$$

In a reciprocal lattice, where V(*r*) must be periodical with

$$\vec{R} = \vec{a}n_1 + \vec{b}n_2 + \vec{c}n_3$$

where a, b, c are the periodic cell dimensions and n_1, n_2, n_3 are positive or negative integers, the potential derived from the fixed charges of the lattice can be written as a Fourier series

$$V(\vec{r}) = \sum_{\vec{G}} V_{\vec{G}}\, e^{i\vec{k}\cdot\vec{r}}$$

where *G* is a vector of the reciprocal lattice. In the case of a cubic lattice, *a*=*b*=*c*= A. The wavefunction Ψ can be written as a linear combination of plane waves

$$\Psi = \sum_{\vec{k}} C_{\vec{k}}\, e^{i\vec{k}\cdot\vec{r}}$$

which expresses a complete set of solutions starting from free-electron ones. We can substitute V and Ψ inside Schoedinger equation to afford

$$\left(\frac{\hbar^2 k^2}{2m} - E\right) C_{\vec{k}} - \sum_{\vec{G}} V_{\vec{G}}\, C_{\vec{k}-\vec{G}}$$

a condition that binds *k*-th coefficients to their (*k*-*G*)-th counterparts. Since *G* must obey to the Born-Von Karman conditions of periodicity, the only values for which such a equation remains valid are inside the first Brillouin zone (FBZ), *i.e.* –π/A < *k* < +π/A.

The original problem is now split in N different problems, where N is the number of cells in a finite solid matrix. Each of these problems can be solved using

$$\Psi_{\vec{k}} = \sum_{\vec{G}} C_{(\vec{k}-\vec{G})}\, e^{i(\vec{k}-\vec{G})\cdot\vec{r}} = \sum_{\vec{G}} C_{(\vec{k}-\vec{G})}\, e^{-i\vec{G}\cdot\vec{r}} e^{i\vec{k}\cdot\vec{r}} = u_{\vec{k}}(\vec{r}) e^{i\vec{k}\cdot\vec{r}}$$

The ansatz to this problem can then be written as a periodical part u_K with the same periodicity of the lattice, modulated by a plane wave $e^{ik\cdot r}$. This is called Bloch's Theorem and shows the basic form of electronic wavefunctions in a periodical medium.

Since we are considering a vanishing potential (nearly-free electrons framework), the dispersion relations are simple free-electrons parabolas: $E=\hbar^2k^2/2m$.

Due to energy periodicity in the whole (supposedly perfect!) solid, $E(k)=E(k+G)$. It is thus possible to reduce all of the free-electrons parabolas inside the FBZ in the operation called "Reduction to the FBZ".

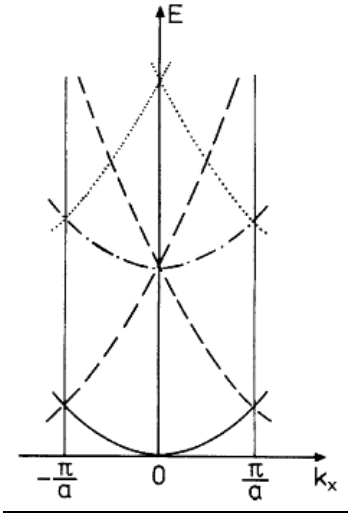

***Figure 4**: a monodimensional reduced FBZ energy depiction. Solid line describes the first parabola. Dashed and dotted lines represent parabolas from nearby Brillouin zones entering the FBZ.*

These waves suffer from Bragg's reflection. In fact, on the FBZ border the condition for Bragg's reflection is satisfied (*i.e. k=G/2*). Considering just one dimension, a superposition of these 2 different waves yields:

$$\Psi_{+} = e^{iGx/2} + e^{-iGx/2} \propto \cos\left(\frac{\pi x}{a}\right)$$

$$\Psi_{-} = e^{iGx/2} + e^{-iGx/2} \propto \sin\left(\frac{\pi x}{a}\right)$$

Remembering that electron density can be evaluated by calculating $|\Psi|^2=\Psi^*\Psi$ (where * denotes the complex conjugate), result is depicted in **Figure 5.** This clearly shows how $|\Psi+|^2$ allows for the building of a charge density close to the ions (lowering overall energy), while $|\Psi-|^2$ does the opposite, building charge where it cannot be stabilized.

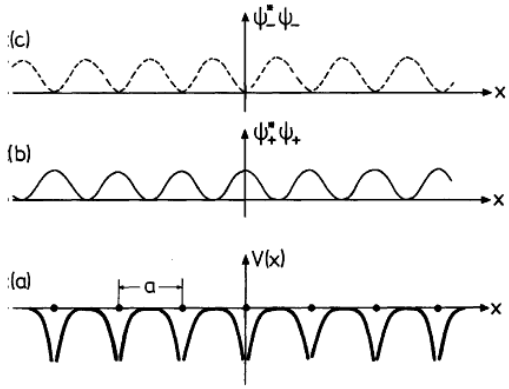

***Figure 5:** (**a**) ion-generated potential in a periodical lattice; (**b**) and (**c**): electronic density distribution for Ψ+ and Ψ-, respectively.*

This is a qualitative discussion of the reasons why an energy gap is generated. This is a central concept to the entire semiconductor physics upon which photovoltaic rests. In first approximation, we can write

$$V(r) = \sum_{\vec{G}} V_{(\vec{G})}\, e^{i\vec{G}\cdot\vec{r}} = V_0 + V_1 e^{i\frac{2\pi}{a}x} + V_{-1} e^{-i\frac{2\pi}{a}x} = V_0 + 2V_1 \cos\left(\frac{2\pi}{a}x\right)$$

In an attempt to deduce the energy difference for an electron described by $|\Psi+|^2$ and one described by $|\Psi-|^2$ with respect to a vanishing V_0 potential, we obtain:

$$\Delta E = \left\langle \Psi_- \middle| 2V_1 \cos\left(\frac{2\pi}{a}x\right) \middle| \Psi_- \right\rangle - \left\langle \Psi_+ \middle| 2V_1 \cos\left(\frac{2\pi}{a}x\right) \middle| \Psi_+ \right\rangle$$

Carrying out the (limited) algebra contained within such a calculation, one can obtain $\Delta E=2V_1$. This shows how, on the zone border, Bragg's reflection opens up a gap (**Figure 6**).

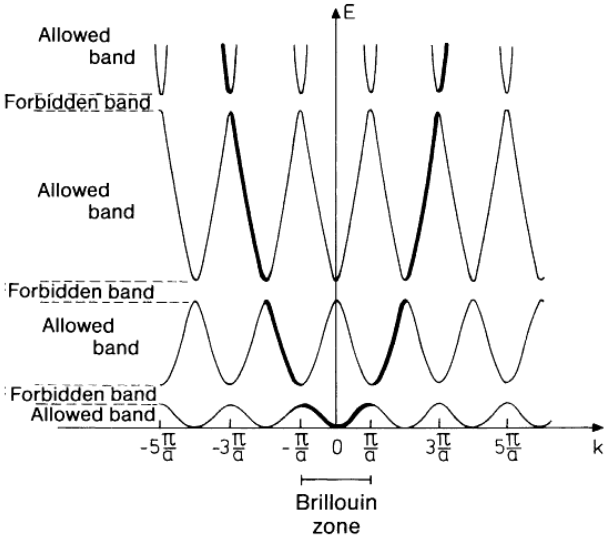

***Figure 6:** extended zone scheme of energy dispersion curves for a monodimensional lattice of constant a. The bold line shows the free-electron energy levels.*

This causes some energies to be unreacheable by the electrons. The dispersion curves are not continuous anymore and this has severe consequences on optical and electronic properties of materials.

Physical Properties: Semiconductors

The spatial interaction of different electronic orbitals gives rise to a peculiar energy structure which is usually found in solids: band structure. The tight-binding approximation, whose details will not be described here[1], allows for an attentive description of such a phenomenon. Suffice it to say that upon linear combination of atomic orbitals energy levels lose their discrete values and smear out to create a continuous interval of energies whose separation is so small that pure thermal energy allows electrons to switch from one level to another. It is now possible to enforce a distinction between materials based on the structure of the band where their last electron lies.

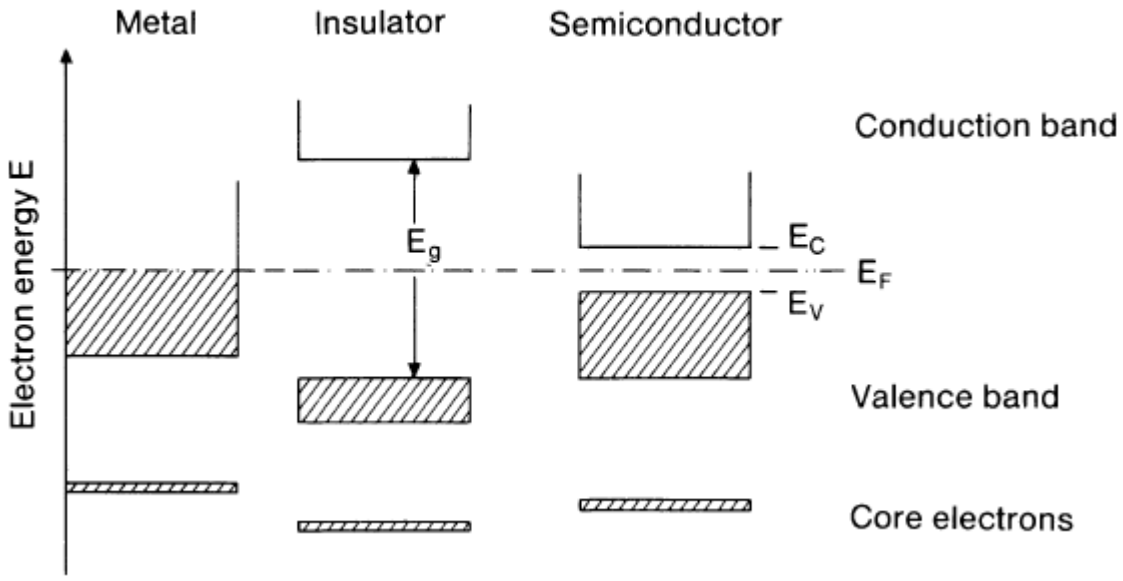

Figure 7: *schematic representation of relative energy levels of metals, insulators and semiconductors.*

It can be shown that full bands do not contribute to current whenever an external electric field is applied to a material[2]. As shown in **Figure 7,** metals do not have a fully occupied band, which causes them to be optimal electricity conductors.

On the other hand, insulators have a very high energy gap ($E_g > 5eV$) and thus the probability for them to thermally excite an electron to the first available energy level is quite small, if not negligible. Semiconductors, theoretically, are insulators with band gaps low enough to allow thermal excitation of electrons to their first unoccupied level (according to Fermi-Dirac distribution). Carriers' density, and therefore resistivity, is thus thermally dependant, ranging from as low as 10^{-6} S/m to as high as 10^{10} S/m.

What happens when a photon strikes a semiconductor? It's just been stated that semiconductors behave as insulators, at low temperatures. This implies that every electron the material must account for will be in the lower energy band (called valence band, VB). Since both energy and momentum must be conserved

in a photon absorption, for an electron to be optically excited to the higher energy band (conduction band, CB), the incident photon's energy must be equal or superior to the semiconductor's energy gap. Photons in the visible region (400 nm < λ < 700 nm) have a negligible momentum k (about 10^{-3} width of the Brillouin zone), so the corresponding electronic transition is "vertical" in an E-vs-k band structure graph (**Figure 8**).

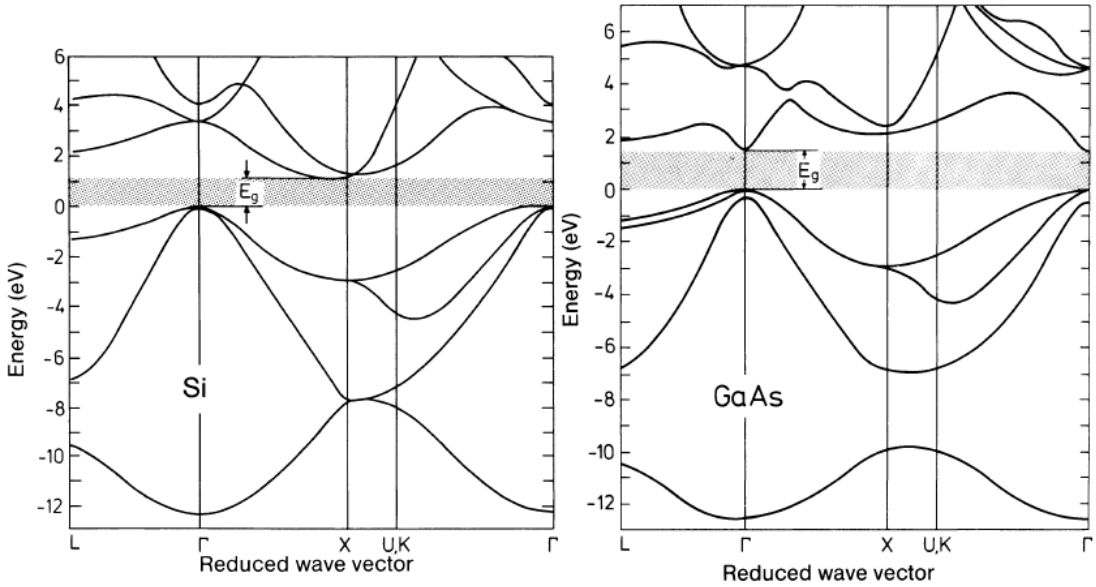

Figure 8: *band structure of an indirect gap semiconductor (Silicon, on the left) and of a direct gap semiconductor (GaAs, on the right).*

Semiconductors can be optically distinguished between direct gap semiconductors (such as GaAs) and indirect gap ones (such as Si or Ge). The difference lies in the k position of the absolute minimum of the conduction band. In the former case the minimum lies vertically above the VB, so a photon whose energy is equal to the band gap can excite an electron to the BC (leaving a hole behind). In the latter case, though, the minimum energy for a transition is not the band gap, because above the VB maximum there's no level where the electron can rest. Absorption in indirect gap semiconductors is thus phonon-assisted, meaning that a 3-bodies process must occur for the photon to be absorbed. In this case the electron is given energy (mainly) by the photon and momentum by the phonon (**Figure 9**).

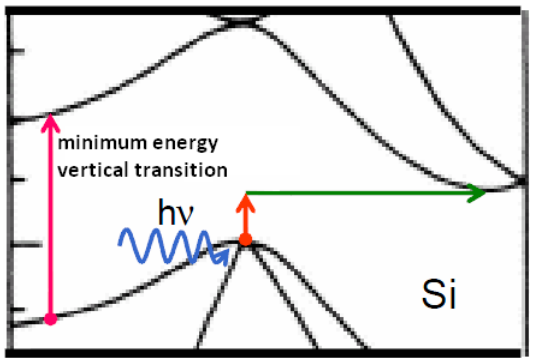

Figure 9: *purple arrow represents the minimum photon energy for a vertical transition. Red arrow shows minimum photon energy for a phonon-assisted transition (phonon is represented by the green arrow).*

The p-n Junction

Once the particular optical and electrical behavior of semiconductors has been explained, the functioning of the p-n junction should seem pretty straight-forward, but for one detail: doping. Dopants are aliovalent impurities whose presence modifies the bulk properties of the undoped solid. The effect of doping is mainly creating additional electronic levels in the energy gap. These levels can either be deep or shallow levels. Whatever they may be (the mathematical approach is profoundly different, though[1]) their effect is to somehow bridge the gap between VB and CB.

This can be done mainly in two ways: n-doping and p-doping. Let's take Silicon as an example. Silicon has 4 electrons in its outer shell, and uses them in a sp^3 hybridization to form 4 bonds with its nearest neighbors. A solid matrix of Silicon doped with a hypovalent impurity like Aluminum will find itself short of an electron. Al atoms, in fact, having only three electrons in its valence levels, will not be able to create four saturated bonds. This is equal to creating a hole in the bulk solid (p-doping) and at the same time allowing Al atoms (acceptors) to charge up negatively. Similarly Phosphor, hypervalent with respect to Silicon, will have a strongly screened excess electron. P atoms will then be easily ionized (donors whose effective charge is +1) and will negatively charge the bulk solid (n-doping). Whenever a p-doped and n-doped Silicon wafers are joined together a non-equilibrium situation arises. Welcome to the magical world of p-n junctions.

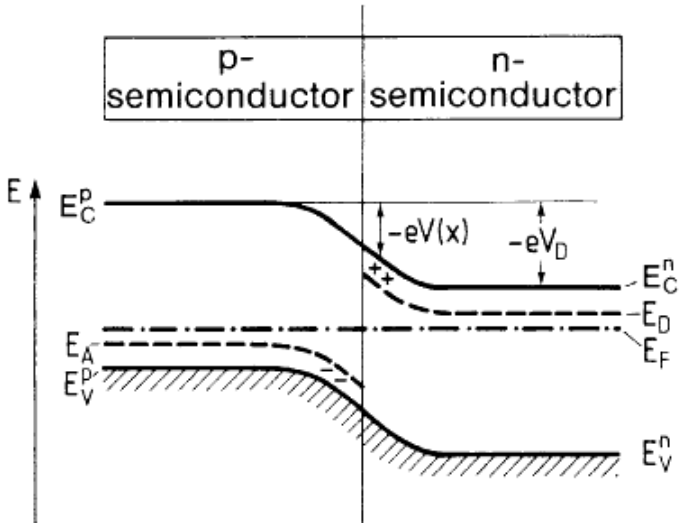

Figure 10: *a representation of p-n junction energy levels.*

In a p-n junction the mobile carriers in each portion of the device (*i.e.* electrons for the n-doped Silicon and holes for the p-doped one) migrate ones towards the others. The recombination of unpaired carriers obviously lowers the system's total free energy. Nonetheless, the progressive disappearance of free carriers (holes and electrons) weakens the shielding effect these carriers provided the fixed charges of Al and P atoms with. An electric field starts building up, up to the point where no free carrier is allowed to

[1] While shallow levels can be considered hydrogen-like systems (whose orbital radius is promptly modified by the medium dielectric constant) mathematical treatment of deep levels is indeed more cumbersome and may require, among other approaches, Green function theory and the sorts.

reach the other side of the field and the recombination of free charges comes to a halt. A depletion zone has been established at the interface between the n-doped and the p-doped portions of the solid.

Energetically speaking, a tweaking of the bands has occurred due to the necessity of the two portions of the solid to have the same Fermi energy. This bending is caused by the electric field between fixed charges of Al^- and P^+.

When the p-n junction is not polarized by an external potential, its total current is null. Whenever a photon is absorbed by the material and its absorption allows excitation of an electron from the VB to CB (*i.e.* its energy is higher than the material optical band gap), an electron-hole couple is formed. This is called a Wannier-Mott exciton[3]. Due to the very high dielectric constant of the solid, this quasi-particle is weakly bound and highly delocalized. Thus, these two charge carriers are quickly separated by the ongoing electrical field across the interface, and a current of free carriers is generated. This photocurrent can be used as any conventional current and is the luck and fortune of the photovoltaic process.

First Photovoltaic Generation

First generation photovoltaic technology is based on single- and polycrystalline silicon wafers. Monocrystalline silicon wafers are usually manufactured by Czochralski[4] method: polycrystalline silicon is placed in a quartz crucible where it is melted using radiofrequency inducers; its crystalline growth is controlled by a crystal seed introduced in the melt and rotated inside the molten silicon, whose temperature is 1687 K, in the opposite direction with respect to the crucible (**Figure 11**). The extraction of the seed allows for the growth of a single-crystal ingot which presents oxygen as the main extrinsic defect[2] and is therefore usable in solar cells. Careful modulation of several critical parameters is paramount to the obtaining of maximum quality monocrystalline silicon.

The very high manufacturing cost of Czochralski silicon has favored the research of viable and more cost-effective alternatives[5]. One of these is polycrystalline silicon. This can be manufactured through either the *chemical route*, a purification and deposition CVD process (which is not, to tell the truth, exactly cheaper) which may be described as

$$Si(s) + HCl(g) \longrightarrow HSiCl_3(g) + H_2(g)$$

$$2HSiCl_3 \longrightarrow Si(s) + SiCl_4(g) + 2HCl(g)$$

where the second step takes place at temperatures above 1400 K, or by the *metallurgic route,* which may either consist of carboreduction of silicon using ultrapure reagents, or by several other techniques, each specific to a single manufacturer, but whose principle is based on controlled fusion, refusion and consecutive crystallization of molten metallurgical-grade silicon. Polycrystalline silicon is somehow less performing than monocrystalline one, mainly due to the presence of extended defects such as grain borders where different crystalline domains of lay one against the other. These defects act as "trap centers" where free charge carriers are trapped and recombined with a hole, decreasing overall efficiency.

[2] Oxygen presence is somehow detrimental to solar cells performance. Modules manufactured using Czochralsky silicon wafers suffer of a loss in performance after the first three hours of light exposure due to the reaction of boron with oxygen.

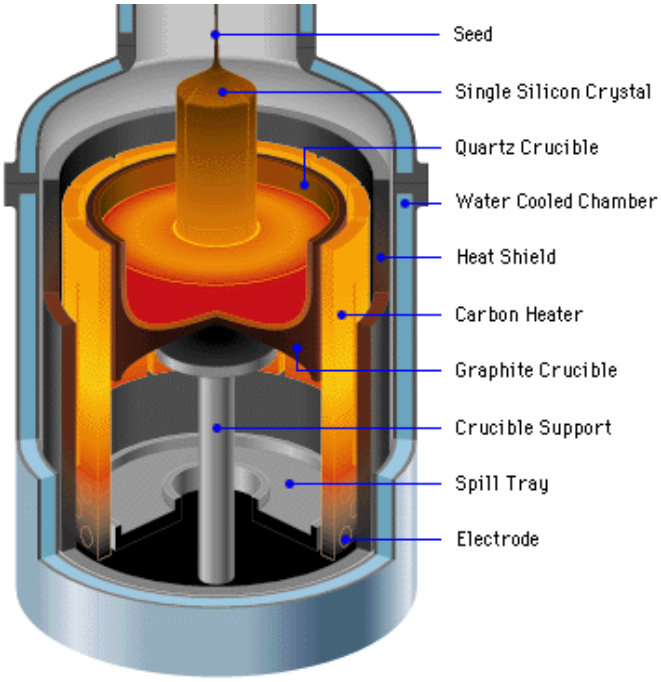

Figure 11: *hardware schematics for crystal pulling following the Czochralski procedure.*

The lowering of performance is somehow balanced by the lower price of manufacturing.

The major limit of bulk solar cells is their absorption edge: silicon energy gap is 1.12 eV, which can be translated in absorbed wavelengths under 1.100 µm. Following the Shockley-Queisser[6] approach, the shape and location of its absorption grant single-junction bulk solar cells a maximum theoretical efficiency of 26% (**Figure 12**), due to their impossibility to gather more than 40% of total solar energy.

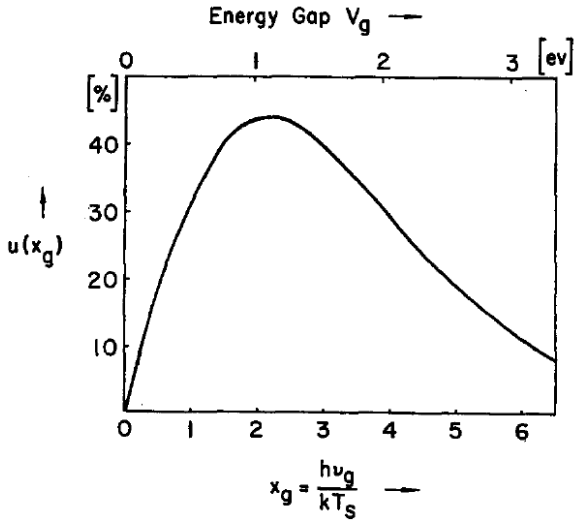

Figure 12: *ultimate efficiency plot against energy gap of a single-junction bulk solar cell as reported by Shockley and Queisser. Maximum theoretical efficiency for silicon (energy gap 1.12 eV) is about 26%.*

Second Photovoltaic Generation

Some years ago, around 2007, the boom in demands for bulk solar cells caused a rapid drop in availability of silicon. This event gave the chance to other kinds of technologies, less dependent on silicon supplies, to carve out their own market share. Additionally, silicon wafers account for more than 50% of the total price of photovoltaic final modules. Substituting them with other less expensive materials or using less silicon for each solar cell could help with the lowering of commercial panel prices. Thin-films solar cells are a perfect example.

The working principles are the same as the wafer solar cells' ones. The main differences lie in the thickness of the semiconducting layer (which ranges from a few nanometers to tens of micrometers) and in the absorbing semiconductor. Various materials are used to achieve performances as high as 11%[7] (**Figure 13**).

Amorphous silicon cells are probably the most common thin-film solar cells. This is both due to the intrinsic environmentally benign nature of silicon and its wide availability. The amorphous silicon is deposited at low temperature in a way that allows about 10% (atomic) hydrogen to be incorporated. The hydrogen greatly improves the quality of the material. A p-i-n junction structure is used with the n- and p-type regions creating a field in the i-layer due to their work-function difference. The very low electrical conductivity of amorphous silicon, though, lowers performances of the final product.

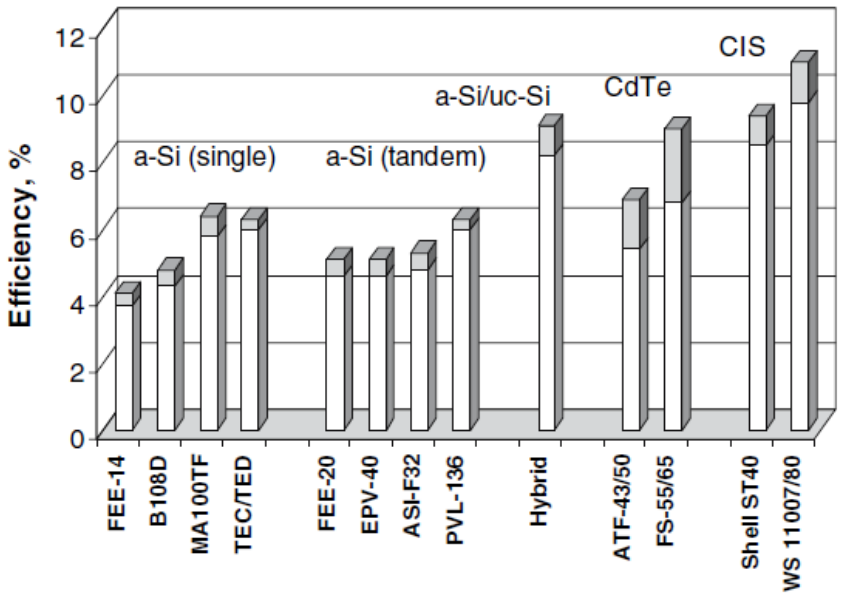

***Figure 13**: some efficiencies as of 2006 of second generation thin film photovoltaic solar cells as reported by Green[10].*

Other materials used for thin film solar cells comprise chalcogenides such as CdTe and CdS (whose components are, though, highly toxic and have thus been disregarded as a long-term viable alternative to silicon), copper indium diselenide or CIS (whose excellent performances, as high as 19.5 are maimed by the scarceness of Indium available in Earth's crust) and copper indium gallium diselenide or CIGS (an alloy of CIS and copper gallium selenide, affording $CuI_xGa_{1-x}S$).

a. b.

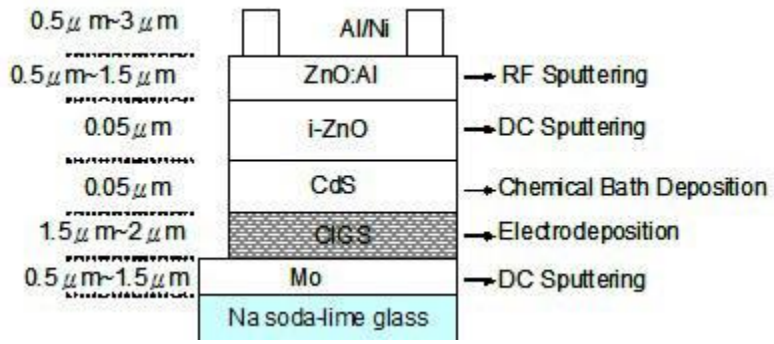

$$\begin{pmatrix} Cu \\ Ag \\ Au \end{pmatrix} \begin{pmatrix} Al \\ Ga \\ In \end{pmatrix} \begin{pmatrix} S \\ Se \\ Te \end{pmatrix}_2$$

Figure 14: *(a) possible components of the CIGS class semiconductive alloys; (b) schematics of a CIGS thin film solar cell. Several alternatives are being considered for the CdS layer .*

Moreover, a-Si modules are easily degraded in the first two months of solar exposure and this brings to unsatisfactory performances (4-6%), which can however be improved by using tandem cells.

In particular this last class of semiconductors (I-III-VI_2) (**Figure 14a**) has been gaining momentum in the scientific community for both its optimal performance (lying just below the 20% threshold) and its very high absorption coefficient in the region of interest (mainly due to its direct band gap semiconductive nature), which significantly lowers total thickness of the cell (**Figure 14b**).

Third Photovoltaic Generation

Third generation of photovoltaic devices is mainly an improvement on second generation thin-films solar cells, featuring (i) different system architectures or (ii) different materials, most notably organic semiconductors.

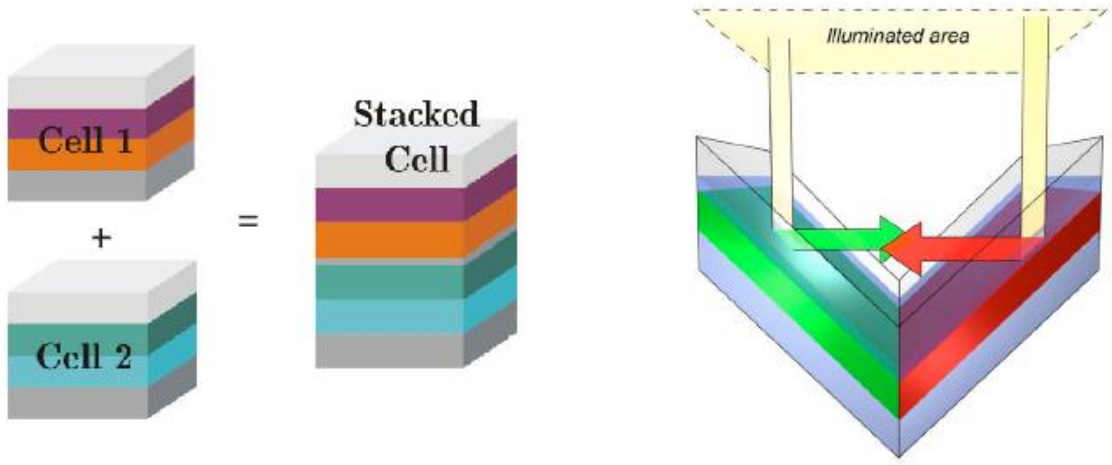

a. b.

Figure 15: *(a) schematics of a stacked tandem solar cell; (b) schematics of a folded light-trapping solar cell.*

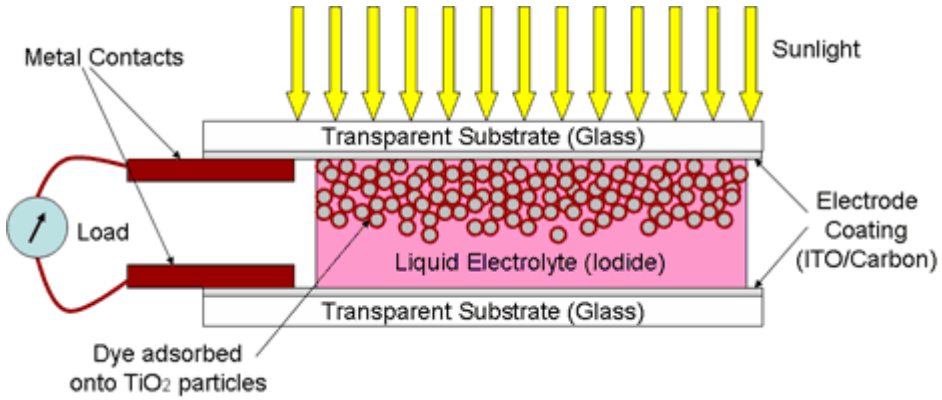

***Figure 16**: schematics of a dye-sensitized solar cell.*

Regarding (i), the tandem approach[8] has attracted serious attention due to its promise to overcome the Shockley-Queisser limit. The core of the concept is granting a single device the maximal absorbing capabilities by combining different cells and extracting the total current generated.

Each cell in the final device has different absorption edges which grant enhanced light-harvesting potentials. Different architectures (e.g. stacked[9] or light-trapping folded[10] solar cells, **Figure 15a** and **b**) are being currently employed in research.

The second major advancement in third-generation photovoltaics concerns materials: both hybrid cells (dye-sensitized solar cells[11], also known as Graetzel cells, and organic-inorganic cells[12,13]) and bulk heterojunctions have shown efficiencies above 7%. Bulk heterojunctions will be object of close examination in following sections.

Dye-sensitized solar cells (DSSC), on the other hand, offer a novel and brisk way of looking at photovoltaics. Their operational principle mimics plants ability to convert solar light in chemical energy by using pigments (chlorophylls and xantophylls). They consist of four critical elements: a dye, a redox couple, a photoanode and a counterelectrode (**Figure 16**). The two phenomena of optical excitation and charge transfer are bound to different components inside the same device. The photoexcitation of the organic dye, absorbed upon titania nanoparticles, allows for an electronic charge-transfer to TiO_2, which, in turn,

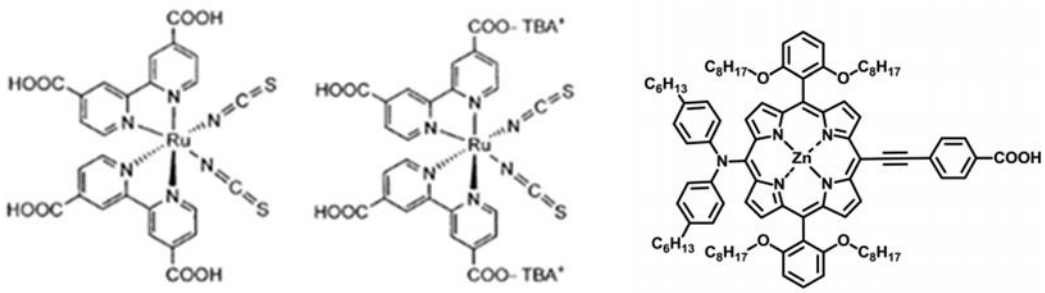

***Figure 17:** state-of-the-art dyes for DSSC. Adapted from references[14,16].*

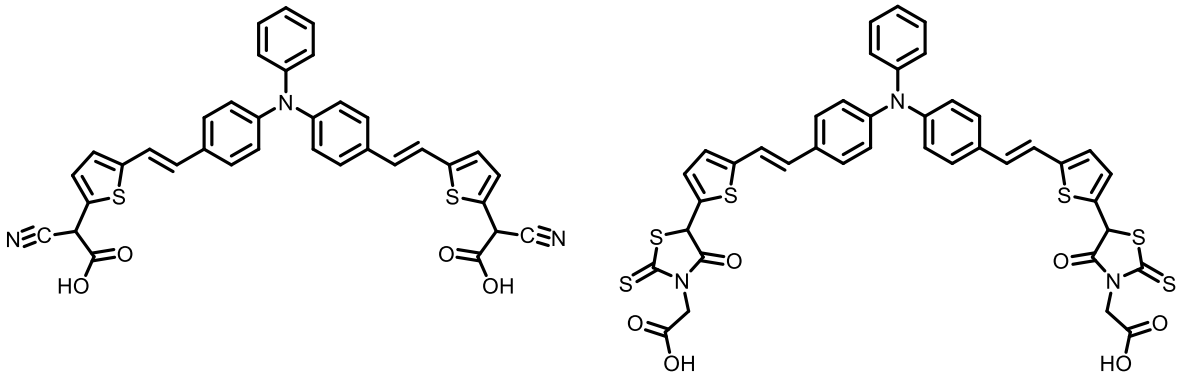

Figure 18: *dibranched D-π-A sensitizers for DSSC.*

transfers electrons to the electrode. The now-oxidized organic dye is reduced to its neutral state by the liquid redox couple (usually a I^{3-} -> $3I^-$ oxidation process), which is then reduced to iodide by the counterelectrode, where electrons from the photoanode end up after their energy is used to power up a load.

Organic sensitizers used for these devices range from organometallic dyes (most notably, bipyridinic ruthenium complexes such as N3 and N719[14], **figure 17**) and push-pull porphyrinic structures to di- and tribranched triphenylamine derivative[15] (**figure 18**) exploiting the D-π-A structure. The excitation and charge transfer mechanisms are different throughout these systems, ranging from being metal-to-ligand charge transfer (MLCT), to canonical π->π* HOMO-LUMO transition. Anchoring of these substrates to the titania nanoparticles is achieved through the carboxylic moieties capping the dyes. These systems have shown efficiencies as high as 12.3%[16]. The main problem with this approach to photovoltaic, though, is the liquid electrolyte, which stiffens the system because a rigid encapsulation of the device has to occur in order to maintain operability of the cell. This issue has been addressed with research of solid redox couples to achieve the same goals as iodine, but the low mobility of solid matrices prevented these systems to achieve the same results as their liquid counterpart[17].

More recently a new class of materials for the employment in DSSC-like device architectures rose to the attention of the community[18]. They are called perovskites, and follow the general structure ABX_3, where A and B are positive cations with very different sizes and X is an anion, typically a halogen. The A cation, the one with the biggest atomic radius, has 12-fold cuboctahedral coordination, while B has a 6-fold octahedral motif (**Figure 19**). The electronic properties of these materials can be vastly tailored to the

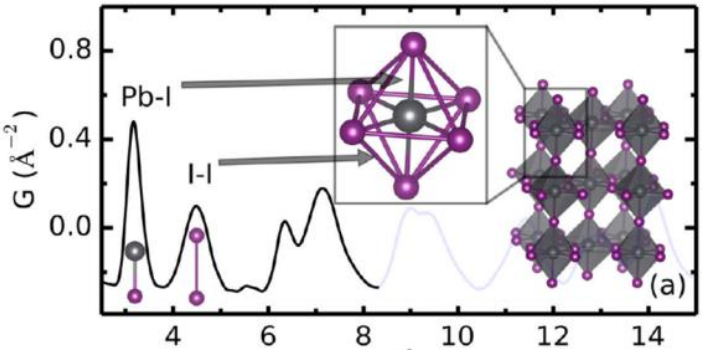

Figure 19: *atomic pair distribution function of bulk $CH_3NH_3PbI_3$ perovskite. The first peak corresponds to the nearest neighbor distance (Pb–I), the second peak to the shortest I–I distance, and so on. Adapted from reference*[59].

required applications, are inherently microcrystalline and their electronic behavior can be easily characterized[19].

In particular the material which set the performance benchmark is a mixed organic/inorganic lead perovskite by the formula of $CH_3NH_4PbI_3$, which is routinely obtained by dissolving Lead(II) Iodide and methylamine in DMF, spincasting the solution and thermally treat it. These materials have shown impressive efficiencies, in the order of 15% and upwards[20], but are plagued by some problems. These issues are now being addressed by the community to understand and improve the highly water-sensitive materials[21], the hysteresis of JV curves[22], the scarcely reproducible results[23] and the effective toxicity of the compounds involved[24].

Bulk Heterojunctions

One particular class of organic photovoltaic devices (from now on, OPVs) promises cost-effective mass production and flexibility. They are called bulk heterojunctions (BHJ) and are an evolution of bilayer heterojunctions first devised by Tang in 1986[25]. Their photoactive layer consists of a blend of an electron-rich, hole-conducting organic substrate (the "donor" D) and of an electron-conducting substrate ("acceptor" A).

Figure 20: *schematics of a bulk-heterojunction solar cell.*

The promise these system convey is one of low-cost processing (roll-to-roll mass production, solution-casting, doctor blading) at room temperature on flexible substrates such as cloth or plastic. The operational principle is similar to what has been exposed in Section 1.3.4, except for a most notable difference: dielectric constants in organic molecular or polymeric solids (ε in the range of 3-4) is not as high as in inorganic insulators or semiconductors (ε about 12). This implies that excitonic states will be far more localized and bound than in Wannier-Mott excitons. These strongly bound electron-hole interactions are called Frenkel excitons[26] and their binding energy can be as high as 1.5 eV. They can be perceived as neutral quasi-particles that can move around in the solid as a free carrier would. Their diffusion length λ_D typically ranges from 5 to 70 nm in organic conjugated materials[27–29].

Whenever a Frenkel exciton diffuses to a donor-acceptor interface, the frontier orbital level offset between the donor and the acceptor induces electron transfer across the interface. If the exciton is localized on the donor, the electron jumps from LUMO (Lowest Unoccupied Molecular Orbital) D to LUMO A; if the exciton is instead on the acceptor side, the hole transfers from HOMO (Highest Occupied Molecular Orbital) A to HOMO D. The exciton is now split and two distinct free carriers have been generated. Since excitonic splitting happens only at the interface, this should underline the importance of bulk morphology in BHJ OPV.

The total cell efficiency rests upon several different processes: (i) absorption of incident photon and formation of a Frenkel exciton; (ii) exciton diffusion; (iii) free carriers generation; (iv) carriers diffusion to the electrodes; (v) carriers collection at the electrodes.

Process (i) is mainly dependent from the energy gap of the absorbing materials and is the main parameter on which a Shockley-Queisser analysis is based[30]. Obviously, the lower the band gap, the higher the percentage of total solar radiation is absorbed. Thus, as previously noted, Silicon (Eg=1.12 eV) has an ultimate efficiency of about 27%, while a 1.4 eV energy gap polymer has a maximum ultimate efficiency below 20%[26].

Also, thickness of the photoactive layer is non-trivial in determination of total absorption because too thin a layer may not harvest all of the solar radiation, while too thick a layer could lead to detrimental unnecessary series resistance and to lower percentage of excitons able to diffuse to the D-A interface.

Diffusion, in fact [process (ii)] may proceed in two distinct physical ways: Foerster (long range, 3-10 nm) and Dexter (short range, 0.3-2 nm). While the former is based upon electrostatic interaction due to insurgence of dipoles in the excited molecule, the latter rests on overlapping electron clouds between adjacent molecules[31]. Diffusion efficiency η_{DIFF} is always <1 due to the presence of trap centers and to radiative or non radiative recombination. Furthermore, the presence of aggregates hampers (J-aggregates) or improves (H-aggregates) the diffusion of excitons between dimeric molecular units. All considered, an acceptable percentage of diffused excitons to the interface is obtained when total thickness of the sample is shorter than the diffusion length λ_D. The BHJ principles lie exactly on these assumptions: their efficiency lies in the fact that enhanced interpenetration allows for major excitonic separation.

Process (iii) usually has unitary yield: in fact as long as ionization potential of D + electronic affinity of A is smaller than Frenkel exciton energy, the process is largely favored.

Process (iv) is usually one of the critical values which mainly affects BHJ OPV final performances. In fact morphological disorder (a common but not mandatory feature for bulk-heterojunctions) hinders conductivity of carriers to the electrodes. Crystalline phases would create electronic “bands” as in inorganic semiconductors. This would make transportation of free carriers very efficient. Unluckily this is not the case with solution-processed organic materials (apart from some peculiar architectures which heavily rely on the system anisotropy and showed outstanding efficiencies[32] for small molecule bulk-heterojunctions, SMBHJ). Insofar, charge carriers transport has been mainly inferred to tunneling and hopping mechanics, inherently less effective.

Process (v) usually also yields unit efficiency as long as the anode Fermi level is lower than acceptor LUMO and as long as cathode Fermi level is higher than donor HOMO.

The benchmark for BHJ performances is now represented by a Poly({4,8-bis[(2-ethylhexyl)oxy]benzo[1,2-b:4,5-b’]dithiophene-2,6-diyl}{3-fluoro-2-[(2-ethylhexyl)carbonyl]thieno[3,4-b]thiophenediyl}) : [6,6]-phenyl-C_{71}-butyric acid methyl ester (**PTB7:PC$_{71}$BM**) blend[33]. The record efficiency in inverted architecture is 9.2%, as of now[34]. The first BHJ approach to photovoltaics was made using poly(phenylen-vynilene) derivatives in combination with fullerene C_{60}[35]. Due to inherent PPV-type low mobility and large optical gap, their efficiencies were modest (in the 3% range). The passage to P3HT favored rising of maximal currents. A refinement of post-deposition treatments (e.g. annealing) improved overall cell performances.

These, in fact, are obviously correlated to the formation of a bicontinuous interpenetrating interfaced network between A and D, which is paramount for the exciton splitting.

Additives have been previously used in literature to enhance morphological order inside the photoactive blend. Alkylthiols[36] or α,ω-dihalo alkanes[37] of different lengths allowed the formation of enlarged crystalline domains, thus improving both carriers' mobilities and lifetimes. A balance has to be struck in this kind of tweaks, though: excessive presence of plasticizers can create domains whose mean dimension is larger than λ_D, hindering dissociation and favoring recombination, which was detected as photoluminescence[38]. The amount of diiodooctane, for instance, is usually limited between 0.1 and 3%.

Solvent used for deposition deeply influences roughness of the interface: while toluene yields a coarser phase separation (200-250 nm), chlorobenzene allows grains to be about 50 nm wide; needless to say that the augmented surface/volume ratio improves carriers separation.

Another approach to the same problem is SMBHJ. While, in general, low weight small molecules perform sensibly worse than polymer-based BHJ, it's important to remember that PCBM in fact IS a single low-molecular weight molecule, and its performances are unsurpassed even by polymeric materials. Direction of research should then try to focus on positive aspects of SMBHJ:

- ✓ A perfectly defined chemical structure erases the problems posed by the structural variability of polymers, namely, the control of the regioregularity, molecular weight, and polydispersity;
- ✓ Purification of a single molecule is in general easier than that of a polymer;
- ✓ Materials derived from molecular elemental units show in general higher charge-carrier mobilities than polymers;
- ✓ Ordered films of molecules with higher carriers mobilities can be obtained through sublimation techniques;
- ✓ The analysis of the relationships between chemical structure, electronic properties, and device performances is more straightforward than that for polymers for which structural modifications can indirectly affect the electronic properties through changes in molecular weight, polydispersity, and effective conjugation length;
- ✓ The high molecular extinction coefficients of many molecular dyes permits limiting the thickness of the active layer, thus minimizing problems associated with charge transport and series resistance;
- ✓ Many small dye molecular structures can be viewed as quasi-spherical particles, which can be more appropriate to isotropic optical and transport properties than linear systems.

Different classes of compounds have been reported during the years: dendrimeric star-shaped oligothiophenes, soluble acenes, push-pull chromophores, diketopyrrolopyrrole and squaraines, just to name a few. As of now, the record efficiency for organic-based photovoltaic has been reported by Heliatek, a German company using with evaporated bilayers.

Recently the community has provided interesting solutions to eschew PCBM from the mixtures due to its excessive cost (especially $PC_{71}BM$). Polyera Inc, an Illinois-based company specialized in formulations for

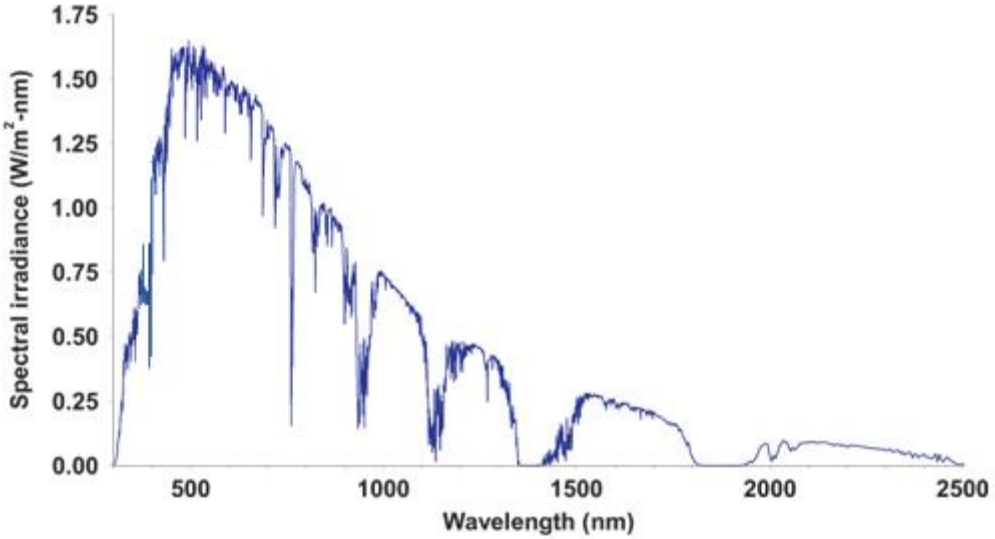

Figure 21: *AM1.5G solar irradiance spectrum used for characterization of photovoltaic devices[1].*

high-performance organic electronics, has recently reported an all-polymer, solution processable BHJ with a 6.4% (once again, no reported structures).

In the field of SMBHJ several classes of materials are rising as interesting alernatives to PCBM, perylen bisimides[39] and boron-complexed subphthalocyanine or naphthalocyanine multistacks[40] being the most relevant.

Main cell parameters

Scientific community's need of comprehension of the several mechanisms hidden behind the apparently ease of use of a photovoltaic device brought to the definition of numerous parameters to evaluate an OPV performance. This description will be tailored to explain the meaning of these factors for BHJ and SMBHJ. The general relevance and the similarities of the phenomena involved make the generalization of such concepts a trivial issue.

First of all, given the flickering nature of Sun's radiance upon earth surface, some standards have been instituted. Any response of OPVs is thus taken under the ASTM Standard G159, which has been named Air Mass 1.5 (AM1.5, **Figure 21**). The so-called AM1.5G, the overall reference for solar cell characterization, cumulates an integrated power density of 1000 $W.m^{-2}$ and an integrated photon flux of 4.31 x $10^{21}.s^{-1}.m^{-2}$, distributed over a large range of wavelengths (280-4000 nm). This system simulates the solar radiation and the absorptions due to Earth's atmosphere hitting the surface with an angle θ=48.19° between perpendicular and direction of incidence.

Under these normalized irradiation conditions it is now important to define meaningful key parameters for evaluation of OPV under an AM1.5G standard light.

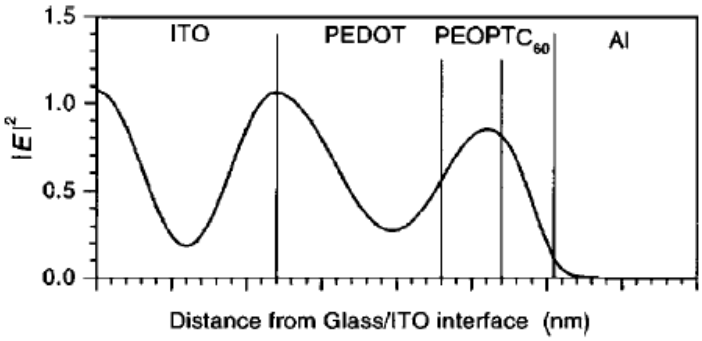

Figure 22: *electromagnetic optical field distribution inside the photoactive layer of the BHJ. The thickness of the layers has been optimized as to maximize $|E^2|$ at the D-A interface*[60]*.*

I. Short circuit current J_{SC}

When potential is null (short circuit conditions) two currents occur at the D-A interface. One is the **drift** current which is induced by the internal electric field produced by the potential slope following from Fermi level alignment. The other one is associated with the diffusion of dissociated carriers at the interface.

They have the same direction and are thus summed one with the other. Through the use of transfer-matrix formalism it is possible to calculate the electromagnetic field distribution inside the photoactive layer and the total number of photons thus absorbed (which is roughly proportional to the short-circuit current). If the different layers the cells comprise are stacked in such a way as to place the D-A interface exactly where the electromagnetic optical field is maximum, the short circuit current is enhanced (**Figure 22**). Common routes to improve J_{SC} are decreasing the optical band gap and improving the mobility of charge carriers in the photoactive layer.

II. Open circuit voltage V_{OC}

Under open circuit conditions, the resulting current density must become zero, so that drift and diffusion currents compensate each other. Recent insights in the issue at hand have demonstrated proportionality between the energy difference $|HOMO_D\text{-}LUMO_A|$ and the final measured V_{OC}. This is because whenever in the device a non-ohmic contact is used (e.g. Calcium) the pinning of the electrodes' Fermi levels to corresponding HOMO and LUMO levels (namely, cathode Fermi energy pinned to acceptor LUMO and anode Fermi energy pinned to donor HOMO) causes the V_{OC} to be directly proportional to their difference.

So, lowering of the HOMO can and has improved performances in BHJ OPV, as reported by Konarka (even if the structure of the modified lower-HOMO polymer remains undisclosed).

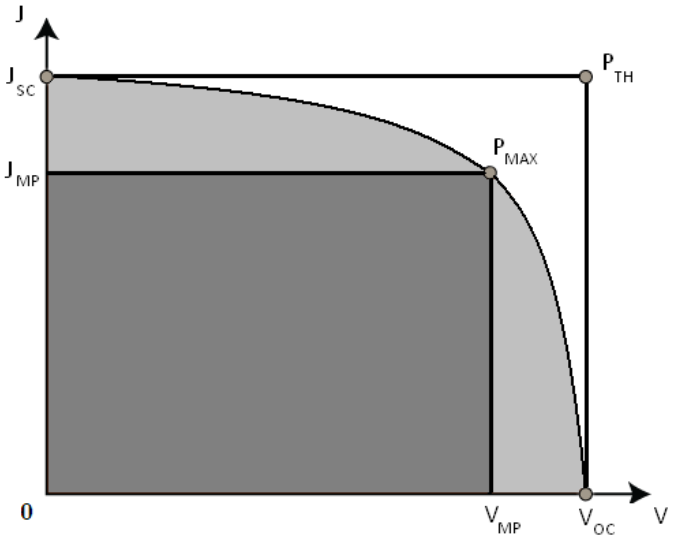

Figure 23: *typical I-V curve. Main photovoltaic parameters are reported on the sketch.*

Recent endeavors for new acceptor materials have also increased the open circuit voltage by employing bis-PCBM instead of normal PCBM. Infact under same solution-processing conditions, multiadducts PCBM featured a 120 mV higher V_{OC}[41] with respect to PCBM (**Figure 24**).

	Fullerene type	V_{oc} (V)	J_{sc} (A m^{-2})	Fill factor (%)	Efficiency (%)
A	PCBM	0.61	89.4	60	2.4
B	Bis[60]PCBM	0.73	73.0	63	2.4
C	Bis[70]PCBM	0.75	70.3	62	2.3

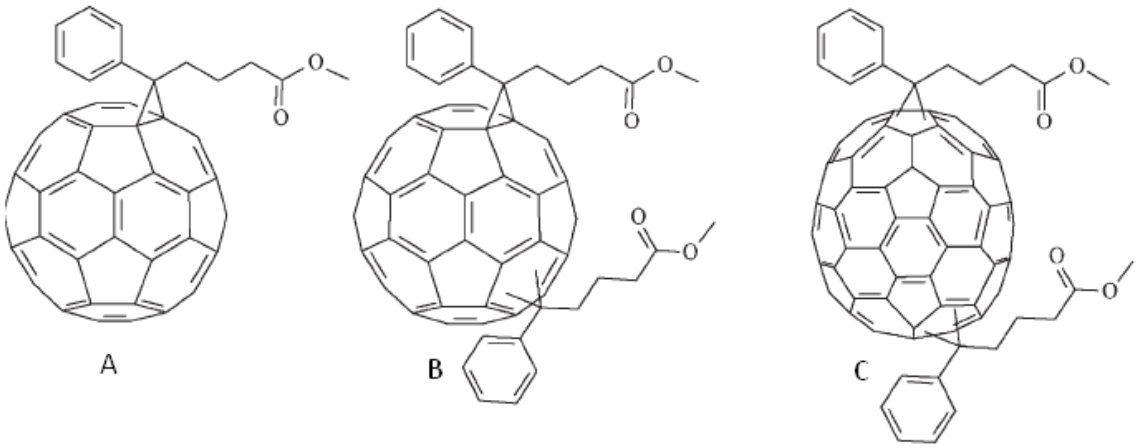

Figure 24: *key parameters for P3HT:fullerene BHJ OPV. Adapted from reference*[41].

III. Fill factor FF

This parameter describes the ratio between the maximum theoretical power the device can dispense (J_{SC} x V_{OC}) and the maximum power rectangle which one can inscribe under the I-V curve, whose vertices are J_{MP} and V_{MP}: FF = (J_{MP} x V_{MP}) / (J_{SC} x V_{OC}). Recently efforts by Guo et al. have afforded FF as high as 80%[42]. This parameter is strictly correlated to the shape of the curve, analysis of which can provide insights in the resistive behavior of the heterojunction[43], which can be caused by a strongly asymmetric mobility of electrons vs holes or by a very high contact resistance, either due to delamination of the material from the electrode or to a lack of energetic alignment.

IV. Internal quantum efficiency (IQE) and external quantum efficiency (EQE)

These two parameters show how high is the percentage of electrons following their theoretical behavior and are a measure of system's efficiency. IQE is defined as η_{DIFF} x η_{CT} x η_{TR} x η_{CC}, where, in order, the η denote the efficiency for diffusion, charge transfer, transport to the electrodes and carrier collection at the electrodes. EQE is IQE x η_{ABS}, which denotes absorption efficiency. The EQE curve versus irradiation wavelength usually has the same profile of the dye absorption. EQE (λ) may also be written as 1.24 x J_{SC}/(λ x E_e), where E_e denotes the illumination (photonic flux ϕ_e on surface, in W.cm^{-2}) on the device.

V. Efficiency η

This parameter summarizes all of the above definitions and musters the OPV energy conversion capabilities. It is defined as P_{MAX} /ϕ_e = (FF x J_{SC} x V_{OC})/ϕ_e. Theoretical insights have shown how whenever thermalization of excitons is minimized by lowering the energy difference between $LUMO_D$ and $LUMO_A$ energy levels efficiency consequently rises (**Figure 25**).

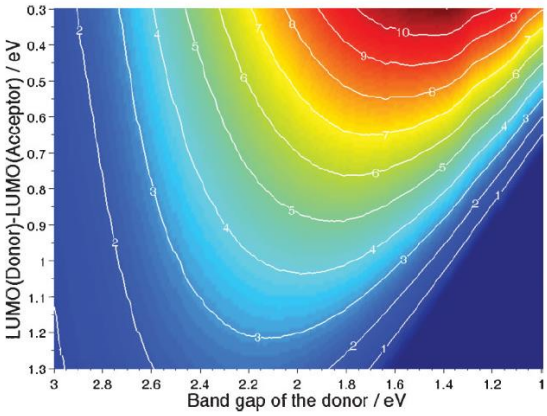

Figure 25: *theoretical calculations suggest that upon bandgap shrinking (Shockley-Queisser ultimate efficiency) and $LUMO_D$-$LUMO_A$ energy levels minimization, efficiency could be raised as high as 10% in BHJ-OPV.*

RESULTS AND DISCUSSION

Most of the impressive results obtained thus far in the field of organic photovoltaic suffer from the important flaw of being device area and/or deposition technique dependent. Part of this thesis was dedicated to the proof of principle demonstration of the applicability of photoresists chemistry to the production of working OPV devices. As the process is carried out after deposition and solvent evaporation, (i.e. simultaneously on the whole active area) this strategy is more easily up-scalable in high throughput deposition techniques and plant processing.

Photoresists are a very large class of both polymeric and molecular derivatives possessing photosensitive functionalities which upon exposition to radiation of the appropriate wavelength causes a solubility increase (positive photoresists) or decrease (negative photoresists) of the host matrix in a given solvent. Standard photoresists find application in lithographic processes, and as such they are insulating (i.e. weakly conjugated) and colorless. We have hereby included both cinnamic ester and acrylic (and meth-acrylic) moieties in squaraines as building blocks for functional negative photoresists.

We aim at materials which would be able to retain photovoltaic performances after UV-induced photocrosslinking. Whilst completely original in the context of OPV devices, a similar approach was proven successful and resourceful by the groups of McCulloch[44,45] and Reynolds[46] in the context of organic field effect transistors and electrochromic devices, respectively. We show that we can perform the photopolymerization process on both pristine films of the squaraine compounds as well as blends with the commonly employed acceptor PCBM. The resulting crosslinked films become insoluble in common organic solvents, while still retaining sizeable photovoltaic performances.

One of the areas of expertise of the Beverina group at Milano-Bicocca is the chemistry and photophysics of squaraines, the products of 1,3-dicondensation of squaric acid with two equivalents of an activated arene or anhydrobase. Their high extinction molar coefficients ε (10^5-10^6 $L.mol^{-1}.cm^{-1}$), granted by the cyanine-like electronic structure characterizing squaraines, allow very efficient uptakes of the solar radiation. This makes reducing the thickness of the organic photoactive layer possible, with all the advantages described thus far. Squaraines absorption spectra in solution are sharp and intense. In the solid state, though, their absorption spectra sensibly widens due to aggregation (which in the right conditions could enhance free carriers transport to the electrodes, *vide supra*).

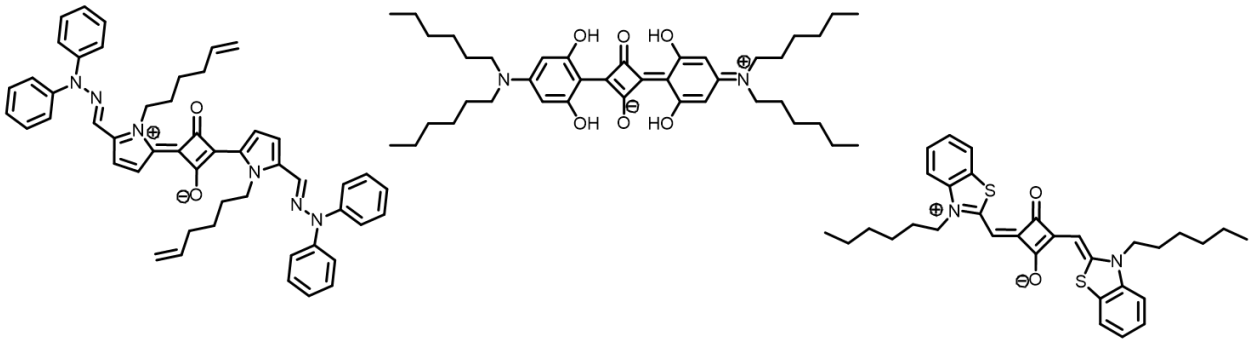

***Figure 26**: three archetypal structures of squaraine dyes; (left) hydrazonic squaraines[61]; (center) aminoresorcinol squaraines[62]; (right) methinic bridge squaraines[63].*

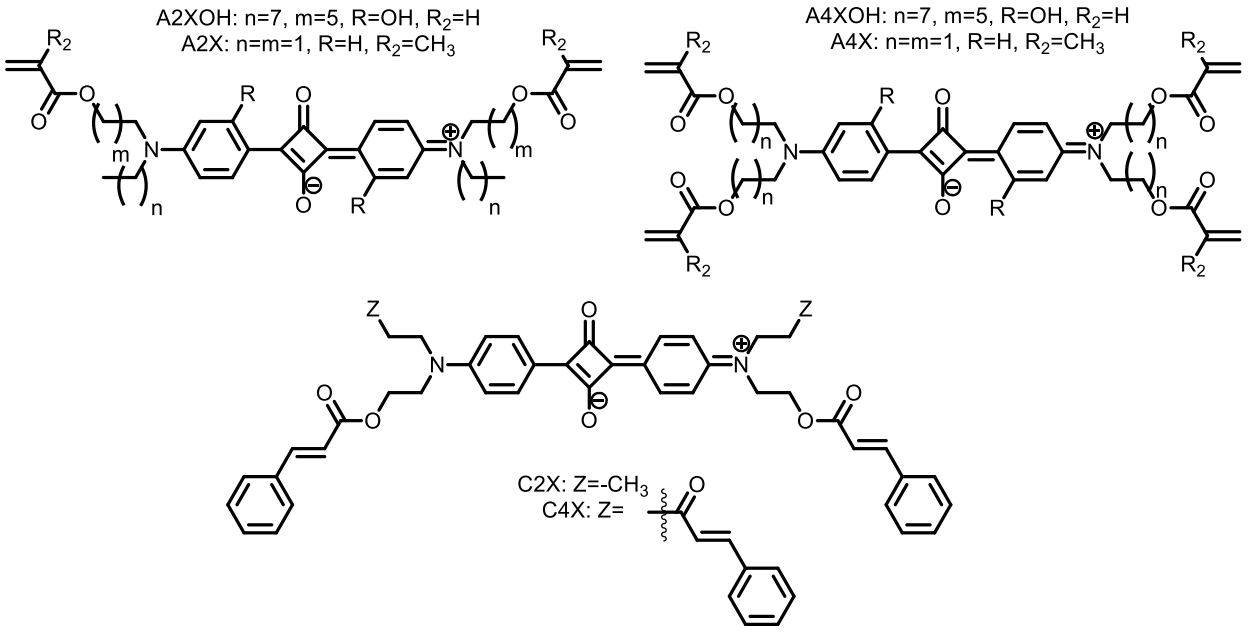

***Figure 27**: structure of the selected squaraines*

Synthesis

A very important endowment of squaraine dyes is the extreme flexibility of the attainable structures. Several electron-rich arene and anhydrobase derivatives, in fact, react with squaric acid to yield both symmetrical and nonsymmetric squaraines. Their application in BHJ[47,48] (as polysquaraines), SMBHJ[49–51] and DSC[52–54] and their good results in these areas account for their strong and expanding niche in the vivid landscape of photoactive materials. We thus considered one of the simplest squaraine general structure, the anilino-squaraine (**Figure 27**), targeting the proof of concept demonstration of a method rather than at the achievement of particularly high conversion efficiencies.

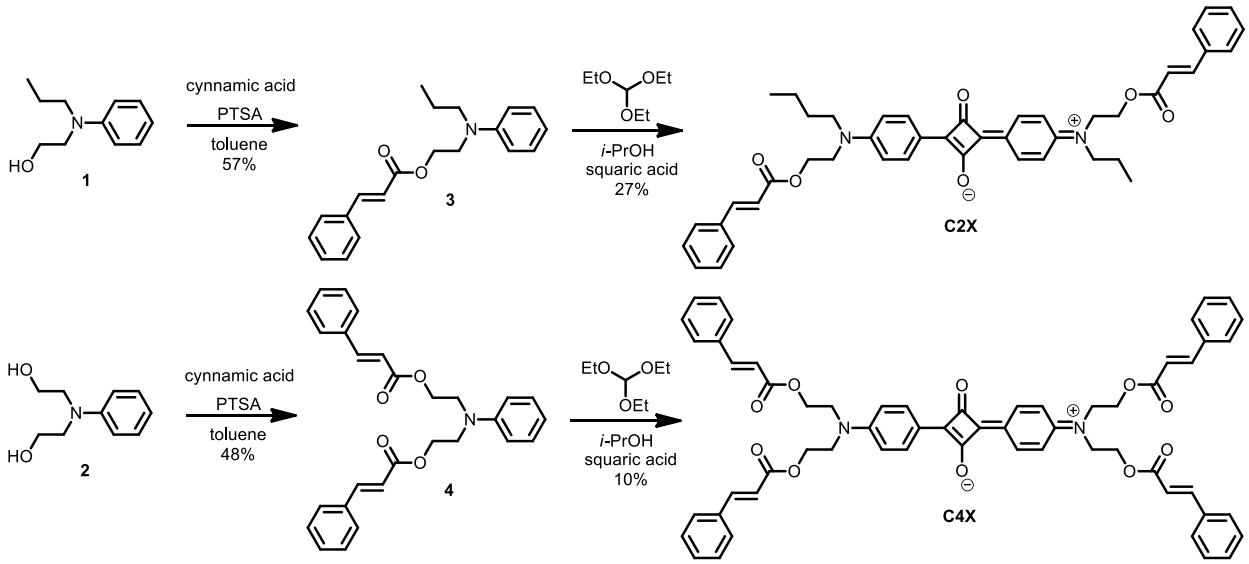

***Scheme 1:** synthesis of C2X and C4X.*

Therefore, as in principle both acrylic and cinnamic derivatives could be successfully employed for photocrosslinking experiments, we synthetized derivatives **A2X** and **A4X** bearing two and four acrylic functionalities, respectively, as well as derivatives **C2X** and **C4X** bearing the same number of cinnamic residues (**Figure 27**). The synthetic access is the same for all derivatives.

Scheme 1 reports the synthesis of **C2X** and **C4X**. In this pathway the alcohol-functionalized anilines **1** and **2** were condensed with cinnamic acid through a Fisher paratoluensulfonic acid-catalyzed esterification in toluene to give anilines **3** and **4**, respectively. The latter were subsequently condensed with squaric acid in isopropanol and in the presence of an excess of ethylorthoformate to give squaraines **C2X** and **C4X** in 27 and 10 % yield respectively as blue powders.

The choice of the solvent is of extreme importance in the formation of squaraines. In fact previous studies in Beverina's group have shown that the squaric acid undergoes esterification with the alcohol before it reacts with the electronrich arene. Triethylorthoformate, on the other hand, acts as a dehydrating agent due to its nature of masked aldehyde, which can react with water to drive the equilibrium towards the products. In any case, it is important to eliminate water as it forms, either via chemical methods (i.e. reactions) or via physical techniques (e.g. molecular sieves, distillation, Dean-Stark apparatus).

According to a similar scheme, **1** and **2** were condensed with methaacriloyl chloride in the presence of triethylamine to give functionalized derivatives **5** and **6**, eventually condensed with squaric acid in isopropanol/triethylorthoformate to give **A2X** and **A4X** in 17 and 27 % respectively. The synthesis of the latter methacrylic squaraines is complicated by the instability of **5** and **6**. Both derivatives in fact cannot be isolated and purified due to their extremely efficient spontaneous self-polymerization. We have hypothesized that the extremely rich electron pair of the nitrogen acts as a polymerization starter, since

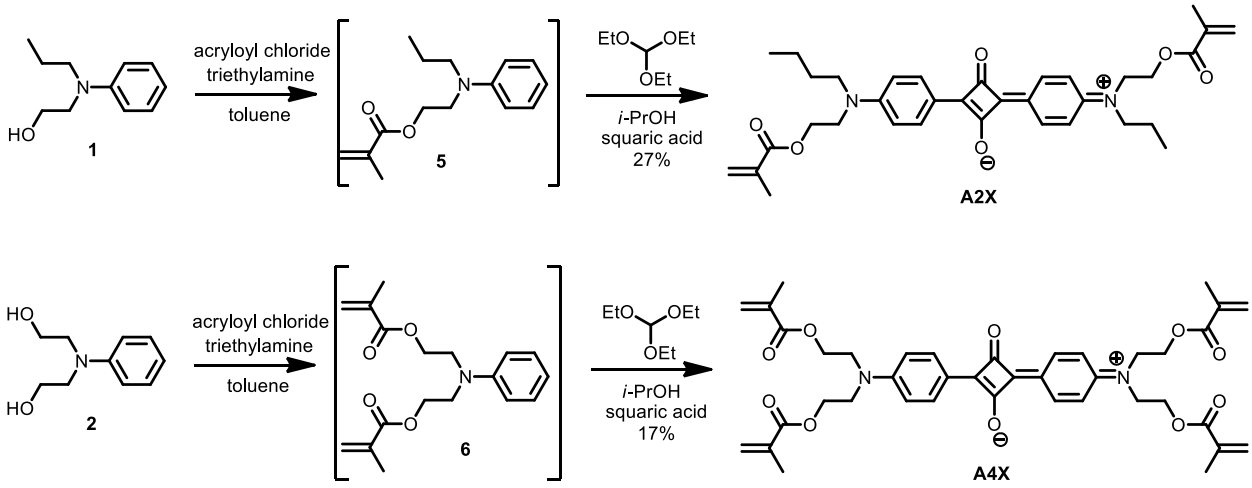

***Scheme 2**: synthesis of A2X and A4X.*

we have observed these viscous oils turn into gels upon standing, even at reduced temperatures and in the dark. As such, we employed a one-pot process starting directly from **1** and **2**, removing the solvent used for the esterification and proceeding to the condensation with squaric acid. This procedure afforded two solid powders as final products. Our attempts to synthesize **A2X** by functionalizing an already preformed squaraine skeleton met with little success (Scheme 3, **A2X** was recovered only in small traces), probably because of the reported interaction of squaraine cores with thermally generated radicals[55].

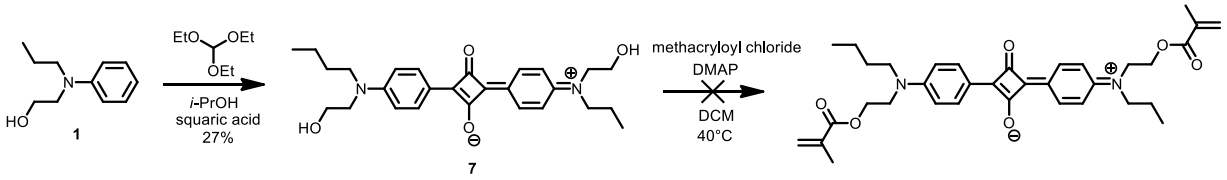

Scheme 3

Knowing that planarity is, as a rule of thumb, extremely important towards conduction mechanisms in the bulk (see Chapter II), we also prepared the hydroxyl functionalized derivatives **A2XOH** and **A4XOH**. In fact the presence of a hydroxyl group adjacent to the squarylium core is known to enforce planarity and thus possibly bolster the efficiency of the target application.

Derivatives **A2XOH** and **A4XOH** were prepared (Scheme 4) starting from 3-aminophenol **8**. The latter was alkylated first with bromooctane, to give N-octyl-3-aminophenol **10**, and then with 6-bromohexyl acrylate to give derivative **11**, eventually converted into squaraine **A2XOH** by reaction with squaric acid in the usual iPrOH/(EtO)3CH mixture. Direct double alkylation of **7** with excess of **9** yielded the diacrylated aniline **9**, directly converted in squaraine **A4XOH** following the usual procedure. It is worth mentioning that compounds **9**, **10** and **11** showed only traces of a *O*-alkylation with respect to the *N*-alkylation, the main impurities being unreacted reagents, bis-alkylated compounds (as for **10**) or ammonium salts (for compounds **9** and **11**).

The extension to tetrahydroxy functionalized derivatives, the most efficient squaraine compounds reported to date, proved to be unfeasible from the synthetic point of view. This is probably most likely due to the extreme electronrichness of a bis-alkilated aminoresorcinol, which causes *O*-alkylation or direct reaction with acrylic moieties.

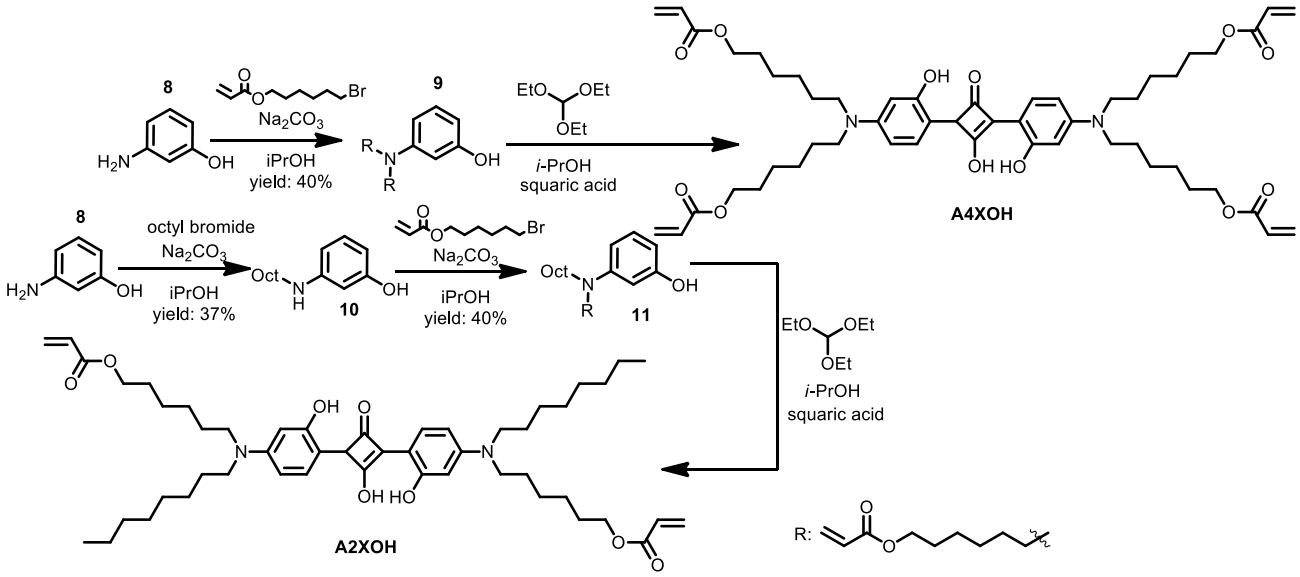

Scheme 4: *synthetic pathways to squaraines A2XOH and A4XOH.*

Characterization of the molecules

Derivatives **C4X** and **A4X** were characterized by coupled DSC/TGA analyses (**Figure 28**). We found no evidence of thermally-induced crosslinking (featureless DSC plot) or major decomposition (TGA trace) for both of the products, showing no sign of spontaneous thermally-induced crosslinking. All of the reported final products can be stored (in the dark) at room temperature for an indefinite time.

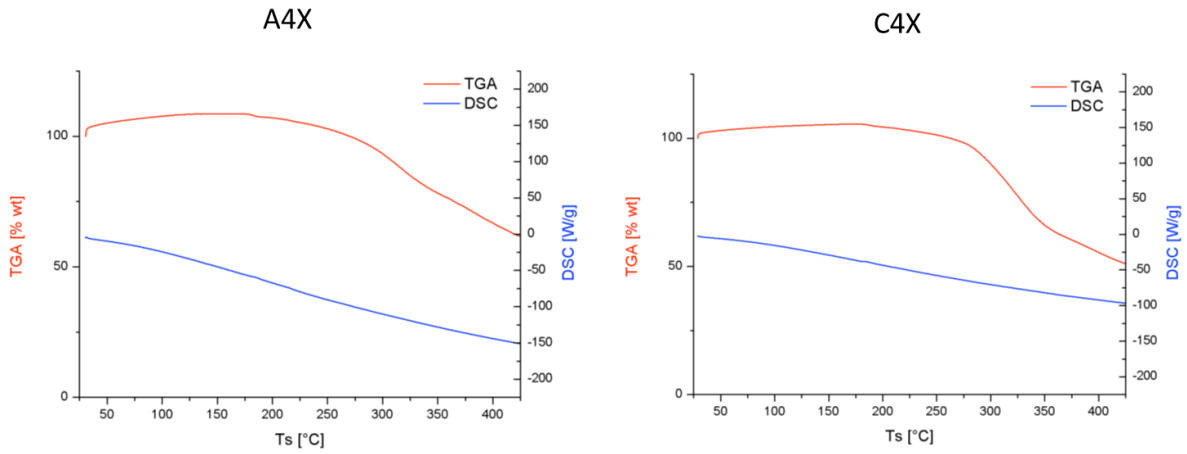

Figure 28: *DSC traces (blue) and TGA plots (red) for (left)* ***A4X*** *and (right)* ***C4X****.*

We report only the UV-Vis characterization of **A4XOH** as a benchmark for all other compounds. The absorption features the typically sharp and intense peak of squaraines, with a shoulder at higher energies, commonly attributed to the first vibronic transition. A thin film of the same compound shows a sizeable broadening of the absorption due to solid-state aggregation. Once the film is crosslinked there is an

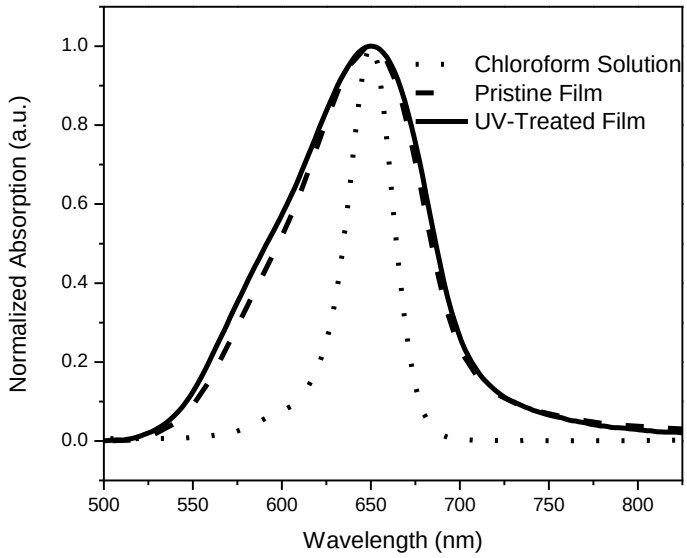

Figure 29: *UV-Vis normalized absorptions of A4XOH / 5% w/w IRGACURE 651. Dotted line: chloroform solution; Dashed line: pristine film on ITO/PEDOT:PSS; Solid line: same film after UV-treatment in Nitrogen atmosphere.*

additional broadening at lower enegies, likely due to a perturbation in the aggregation behavior due to the different solid-state crosslinking of the chains. The optical gap of the hydroxyl functionalized derivative **A2XOH** is smaller than that of **A2X** due to hydrogen bond-enforced planarization of the former conjugated core.

	λ_{MAX} (nm)	ε (L mol^{-1} cm^{-1})
C2X	625	~220.000
C4X	625	~220.000
A2X	629	~240.000
A4X	639	~250.000
A2XOH	638	~240.000
A4XOH	649	~230.000

UV-Catalyzed Photocrosslinking

Turning to photocrosslinking behavior, we characterized the cinnamic derivatives first as this particular cross-linking scheme can be performed without the help of a photoinitiator, which would be beneficial for the target application, due to the weakly conjugated nature of the photoiniziators and their resulting low conductivity.

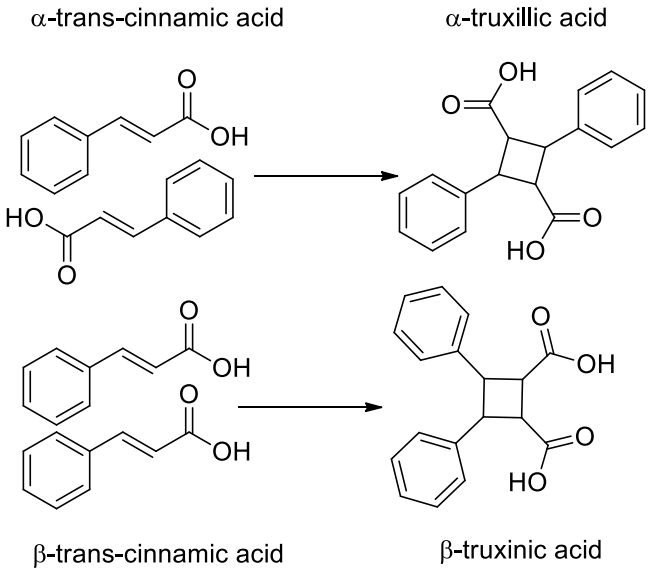

Figure 30: *different possibilities for the dimerization of trans-cinnamic acid. (Above) favourable α head-to-tail form; (below) favourable β head-to-head form. Adapted from reference*[58]*.*

The cinnamic dimerization is a classical photocatalyzed [2+2] cyclization[56]. It is strictly topochemical, meaning that the solid state structure of the molecules is paramount to the efficiency of the photodimerization, and it is catalyzed by UV light (the dimerization quantum efficiency is 0.7 @ 302 nm[57]). When brought out on *trans*-cinnamic acid, the resulting products can be either the α-truxillic acid or the β-truxinic acid, as reported in **Figure 30**. These two isomers stem from the crystalline habit of the monomer, and only when the two double bonds are less than 4.2 Å away one from the other the

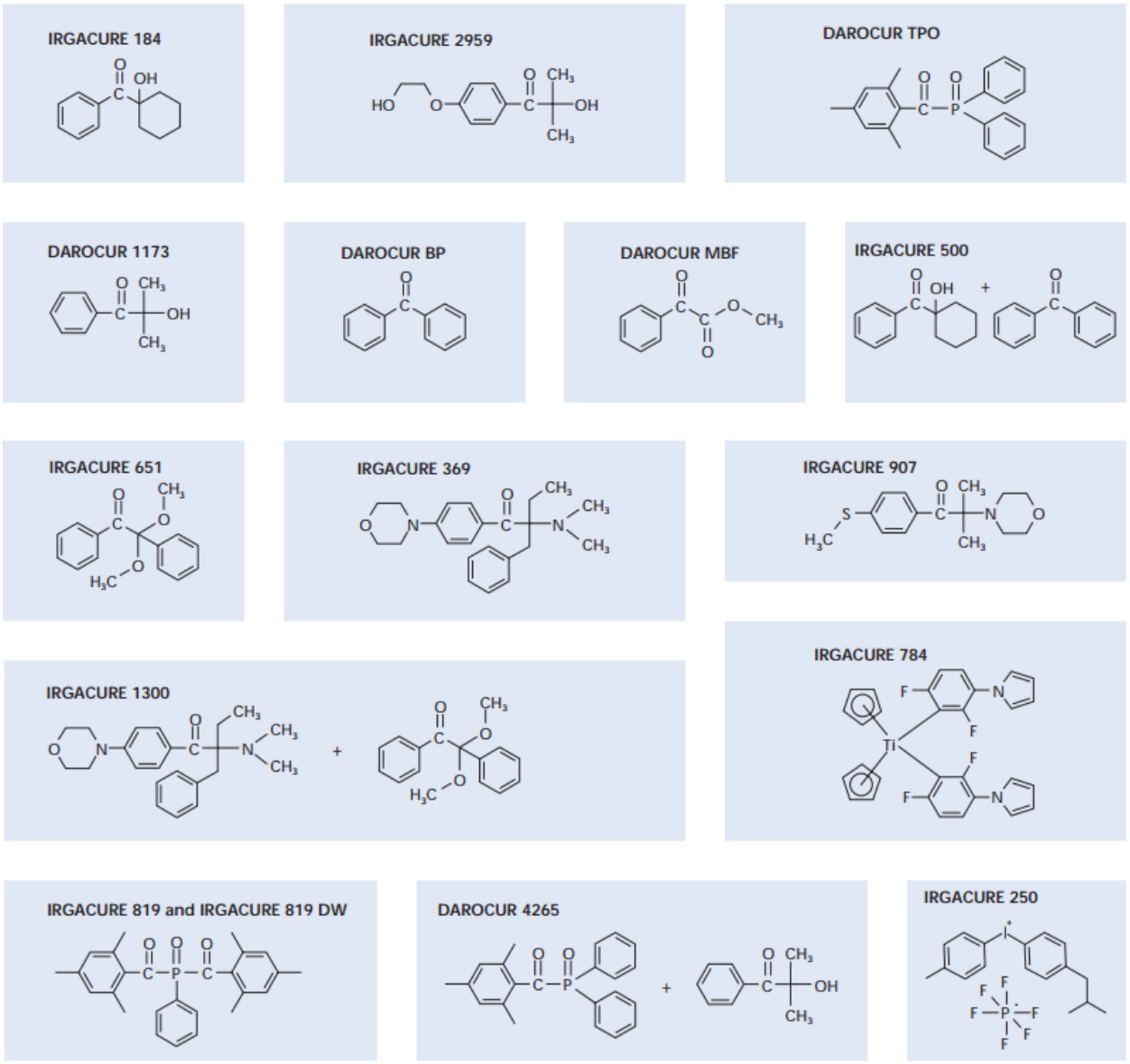

***Figure 31**: selected IRGACURE and DAROCUR products from CIBA Specialty Chemicals.*

dimerization occurs. Unfortunately C4X showed extreme photostability and did not polymerize under the irradiaton of a Wood lamp at both 254 nm and 365 nm. This is probably due to the intrinsically low order of a spun-cast film, which makes the possibility of a favourable mutual position of the double bonds unlikely at best.

Nonetheless, since cinnamic acid dimerization is competitive with the cinnamic double bond isomerization (a process favored at low irradiation intensities), we exposed a C4X film deposited on a glass slides to a stronger UV source (50 mW cm-2) for up to 30 min. Once again, no change was observed in the chemical structure (as asserted by NMR) or in the solubility of the film.

We thus dropped the cinnamic esters dimerization scheme and turned to acrylic derivatives. In this case, the use of an appropriate photoinitiator is required. After some trials we decided to use IRGACURE 651, which is part of a trademarked list of photoinitiators working in the UV light region (250-350 nm range).

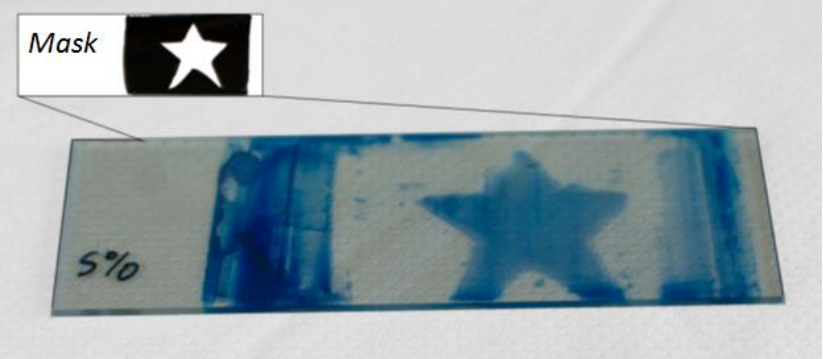

***Figure 32**: A4X film on a glass slide after UV curing under Wood lamp and acetone developing of the film. Inset: cartoon representation of the mask used for lithography.*

These compounds are widely used in industry for resins and photocuring, and range from ionic solids to liquids.

Figure 32 shows the very first photopolymerization test we made, based on squaraine A4X. We cast a thick film of a 5% w/w IRGACURE 651 and A4X in 1,2-dichloroethane (10 mg/ml) on a microscope slide. The film was intentionally very thick in order to allow identification of the photocrosslinking by naked eye. The film was partially protected with a black mask and exposed under nitrogen flux to 365 nm UV light of a Wood lamp for 45 min, while keeping the light source 2 cm away from the film surface.

The mask was removed and the film developed by immersion and sonication in an acetone bath. Derivative A4X is freely soluble in acetone, and in fact the unexposed portion of the film was completely washed away. Conversely, the exposed area became totally insoluble in the developing solvent, thus confirming the polymerization/crosslinking process.

The comparison of the UV-Vis absorption spectra of A4X before and after photo-crosslinking does not show sign of photoinduced degradation. The only minor band shape changes can be attributed to a slightly different, photocrosslinking-perturbed aggregation behavior.

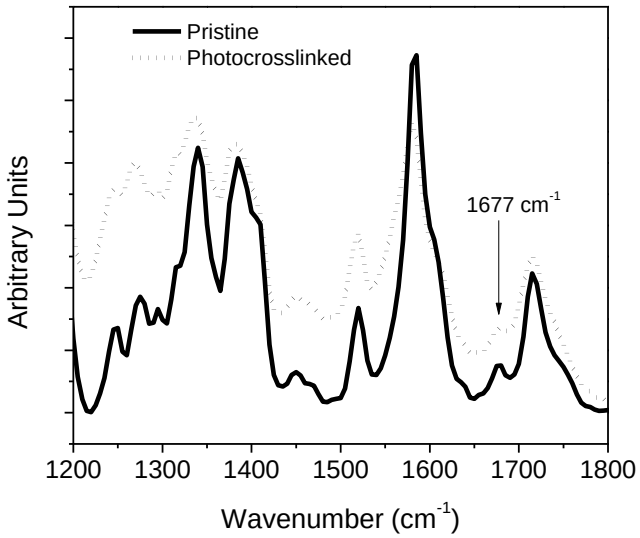

***Figure 33:** FTIR-ATR absorbance of a solid film of pristine and photocrosslinked squaraine.*

Morphological Characterization

We characterized the process by means of FTIR spectroscopy working in ATR configuration. **Figure 33** also shows that the band at 1677 cm^{-1}, previously attributed to the stretching of the acrylic double bond, progressively disappears at increasing exposition times. After 30 min, the process is essentially complete.

We investigated the surface of these films by using AFM techniques to further understand the effect of photopolymerization on the morphology. By lowering the photoinitiator loading (3.5% w/w) and deposing a chloroform film by spincasting at 900 rpm we were able to obtain macroscale-uniform films which were then subjected to curing under Wood lamp for 45 minutes.

By using the AFM mechanical stage we were able to scan the surface, cure the films and then move the samples back to the same macroarea (~1 mm^2). **Figure 34** reports our findings.

It is easy enough to notice that the initial surface roughness (expressed as root mean square variability of the peak and pits heights in the area scan) goes unchanges after and before treatment, if not for a small ~10% variation which might depend on the position of the scan (**Figure 34a** and 34**b**).

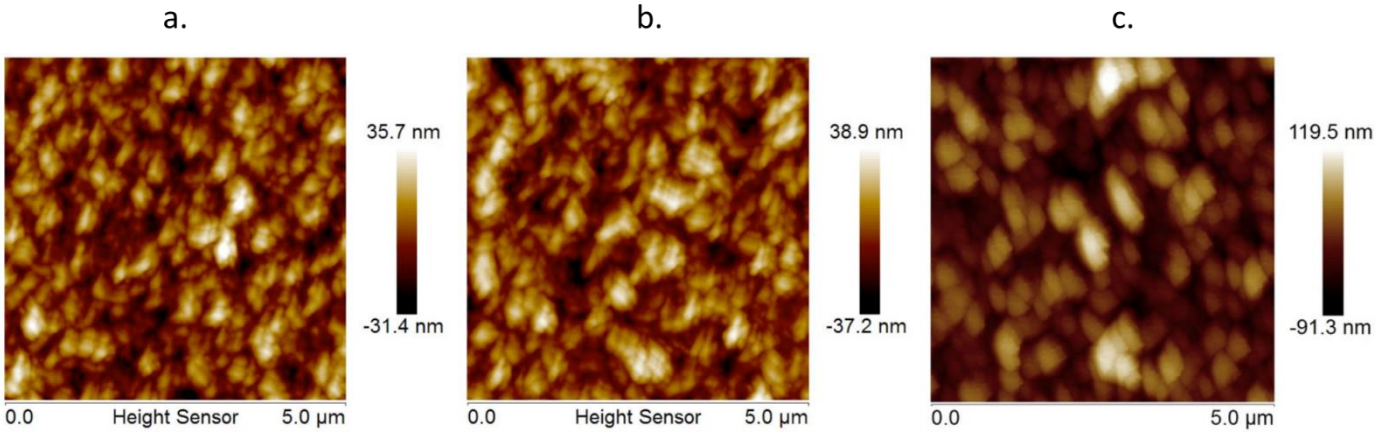

Figure 34: *AFM height scans of A4X films on PEDOT:PSS surfaces. (a) Pre-UV treatment; (b) Post-UV treatment; (c) Film after acetone development.*

On the other hand, though, the development of the film causes major delamination/dissolution of low molecular weight chains. The morphology of the film is not unaffected by the removal of material, and develops pitches which can be 200 nm high, bottom to top.

This phenomenon by itself could be really interesting for the development of a very high contact surface area bulk heterojunction, allowing for a fast and cheap interdigitated nanostructure. The possibility of developing nanostructures by diffraction photolithography is also very interesting, with the *caveat* of a wavelength-driven resolution in the structures one is able to form.

By increasing the spinning velocity of the deposition we were able to obtain smoother and thinner films. The result shows a reduced rms for the untreated sample, and an interesting shrinking effect of the film after UV-assisted *in situ* polymerization. This is especially highlighted by the trenches forming in **Figure 35b**, where the existence of clear fault lines in the material has been underlined artificially to indicate where this phenomenon takes place.

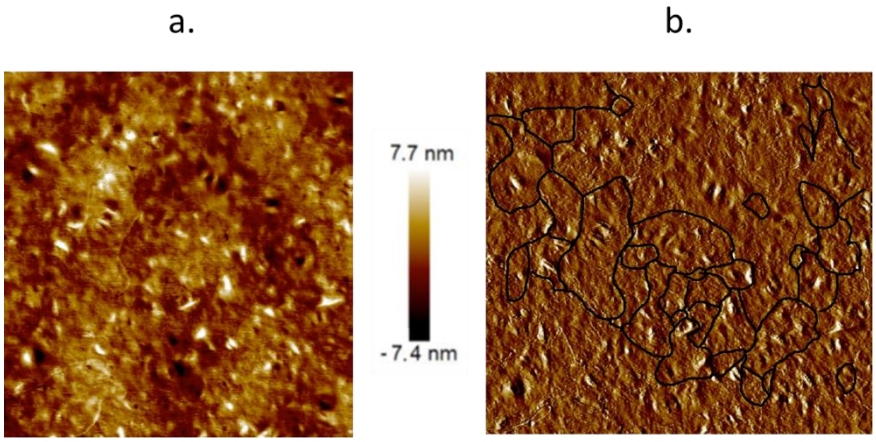

Figure 35: *(a) AFM height scan map of a A4X film on MoOx after UV treatment; (b) the trenches where the shrinkage of the material has occurred have been highlighted in black.*

In order to ascertain the dynamic behavior of the materials upon UV exposition we characterized thin films of squaraines A2X and A4X by thin film X-Ray Diffraction (XRD) experiments in θ-2θ configuration before and after exposure. **Figure 36** shows that both pristine films feature a reflection centered on θ~4.3,

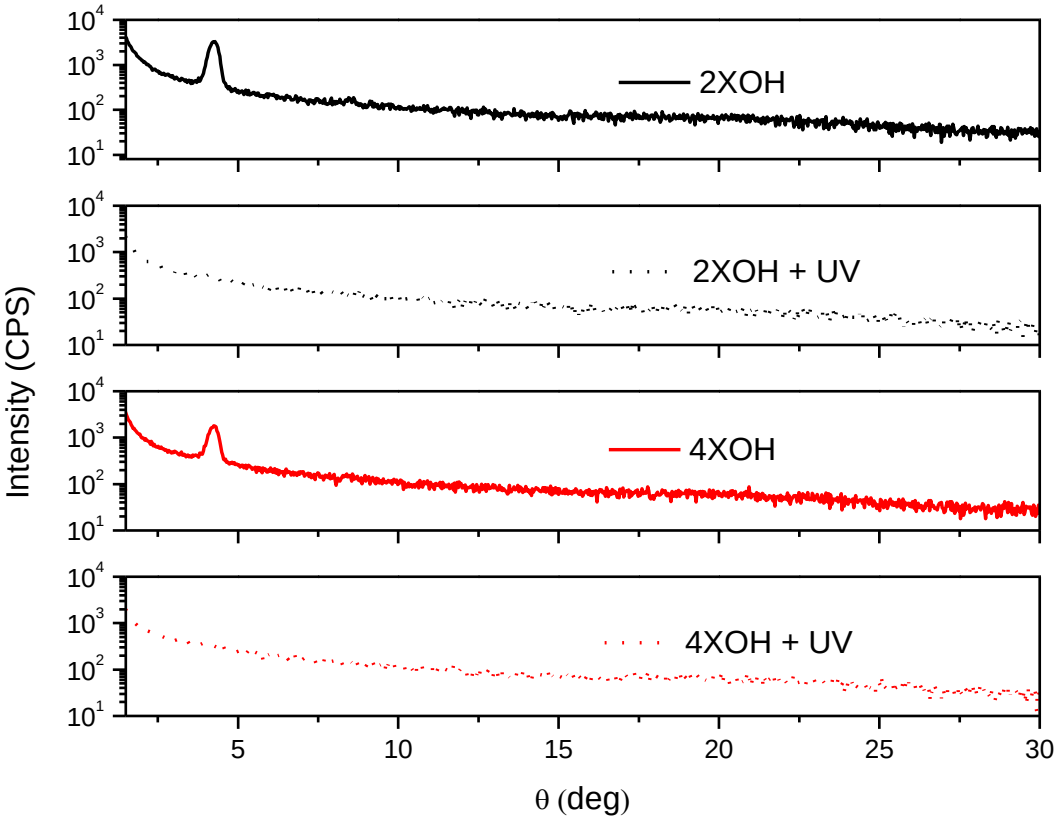

Figure 36: *XRD scans of thin films of reported materials; the solid lines indicate films before treatment, dotted lines the same film after treatment.*

which can be attributed to the π stack of neighboring squaraines.

Upon exposure, the peak disappears in both cases, hinting at a complete amorphization of the film. The result is in agreement with what was previously observed by Mc Colluog et al. while irradiating photosensitive liquid crystalline mesophases. The reduced rotational freedom of the lateral chains negatively affects the packing capability of the conjugated cores.

We are actively working on both the inclusion of adhesion promoter in the active layer formulation as well as on the pretreatment of the deposition substrate with very thin films of a low polarity primer in order to avoid the delamination problems we have had.

Photovoltaic Performance

We preliminarily tested the OPV performances of acrylic derivatives as the Donor component in a BHJ configuration having PC61BM as the Acceptor. In all of the cases we compared the performances of identical devices, with and without UV treatment. Table X shows all the relevant device characterizations.

***Table 1**: OPV results for the relevant materials reported herein.*

Compound	ratio	IC	V_{OC}	J_{SC}	FF	η	Mult.
A4X	1:2.5	N	0.50	5.96	34	1.00	-
A2X	1:1	Y	0.46	3.52	27	0.42	13.5
A2XOH	1:2	N	0.57	1.70	33	0.32	
A2XOH	1:2	Y	0.27	1.45	32	0.12	0.38
A2XOH	1:1	N	0.35	0.63	27	0.06	
A2XOH	1:1	Y	0.45	0.70	31	0.10	1.7
A4XOH	1:2	N	0.27	0.42	25	0.03	
A4XOH	1:2	Y	0.32	0.71	37	0.08	2.7
A4XOH	1:1	N	0.14	0.07	26	0.002	
A4XOH	1:1	Y	0.23	0.44	28	0.03	15

Derivatives **A2X** and **A4X**, both featuring short alkyl chains connecting the conjugated core and the photoresponsive functionalities, gave opposite results: while untreated **A4X**-based devices afforded conversion efficiencies comparable with reported literature performances for other simple alkyl chain substituted compounds (1%,), the corresponding UV cross-linked devices did not show any photocurrent and basically behaved as diodes.

Details of the device stack are as following: the active layer is a mixture of A4X and PCBM-61 in a 1:2.5 ratio, and it is sandwiched between a Molybdenum Oxide (EBL) and a LiF (HBL) layers, capped with Aluminum electrodes. Its photovoltaic characterization can be found in **Figure 37**.

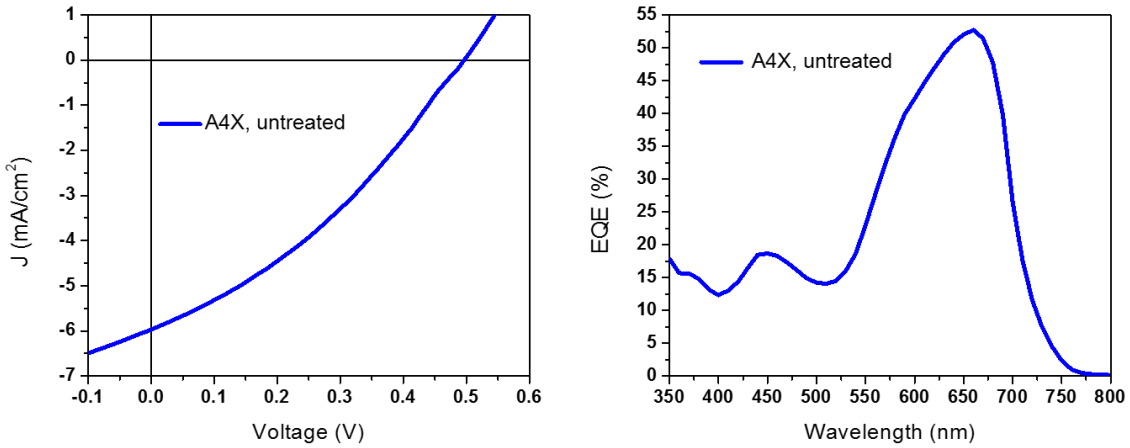

Figure 37: *photovoltaic characterization of the best-performing A4X bulk heterojunction; (left) J-V curve at 1.5 AM illumination (active area 8 mm²); (right) EQE characterization of the solar cell.*

The low FF of the cell comes mainly from the high resistivity of the squaraines we employ, and will be recurring throughout the device characterizations. The EQE shows that the vast majority of the photogenerated charge carriers arise from the absorption of the squaraine. This is easily understandable when one considers that the molar extinction coefficients for PCBM and A4X are ~5.000 mol L^{-1} cm^{-1} for PCBM versus ~250.000 mol L^{-1} cm^{-1} for A4X, hence the absorption of a photon by the squaraine is ~50 times more likely. It is easy to notice the occurrence of a blue-shifted shoulder in the EQE spectrum with respect to the main peak, probably arising from the formation of higher energy H-aggregates after the annealing at 50°C.

Conversely, unexposed A2X based devices featured a barely measurable efficiency (0.035 %), and, upon UV exposure reached efficiencies similar to unexposed A4X (0.46 % with a remarkable 13.5 enhancement factor). Such surprising result might be explained based on the interfaces structuring we observed in the case of pure A4X films.

The presence on the same molecule of 4 crosslinkable functionalities leads to perturbation of the π-π stacking between neighboring molecules, as already observed by Mc Colloug, as well as extensive cracking induced by shrinking. In the case of a blend, the formation of strongly phase-segregated Donor embedded in an Acceptor matrix completely impairs any photovoltaic activity.

Conversely, in the case of A2X the performance improvement upon photopolymerization is likely due to the better resolved BHJ morphology. A2X is much more soluble than A4X, meaning that the bulk heterojunction is mainly featureless because of the low tendency to phase segregation while in mixture with the Acceptor. As such, pristine cells have almost no OPV activity.

When UV treated, the formation of a Donor photocrosslinked phase triggers segregation of the Acceptor, thus enhancing all cell parameters. The formation of well-defined domains of squaraine is also hinted at by the massive H-aggregate peak in the EQE plot. The cell behavior remains in any case contact-resistance limited, as is particularly evident by the S kink of the J-V curve of the UV polymerized device.

While designing hydroxyl-functionalized squaraines A2XOH and A4XOH we elongated the alkyl chains connecting conjugated core and photoreactive residue mainly to increase solubility, hoping it would help

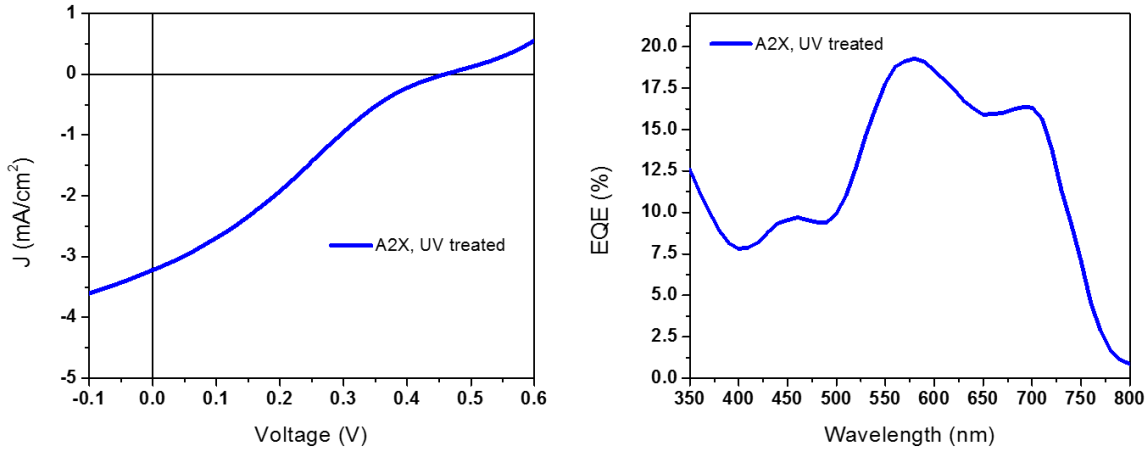

Figure 38: *photovoltaic characterization of the best-performing A2X bulk heterojunction. (left) J-V curve; (right) EQE curve.*

us reproduce A2X UV-induced segregation behaviour. We also replaced the methacrylic residue with an acrylic one, in analogy with the design guidelines employed by the Reynolds group.

As a general rule, the tetrafunctionalized derivative A4XOH gave very poor results, both as pristine and as UV polymerized material. In particular, we found that cells based on a 1:1 by weight ratio of A4XOH and PCBM have negligible efficiencies prior to UV exposure. The very low Voc and Jsc values essentially show that there hardly is any BHJ structure and that the blend is essentially insulating. UV polymerization improves the efficiency by a factor of 15, yet still providing very low, Voc and Jsc limited, efficiencies (0.03 %).

The increase of the PCBM ratio form 1:1 to 1:2 by weight improves the pristine device efficiencies by one order of magnitude (0.03%), further enhanced by the UV treatment (0.08 %). Such results have in any case a very limited scope, being the efficiencies so low.

The inspection of A2XOH based cells results is more promising. In fact, although efficiencies are still pretty low, all cells we prepared were working properly, with reproducible results. As in the previous case, the 1:2 by weight Donor Acceptor ratio gave best results, with a peak efficiency of 0.32 % for unexposed cells. UV exposure caused a strong decrease in the Voc, likewise for increased contact resistance due to contact delamination.

The opposite is true for the 1:1 by weight ratio cells, where UV polymerization improved both Voc (0.45 V) and efficiency (0.10 %). We believe that, due to the very low conductivity of the model squaraines we made, the nature of the contact/active layer interface is crucial for device performances. Our trends show that an increase of PCBM concentration usually improves efficiencies because of higher electron mobilities and additional absorption in the 300-450 nm range. At the same time, the decrease in the photoreactive Donor concentration favors extensive phase segregation upon photocrosslinking, with the consequent reduction in both Voc and photocurrent.

As such, our preliminary data show that the active photoresists approach might be a valuable entry for OPV devices, provided that the cross-linking ratio is controlled, and that the performances of the resist itself are improved. We stress however that the A2X and A2XOH data show that it is possible to prepare

an active (without any thermal and/or solvent annealing) photoresists retaining the same order of magnitude in the conversion efficiency with respect to structurally related UV-inert compounds.

Although largely improvable, our results represent the first successful application of the photoresist chemistry to the donor of a bulk heterojunction for organic photovoltaics.

EXPERIMENTAL

Active layer fabrication: All steps taken are followed by Nitrogen spray cleaning. Pre-patterned ITO-coated glass (Thin Film Devices, Inc.) with a sheet resistance of ~10Ω/□ is used as the substrate. The slides are cleaned by sequential sonication at 50°C in soap water, DI water, methanol, isopropanol, and acetone. The substrates were then exposed to oxygen plasma for 5 minutes (residual pressure 0.3-0.4 mTorr). For PEDOT:PSS HBL an aqueous solution of it was spun-cast at 5000 rpm for 30 seconds. After cleaning the electrical contacts, the substrates are annealed in air at 160 ºC for 30 min and dried in a glovebox. For MoOx HBL 6 nm of MoO_3 are evaporated at a base pressure of ~10^{-6} Torr, then the surface is oxygen plasma treated for 5 minutes and brought in the glovebox.

4-8 mg/mL active layer solutions in anhydrous chloroform of A2X, A4X, A2XOH and A4XOH and PCBM in the appropriate weigth ratios are prepared in a glovebox. For best device performance, active layers of A2X and A2XOH are spun cast at 2500 rpm, while A4X and A4XOH were spuncast at 3000 rpm.

The thin films were photocrosslinked using a Wood lamp (1 cm distance) for 30 minutes at 365 nm in glovebox nitrogen atmosphere.

Solar cell fabrication: Contacts are again cleaned and a thin 1.0 nm layer of LiF and 120 nm of Al are then thermally evaporated through a shadow mask at a base pressure of ~10^{-6} Torr.

Device characterization, J-V characteristics are measured under AM1.5G light (100 mW/cm2) using the Xe arc lamp of a Spectra-Nova Class A solar simulator. The light intensity is calibrated using an NREL-certified monocrystalline Si diode coupled to a KG3 filter to bring spectral mismatch to unity. A Keithley 2400 source meter is used for electrical characterization. The area of all devices is 8 mm^2.

EQEs are characterized using an Oriel model QE-PV-SI instrument equipped with a NIST-certified Si diode. Monochromatic light is generated from an Oriel 300W Helium lamp source through 2 mechanical monochromators.

AFM characterization: AFM images were collected on a Bruker ICON System at a frequency of 1.0 Hz in tapping mode, using ACTA-50 n-doped Silicon tips (<10 nm tip radius) from AppNano. Images were elaborated using NanoScope 1.40.

Synthesis of **3**

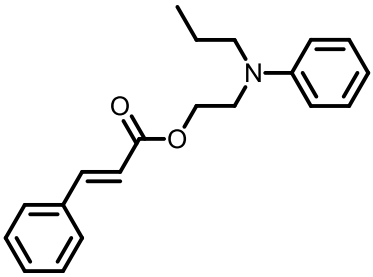

Compound **1** (0.932 g, 5.64 mmol) is dissolved in 100 ml of toluene. Cinnamic acid (0.918 g, 6.20 mmol) and paratoluen sulfonic acid (0.057 g, 0.56 mmol) are added to the solution and the mixture is refluxed for 20 hours in a Dean-Stark apparatus. Solvent is evaporated at reduced pressure and the obtained viscous oil is redissolved in dichloromethane, washed with brine and aqueous potassium carbonate. The organic phase is dried on magnesium sulfate, solvent is evaporated at reduced pressure and the crude is purified through a silica gel column (DCM:toluene 8:2) to afford the pure material as a viscous yellow oil (yield 57%).

^{1}H-NMR ($CDCl_3$ @ 500 MHz): δ 7.70, d, 2H; δ 7.53, m, 4H; δ 7.41, m, 6H; δ 7.25, m, 4H; δ 6.79, m, 4H; δ 6.72, m, 2H; δ 6.45, d, 2H; δ 4.39, m, 4H; δ 3.65, m, 4H; δ 3.46, m, 4H; δ 1.21, m, 6H.

^{13}C-NMR ($CDCl_3$ @ 126 MHz): δ 167.78, 148.54, 146.05, 135.24, 131.26, 130.26, 129.79, 129.00, 118.67, 117.13, 112.94, 62.77, 49.80, 46.16, 13.19.

Synthesis of **C2X**

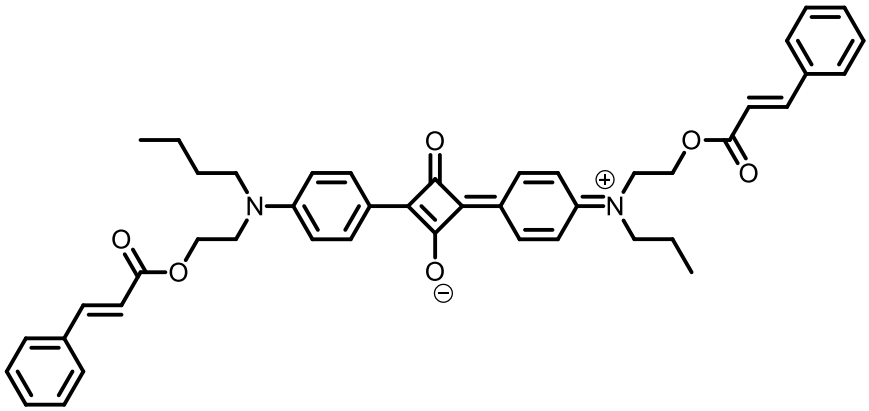

Compound **3** (0.730 g, 2.47 mmol) is dissolved in 30 ml of a n-butanol/toluene 1:1 mixture. Squaric acid (0.140 g, 1.23 mmol) is added and the mixture is refluxed for 5 hours. Solvent is removed at reduced pressure and the solid is triturated with diethyl ether, affording the product as a black solid (27%).

^{1}H-NMR ($CDCl_3$ @ 500 MHz): δ 8.43, d, 4H; δ 7.68, d, 2H; δ 7.51, m, 4H, δ 7.38, m, 6H; δ 6.87, d, 4H; δ 6.39, d, 2H; δ 4.44, m, 4H; δ 3.82, m, 4H; δ 3.62, m, 4H; δ 1.30, m, 6H.

^{13}C-NMR ($CDCl_3$ @ 126 MHz): δ 190.65, 184.02, 167.57, 154.50, 146.85, 134.92, 134.42, 131.48, 129.82, 129.10, 121.14, 117.86, 113.39, 62.14, 49.84, 46.88, 13.28.

Synthesis of **4**

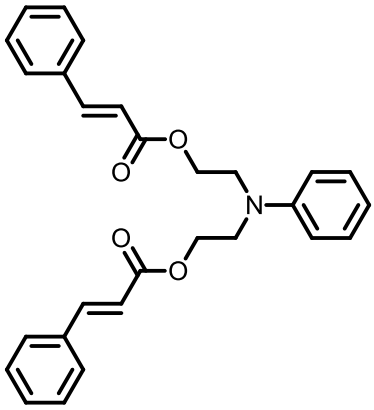

Compound **2** (30.000 g, 165.50 mmol) is dissolved in 300 ml of toluene. Cinnamic acid (73.000 g, 364.20 mmol) and paratoluen sulfonic acid (5.600 g, 16.50 mmol) are added to the solution and the mixture is refluxed for 200 hours in a Dean-Stark apparatus. Solvent is evaporated at reduced pressure and the obtained viscous oil is redissolved in dichloromethane, washed with brine and aqueous potassium carbonate. The organic phase is dried on magnesium sulfate, solvent is evaporated at reduced pressure and the crude is purified through a silica gel column (DCM:toluene 8:2) to afford the pure material as a viscous yellow oil (yield 48%).

^{1}H-NMR ($CDCl_3$ @ 500 MHz): δ 7.69, d, 2H; δ 7.52, m, 4H; δ 7.39, m, 6H; δ 7.28, m, 3H; δ 6.87, d, 2H; δ 6.77, t, 1H; δ 6.45, d, 2H; δ 4.43, t, 4H; δ 3.77, t, 4H.

^{13}C-NMR ($CDCl_3$ @ 126 MHz): δ 167.32, 147.75, 145.74, 134.75, 130.85, 129.98, 129.35, 128.62, 118.12, 117.58, 112.73, 62.14, 50.40.

Synthesis of **C4X**

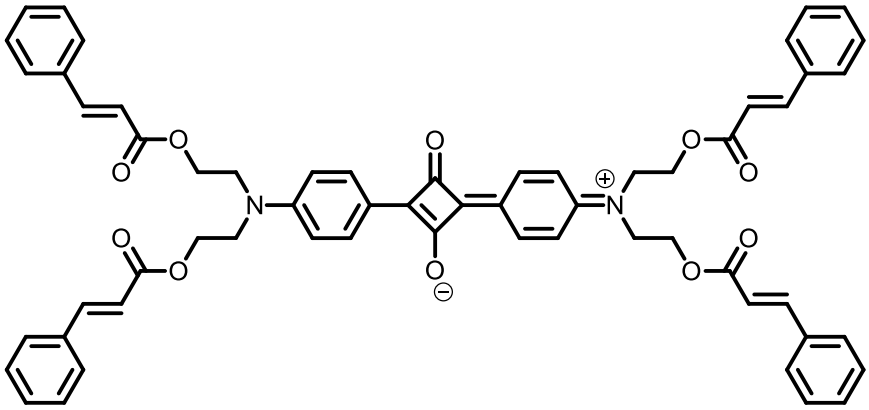

Compound **4** (5.000 g, 11.32 mmol) is dissolved in 40 ml of isopropanol. Squaric acid (0.645 g, 5.66 mmol) and triethyl orthoformate (10 ml) are added and the mixture is refluxed for 4 hours. A blue powder is filtered on a Hirsch funnel and recrystallized from ethanol to afford the pure product (10%).

^{1}H-NMR ($CDCl_3$ @ 500 MHz): δ 8.48, d, 4H; δ 7.67, d, 2H; δ 7.50, m, 4H, δ 7.37, m, 6H; δ 6.91, d, 4H; δ 6.40, d, 2H; δ 4.49, t, 4H; δ 3.93, t, 4H.

^{13}C-NMR ($CDCl_3$ @ 126 MHz): δ 191.00, 183.51, 167.56, 155.00, 146.96, 134.87, 134.75, 131.50, 129.82, 129.13, 121.53, 117.75, 113.88, 61.96, 50.82.

Synthesis of **A2X**

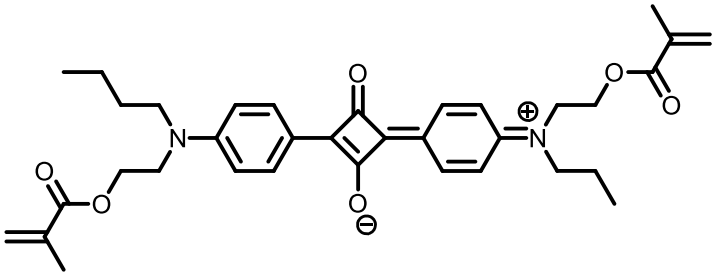

Compound **2** (3.870 g, 23.40 mmol) is dissolved in 80 ml of toluene. Triethylamine (2.610 g, 25.80 mmol) is added to the solution and the mixture cooled down to 0°C via ice bath. A solution of methacryloyl chloride (2.680 g, 25.60 mmol) in 20 ml of toluene is added dropwise to the mixture. Reaction is stirred for 12 hours at room temperature. The white precipitate is filtered away and the organic phase reduced by evaporating the solvent at reduced pressure. The crude is filtered on a silica plug using DCM as a solvent, affording a pale yellow oil as intermediate. This intermediate is immediately dissolved in isopropanol (10 ml), to which both squaric acid (0.570 g, 5.00 mmol) and triethyl orthoformate (1 ml) are added. Mixture is refluxed for 3 hours and the precipitate is filtered away on a Hirsch funnel. The crude is recrystallized from methanol to afford the final product as a blue powder (yield 7%).

^{1}H-NMR ($CDCl_3$ @ 500 MHz): δ 8.41, d, 4H; δ 6.84, d, 4H; δ 6.08, s, 2H, δ 5.59, m, 2H; δ 4.39, m, 4H; δ 3.79, m, 4H; δ 3.59, m, 4H; δ 1.92, s, 6H; δ 1.28, m, 6H.

^{13}C-NMR ($CDCl_3$ @ 126 MHz): δ 190.73, 184.03, 168.03, 154.48, 136.53, 134.37, 127.40, 121.13, 113.34, 62.41, 49.66, 46.69, 19.17, 13.19.

Synthesis of **A4X**

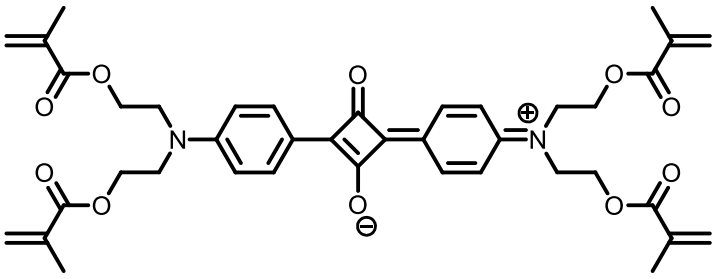

Compound **4** (2.200 g, 12.29 mmol) is dissolved in 80 ml of toluene. Triethylamine (2.720 g, 26.60 mmol) is added to the solution and the mixture cooled down to 0°C via ice bath. A solution of methacryloyl chloride (2.680 g, 25.60 mmol) in 20 ml of toluene is added dropwise to the mixture. Reaction is brought out for 12 hours at room temperature. The white precipitate is filtered away and the organic phase reduced by evaporating the solvent at reduced pressure. The crude is filtered on a silica plug using DCM as a solvent, affording a pale yellow oil as intermediate. This intermediate is immediately dissolved in

isopropanol (10 ml), to which both squaric acid (0.500 g, 4.40 mmol) and triethyl orthoformate (1 ml) are added. Mixture is refluxed for 3 hours and the precipitate is filtered away on a Hirsch funnel. The crude is recrystallized from ethanol to afford the final product as a dark green (yield 27%).

^{1}H-NMR ($CDCl_3$ @ 500 MHz): δ 8.42, d, 2H; δ 6.93, d, 2H; δ 6.07, s, 2H, δ 5.59, m, 2H; δ 4.41, m, 4H; δ 3.86, m, 4H; δ 1.91, s, 6H.

^{13}C-NMR ($CDCl_3$ @ 126 MHz): δ 192.58, 183.75, 167.96, 154.86, 136.45, 134.51, 127.48, 121.74, 113.64, 62.12, 50.32, 19.16.

Synthesis of **7**

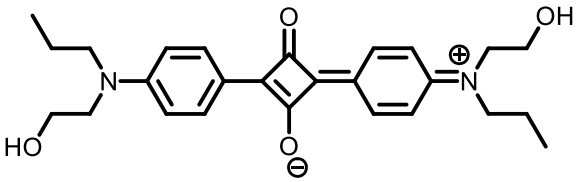

Compound **2** (2.000 g, 12.10 mmol) is dissolved in 60 ml of a n-butanol/toluene 1:1 mixture squaric acid (0.690 g, 6.05 mmol) is added to the solution and the mixture is refluxed for 6 hours in a Dean-Stark apparatus. The precipitate is filtered away on a Hirsch funnel. The crude is washed with toluene directly on the filter to afford the final product as a light blue powder (yield 15%).

^{1}H-NMR (DMSO-d_6 @ 500 MHz): δ 8.11, d, 4H; δ 6.99, d, 4H; δ 4.91, s, 2H, δ 3.61, m, 12H; δ 1.18, m, 6H.

^{13}C-NMR (DMSO-d_6 @ 126 MHz): δ 186.72, 183.07, 154.91, 132.96, 119.89, 114.46, 59.88, 53.63, 47.11, 13.48.

Synthesis of **6-bromohexyl acrylate**

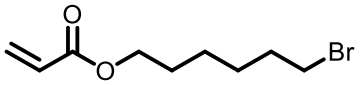

In a three-necked round bottomed flask equipped with a calcium chloride trap triethylamine (3.04 g, 30.05 mmol) and 6-bromoesanol (5.00 g, 27.61 mmol) are dissolved in 30 ml of dry toluene. Mixture is cooled to -10°C via salt and ice bath, and a solution of acryloyl chloride (2.72 g, 30.05 mmol) in 10 ml of dry toluene is added dropwise. The reaction warmed to room temperature and stirred for 48 hours. The organic phase is subsequently washed with a 5% w/w aqueous solution of sodium carbonate, a 5% w/w aqueous hydrochloric acid solution and with brine. Organic phase is then dried on magnesium sulfate and the solvent is evaporated at reduced pressure to afford the product as a yellowish oil (yield 77%).

^{1}H-NMR ($CDCl_3$ @ 500 MHz): δ 6.40, d, 1H; δ 6.12, dd, 1H; δ 5.82, d, 1H; δ 4.16, t, 2H; δ 3.41 ,t, 2H; δ 1.88, m, 2H; δ 1.69, quin, 2H; δ 1.45, m, 4H.

^{13}C-NMR ($CDCl_3$ @ 126 MHz): δ 166.28, 130.55, 128.54, 64.39, 33.68, 32.60, 28.45, 25.29, 25.17.

Synthesis of **9**

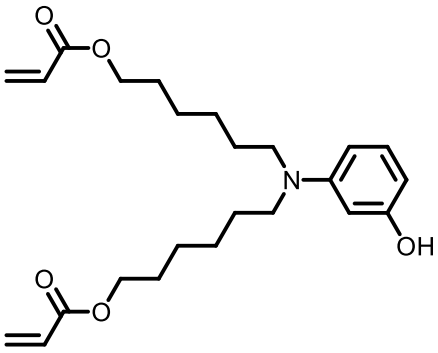

3-aminophenol (compound **8**, 35.00 g, 320.00 mmol), bromooctane (62.31 g, 323.10 mmol) and finely ground sodium carbonate (38.42 g, 350.12 mmol) are added to 70 ml of isopropanol. The mixture is refluxed for 10 hours. The precipitate is filtered away and the organic phase is evaporated at reduced pressure to afford a brown oil, which is then triturated in a heptane/ethyl acetate 4:1 mixture. The solid is filtered away and the crude is purified by column chromatography on silica (eluent: heptane/ethyl acetate 4:1). After solvent evaporation the product is obtained as a white powder (yield 37%).

Synthesis of **A4XOH**

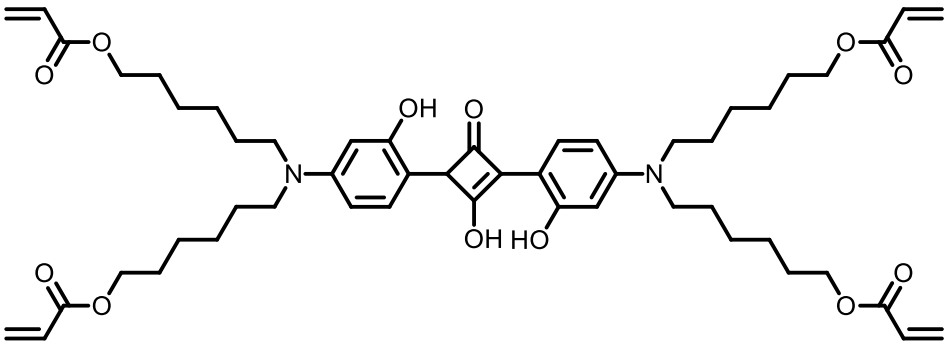

Compound **9** (0.950 g, 2.30 mmol) is dissolved in 3 ml of isopropanol. Squaric acid (0.130 g, 1.15 mmol) and triethyl orthoformate (2 ml) are added and the mixture is refluxed for 4 hours. Volatiles are evaporated at reduced pressure and the resulting dark wax is dissolved in ethyl acetate and purified by column chromatography, to afford the product as a blue wax (yield 15%).

Synthesis of **10**

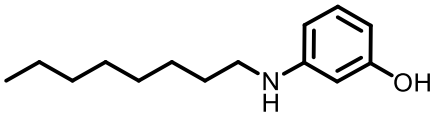

3-aminophenol (compound **8**, 35.00 g, 320.00 mmol), bromooctane (62.31 g, 323.10 mmol) and finely ground sodium carbonate (38.42 g, 350.12 mmol) are added to 70 ml of isopropanol. The mixture is refluxed for 10 hours. The precipitate is filtered away and the organic phase is evaporated at reduced pressure to afford a brown oil, which is then triturated in a heptane/ethyl acetate 4:1 mixture. The solid

is filtered away and the crude is purified by column chromatography on silica (eluent: heptane/ethyl acetate 4:1). After solvent evaporation the product is obtained as a white powder (yield 37%).

^{1}H-NMR ($CDCl_3$ @ 500 MHz): δ 7.83, s, 2H; δ 7.20, t, 1H; δ 7.14, t, 1H; δ 6.99, dd, 1 H; δ 6.84, dd, 1H; δ 3.26, t, 2H; δ 1.78, m, 2H; δ 1.16, s, 10 H; δ 0.84, t, 3H.

^{13}C-NMR ($CDCl_3$ @ 126 MHz): δ 157.61, 135.54, 130.98, 116.99, 113.79, 109.77, 52.60, 31.60 , 29.00, 28.88, 26.50, 25.46, 22.50, 14.00.

Synthesis of **11**

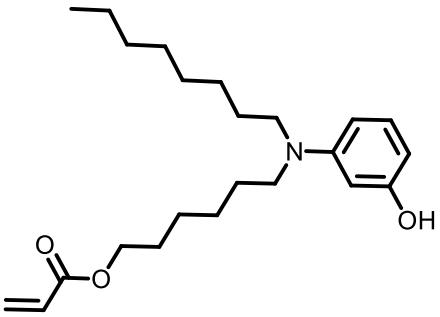

Compound **10** (0.94 g, 4.25 mmol), bromohexyl acrylate (1.30 g, 5.52 mmol) and finely ground sodium carbonate (0.90 g, 8.50 mmol) in 5 ml of isopropanol is refluxed for 74 hours. The precipitate is filtered away and the organic phase is evaporated at reduced pressure to afford a brown oil which is purified by column chromatography (eluent: petroleum ether/ethyl acetate 5:1). After evaporation the product is obtained as a yellowish oil (yield 40%).

Synthesis of **A2XOH**

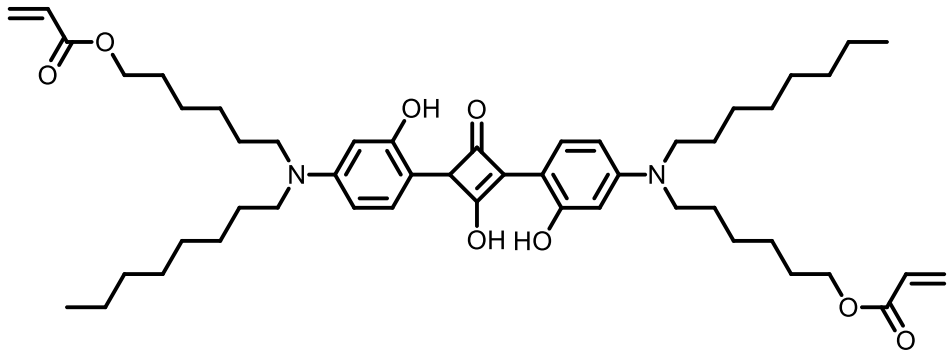

Compound **11** (0.600 g, 2.30 mmol) is dissolved in 3 ml of isopropanol. Squaric acid (0.130 g, 1.15 mmol) and triethyl orthoformate (2 ml) are added and the mixture is refluxed for 4 hours. Volatiles are evaporated at reduced pressure and the resulting dark wax is dissolved in ethyl acetate and purified by column chromatography, to afford the product as a blue powder (yield 15%).

BIBLIOGRAPHY

1. Ibach, H. & Lüth, H. *Solid-State Physics: An Introduction to Principles of Materials Science*. **4,** 536 (Springer Science & Business Media, 2009).

2. Kittel, C. *Introduction to Solid State Physics*. **11,** 704 (Wiley, 2004).

3. Wannier, G. The Structure of Electronic Excitation Levels in Insulating Crystals. *Phys. Rev.* **52,** 191–197 (1937).

4. Müller, G. The Czochralski Method - where we are 90 years after Jan Czochralski's invention. *Cryst. Res. Technol.* **42,** 1150–1161 (2007).

5. Braga, A. F. B., Moreira, S. P., Zampieri, P. R., Bacchin, J. M. G. & Mei, P. R. New processes for the production of solar-grade polycrystalline silicon: A review. *Sol. Energy Mater. Sol. Cells* **92,** 418–424 (2008).

6. Shockley, W. & Queisser, H. J. Detailed Balance Limit of Efficiency of p-n Junction Solar Cells. *J. Appl. Phys.* **32,** 510 (1961).

7. Green, M. A. Thin-film solar cells: review of materials, technologies and commercial status. *J. Mater. Sci. Mater. Electron.* **18,** 15–19 (2007).

8. Conibeer, G. Third-generation photovoltaics. *Mater. Today* **10,** 42–50 (2007).

9. Cheyns, D., Gommans, H., Poortmans, J., Genoe, J. & Heremans, P. Stacked organic solar cells increase efficiency. *SPIE Newsroom* (2007). doi:10.1117/2.1200704.0731

10. Tvingstedt, K., Andersson, V., Zhang, F. & Inganäs, O. Folded reflective tandem polymer solar cell doubles efficiency. *Appl. Phys. Lett.* **91,** 123514 (2007).

11. O'Regan, B. & Grätzel, M. A low-cost, high-efficiency solar cell based on dye-sensitized colloidal TiO2 films. *Nature* **353,** 737–740 (1991).

12. Arici, E., Sariciftci, N. S. & Meissner, D. Hybrid Solar Cells Based on Nanoparticles of CuInS2 in Organic Matrices. *Adv. Funct. Mater.* **13,** 165–171 (2003).

13. Bi, D. *et al.* Device Performance Related to Amphiphilic Modification at Charge Separation Interface in Hybrid Solar Cells with Vertically Aligned ZnO Nanorod Arrays. *J. Phys. Chem. C* **115,** 3745–3752 (2011).

14. Jin, Z. *et al.* Efficient Electron Transfer Ruthenium Sensitizers for Dye-Sensitized Solar Cells. *J. Phys. Chem. C* **113,** 2618–2623 (2009).

15. Abbotto, A. *et al.* Di-branched di-anchoring organic dyes for dye-sensitized solar cells. *Energy Environ. Sci.* **2,** 1094 (2009).

16. Yella, A. *et al.* Porphyrin-sensitized solar cells with cobalt (II/III)-based redox electrolyte exceed 12 percent efficiency. *Science* **334,** 629–34 (2011).

17. Yanagida, S., Yu, Y. & Manseki, K. Iodine/iodide-free dye-sensitized solar cells. *Acc. Chem. Res.* **42,** 1827–38 (2009).

18. Kojima, A., Teshima, K., Shirai, Y. & Miyasaka, T. Organometal halide perovskites as visible-light sensitizers for photovoltaic cells. *J. Am. Chem. Soc.* **131,** 6050–1 (2009).

19. Baikie, T. *et al.* Synthesis and crystal chemistry of the hybrid perovskite (CH3NH3)PbI3 for solid-state sensitised solar cell applications. *J. Mater. Chem. A* **1,** 5628 (2013).

20. Burschka, J. *et al.* Sequential deposition as a route to high-performance perovskite-sensitized solar cells. *Nature* **499,** 316–9 (2013).

21. Smith, I. C., Hoke, E. T., Solis-Ibarra, D., McGehee, M. D. & Karunadasa, H. I. A Layered Hybrid Perovskite Solar-Cell Absorber with Enhanced Moisture Stability. *Angew. Chemie Int. Ed.* **53,** n/a–n/a (2014).

22. Snaith, H. J. *et al.* Anomalous Hysteresis in Perovskite Solar Cells. *J. Phys. Chem. Lett.* **5,** 1511–1515 (2014).

23. Jeon, Y.-J. *et al.* Planar heterojunction perovskite solar cells with superior reproducibility. *Sci. Rep.* **4,** 6953 (2014).

24. Hao, F., Stoumpos, C. C., Cao, D. H., Chang, R. P. H. & Kanatzidis, M. G. Lead-free solid-state organic–inorganic halide perovskite solar cells. *Nat. Photonics* **8,** 489–494 (2014).

25. Tang, C. W. Two-layer organic photovoltaic cell. *Appl. Phys. Lett.* **48,** 183 (1986).

26. Frenkel, J. On the Transformation of light into Heat in Solids. I. *Phys. Rev.* **37,** 17–44 (1931).

27. Knupfer, M. Exciton binding energies in organic semiconductors. *Appl. Phys. A Mater. Sci. Process.* **77,** 623–626 (2003).

28. Stübinger, T. & Brütting, W. Exciton diffusion and optical interference in organic donor–acceptor photovoltaic cells. *J. Appl. Phys.* **90,** 3632 (2001).

29. Van Amerongen, H., van Grodelle, R. & Valkunas, L. Photosynthetic Excitons. *World Sci.* (2000). doi:ISBN: 78-981-4496-85-8

30. Dennler, G., Scharber, M. C. & Brabec, C. J. Polymer-Fullerene Bulk-Heterojunction Solar Cells. *Adv. Mater.* **21,** 1323–1338 (2009).

31. Moliton, A. & Nunzi, J.-M. How to model the behaviour of organic photovoltaic cells. *Polym. Int.* **55,** 583–600 (2006).

32. Matsuo, Y. *et al.* Columnar structure in bulk heterojunction in solution-processable three-layered p-i-n organic photovoltaic devices using tetrabenzoporphyrin precursor and silylmethyl[60]fullerene. *J. Am. Chem. Soc.* **131,** 16048–50 (2009).

33. Lu, L. & Yu, L. Understanding low bandgap polymer PTB7 and optimizing polymer solar cells based on it. *Adv. Mater.* **26,** 4413–30 (2014).

34. He, Z. *et al.* Enhanced power-conversion efficiency in polymer solar cells using an inverted device structure. *Nat. Photonics* **6,** 593–597 (2012).

35. Yu, G., Gao, J., Hummelen, J. C., Wudl, F. & Heeger, A. J. Polymer Photovoltaic Cells: Enhanced Efficiencies via a Network of Internal Donor-Acceptor Heterojunctions. *Science (80-.).* **270,** 1789–1791 (1995).

36. Peet, J. *et al.* Method for increasing the photoconductive response in conjugated polymer/fullerene composites. *Appl. Phys. Lett.* **89,** 252105 (2006).

37. Lee, J. K. *et al.* Processing additives for improved efficiency from bulk heterojunction solar cells. *J. Am. Chem. Soc.* **130,** 3619–23 (2008).

38. Scharber, M., Schultz, N., Sariciftci, N. & Brabec, C. Optical- and photocurrent-detected magnetic resonance studies on conjugated polymer/fullerene composites. *Phys. Rev. B* **67,** 085202 (2003).

39. Hartnett, P. E. *et al.* Slip-stacked perylenediimides as an alternative strategy for high efficiency nonfullerene acceptors in organic photovoltaics. *J. Am. Chem. Soc.* **136,** 16345–56 (2014).

40. Cnops, K. *et al.* 8.4% efficient fullerene-free organic solar cells exploiting long-range exciton energy transfer. *Nat. Commun.* **5,** 3406 (2014).

41. Lenes, M. *et al.* Electron Trapping in Higher Adduct Fullerene-Based Solar Cells. *Adv. Funct. Mater.* **19,** 3002–3007 (2009).

42. Guo, X. *et al.* Polymer solar cells with enhanced fill factors. *Nat. Photonics* **7,** 825–833 (2013).

43. Sims, L. *et al.* Investigation of the s-shape caused by the hole selective layer in bulk heterojunction solar cells. *Org. Electron.* **15,** 2862–2867 (2014).

44. McCulloch, I. *et al.* Polymerisable liquid crystalline organic semiconductors and their fabrication in organic field effect transistors. *J. Mater. Chem.* **13,** 2436 (2003).

45. McCulloch, I. *et al.* Designing solution-processable air-stable liquid crystalline crosslinkable semiconductors. *Philos. Trans. A. Math. Phys. Eng. Sci.* **364,** 2779–87 (2006).

46. Nielsen, C. B., Angerhofer, A., Abboud, K. a & Reynolds, J. R. Discrete photopatternable pi-conjugated oligomers for electrochromic devices. *J. Am. Chem. Soc.* **130,** 9734–46 (2008).

47. Yang, D. *et al.* Novel high-performance photovoltaic D–A conjugated polymers bearing 1,2-squaraine moieties as electron-deficient units. *Sol. Energy Mater. Sol. Cells* **105,** 220–228 (2012).

48. Völker, S. F. *et al.* Polymeric Squaraine Dyes as Electron Donors in Bulk Heterojunction Solar Cells. *Macromol. Chem. Phys.* **211,** 1098–1108 (2010).

49. Brück, S. *et al.* Structure-property relationship of anilino-squaraines in organic solar cells. *Phys. Chem. Chem. Phys.* **16,** 1067–77 (2014).

50. Mayerhöffer, U. *et al.* Outstanding short-circuit currents in BHJ solar cells based on NIR-absorbing acceptor-substituted squaraines. *Angew. Chem. Int. Ed. Engl.* **48,** 8776–9 (2009).

51. Beverina, L. *et al.* Second harmonic generation in nonsymmetrical squaraines : tuning of the directional charge transfer character in highly delocalized dyes †. *J. Mater. Chem.* 8190–8197 (2009). doi:10.1039/b914716k

52. Li, J.-Y., Chen, C.-Y., Ho, W.-C., Chen, S.-H. & Wu, C.-G. Unsymmetrical squaraines incorporating quinoline for near infrared responsive dye-sensitized solar cells. *Org. Lett.* **14,** 5420–3 (2012).

53. Li, J.-Y. *et al.* Unsymmetrical squaraines incorporating the thiophene unit for panchromatic dye-sensitized solar cells. *Org. Lett.* **12,** 5454–7 (2010).

54. Qin, C., Wong, W.-Y. & Han, L. Squaraine dyes for dye-sensitized solar cells: recent advances and future challenges. *Chem. Asian J.* **8,** 1706–19 (2013).

55. Ramaiah, D., Eckert, I., Arun, K. T., Weidenfeller, L. & Epe, B. Squaraine Dyes for Photodynamic Therapy: Mechanism of Cytotoxicity and DNA Damage Induced by Halogenated Squaraine Dyes Plus Light (>600 nm)¶. *Photochem. Photobiol.* **79,** 99–104 (2004).

56. Schmidt, G. M. J. Photodimerization in the solid state. *Pure Appl. Chem.* **27,** 647–678 (1971).

57. Rennert, J., Ruggiero, E. M. & Rapp, J. THE NON-RADIATIVE DISSIPATION OF EXCITATION ENERGY IN SOLID CINNAMIC ACID BY DIMER FORMATION. *Photochem. Photobiol.* **6,** 29–34 (1967).

58. Khan, M., Brunklaus, G., Enkelmann, V. & Spiess, H.-W. Transient states in [2 + 2] photodimerization of cinnamic acid: correlation of solid-state NMR and X-ray analysis. *J. Am. Chem. Soc.* **130,** 1741–8 (2008).

59. Choi, J. J., Yang, X., Norman, Z. M., Billinge, S. J. L. & Owen, J. S. Structure of methylammonium lead iodide within mesoporous titanium dioxide: active material in high-performance perovskite solar cells. *Nano Lett.* **14,** 127–33 (2014).

60. Pettersson, L. A. A., Roman, L. S. & Inganäs, O. Modeling photocurrent action spectra of photovoltaic devices based on organic thin films. *J. Appl. Phys.* **86,** 487 (1999).

61. Bagnis, D. *et al.* Marked alkyl- vs alkenyl-substitutent effects on squaraine dye solid-state structure, carrier mobility, and bulk-heterojunction solar cell efficiency. *J. Am. Chem. Soc.* **132,** 4074–5 (2010).

62. Wei, G. *et al.* Functionalized squaraine donors for nanocrystalline organic photovoltaics. *ACS Nano* **6,** 972–8 (2012).

63. Ronchi, E. *et al.* Regioselective synthesis of 1,2- vs 1,3-squaraines. *Org. Lett.* **13,** 3166–9 (2011).

Chapter III:

Effects of Dipole Moment Inversion in Self-Assembled Nanodielectric for Organic Thin Film Transistors

THEORETICAL INTRODUCTION

Since we have already dealt with the historical and sociological background of transistors, I would like to focus on the theoretical background of transistor operation, starting out with inorganic and then moving on to the organic ones. There are some slight differences in mechanism among the two. A brief run-down on capacitance measurement as carried out in this thesis is presented.

Transistors

As already reported, transistors are one of the most used single pieces of technology we can think of. Their architecture greatly varies, but, whatever iteration of the technology you are analyzing, there are some common elements defining its operation.

Figure 39a shows a sketch of a *bipolar junction transistor* (**BJT**). Bipolar transistors, the direct evolution of a diode, are constituted by three contacts (emitter, collector and base) connected to a three-layered Silicon piece, featuring an alternation of p-n-p or n-p-n doped layers.

The emitter and the collector are contacted on the external layers of the stack (the portion where the emitter is contacted features a higher doping concentration than the other two), while the base is connected to the central portion. As in a normal p-n junction, a depletion zone forms inside the Silicon and, when undisturbed, the charge carriers are in equilibrium with one another. Let us consider npn transistors: once a direct bias is applied from the base to the emitter a current of electrons diffuses through the n-doped material and reaches the base.

By applying a reverse bias to the base-collector junction, electrons are extracted through the collector and the base-emitter current is greatly enhanced. In order to avoid recombination of the minority carriers, the hole-rich p-layer needs a thickness smaller than the diffusion length of the minority carrier.

Two of the main parameters are β, the base-to-collector on base-to-emitter currents ratio, also called amplification factor, and α, the common-base current gain, a parameter which determines the loss of current due to minority carriers recombination through the stack.

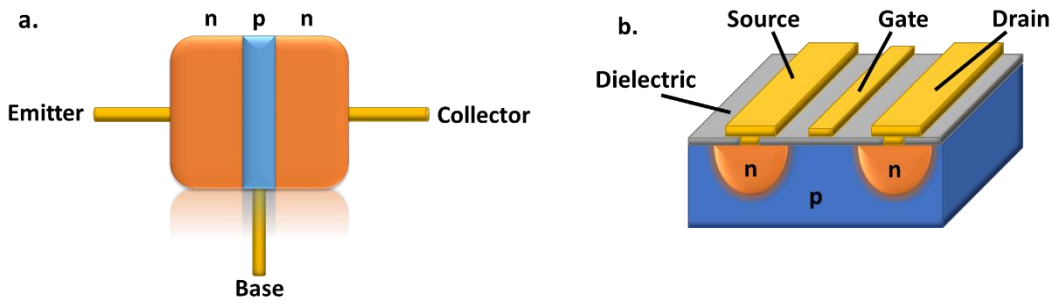

***Figure 39**: schematic architectures of a) a bipolar junction transistor; b) a metal-oxide-semiconductor field effect transistor.*

The cartoon in **Figure 39b**, on the other hand, represents a *field-effect transistor* (**FET**). In particular, it shows a MOSFET, that is a Metal-Oxide-Semiconductor FET, a hint to its top-down structure. These transistors feature three contacts too, but they go with different names: the base is called gate, the emitter is the source and the collector is renamed drain. The principle of operation of FETs is that by

applying a voltage from the gate to the body of the semiconductor (which is short-circuited with the source) the charge carrier distributions inside the semiconductor change, turning the device on or off by favoring or hampering charge conduction through a channel close to the interface. The former type of devices are called enhancement-mode, the latter depletion-mode.

Contrary to BJTs, FETs are unipolar, meaning that in a single device only one type of charge carrier is present, either electrons or holes, whereas BJTs feature both minority and majority carriers in any single device. The unipolarity of FETs allows for more complex architectures which would be unfeasible using BJTs.

MOSFETs feature a fourth element, the *dielectric*, placed between the gate and the doped Silicon. The dielectric, in its most common reiteration, is made of Silicon Oxide, SiO_2, and hinders conduction of carriers though it. The voltage applied across it polarizes the medium, and this polarization modifies the carrier concentration in the immediate vicinity of the dielectric-semiconductor interface.

Figure 39b shows the typical architecture for an n-type enhancement-mode MOSFET. Typical phases of the operation are reported in **Figure 40**.

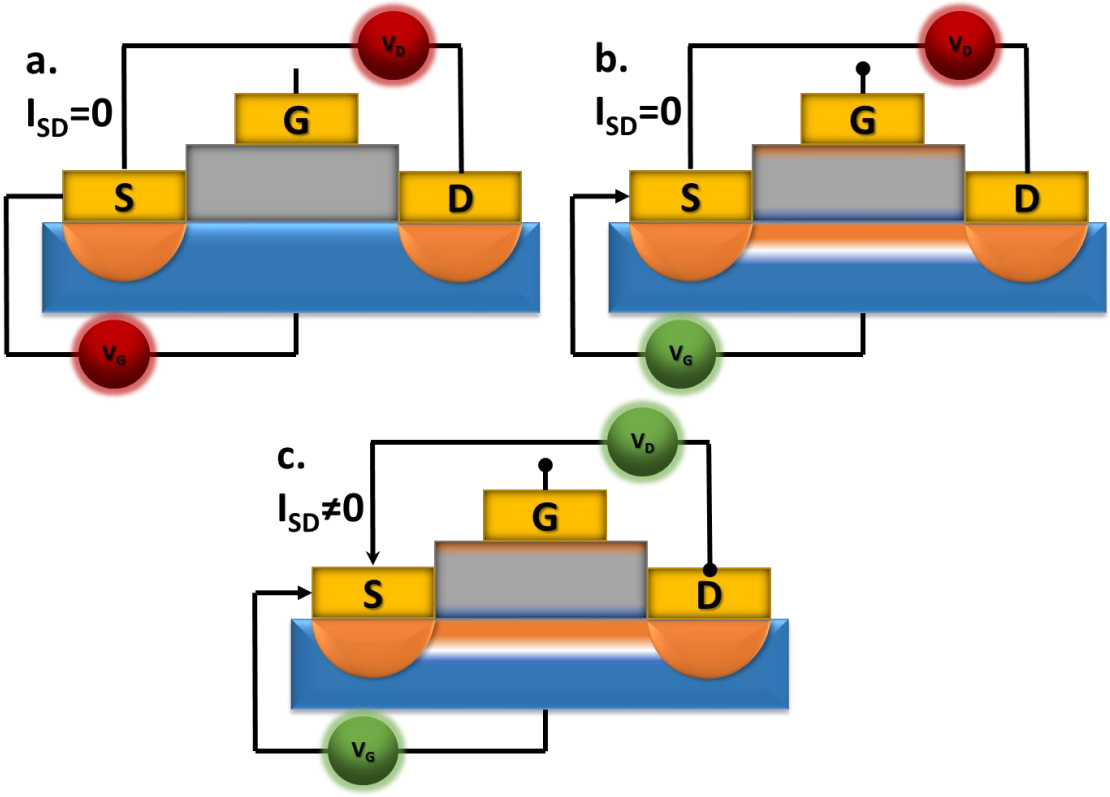

Figure 40: *schematic operation of a MOSFET. a) No voltage applied to the device; b) a direct gate-source bias is applied, the channel is formed; c) a bias is applied from source to drain, and a current flows though the channel near the interface.*

a. No bias is applied to the device. In an enhancement transistor this means that the device is off. The orange and blue portions of the figure represent n- and p-doped Silicon, respectively. The concentrations of mobile (holes) and fixed (lattice) charges are equal, therefore there is no way for the electrons to cross from the source to the drain without recombining in the p-doped layer.

b. By applying a direct bias from the gate to the body (and therefore to the source), the mobile charges in the p-doped Silicon are moved away from the dielectric-semiconductor interface. This causes the formation of a depletion zone close to the interface (the white area), and a "seeping" of electrons from the n-doped areas below the source and the drain. A conduction channel is now present. The device is still not giving any output. The voltage at which the inversion zone starts forming is called the Threshold Voltage (V_T).

c. Upon application of an inverse bias between the source and the drain (V_D; also, the source is set to the ground, therefore at V=0) the electrons are now free to move in the channel and a current flows between the two terminals (I_{SD}).

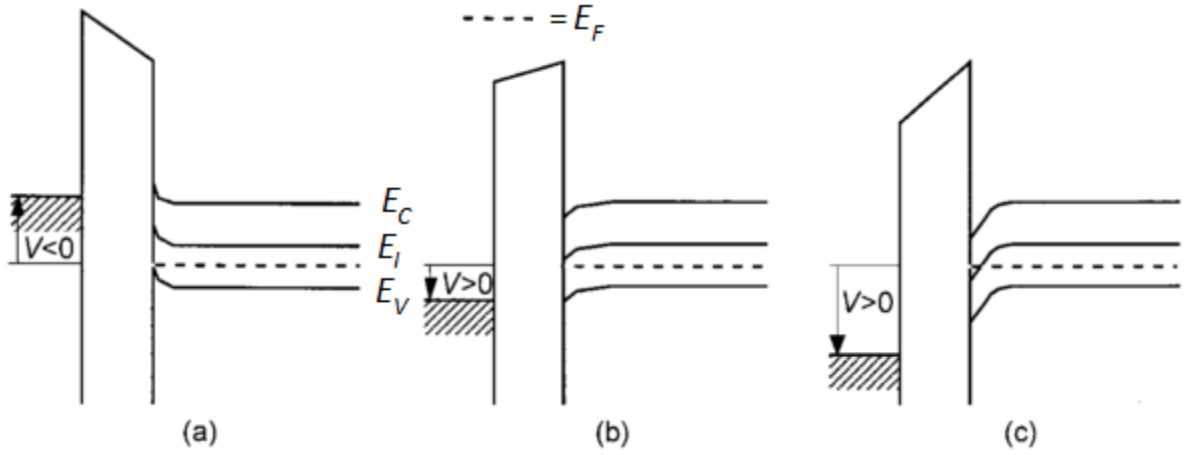

Figure 41: *energetic representation of metal-insulator-semiconductor interface when subjected to: a) a positive bias; b) a mild negative bias; c) a strong negative bias. Adapted from reference*[1]*.*

Figure 41 shows what is happening in the transistor under the energetic point of view. E_C is the energy of the conduction band, E_I is the intrinsic Fermi level, E_V is the energy of the valence band and E_F is the Fermi energy level. Please note that E_F and the ground energy level in the metal are the same.

a. A weak negative bias is applied to the device. The energy levels shift upwards by a quantity $-qV$, q being the elementary charge. The bands in the semiconductor bend upwards, causing an accumulation of positive charge carriers close to the interface.

b. A weak positive bias is applied and the bands shift downwards. This causes a depletion of the majority carriers (in this case holes), which float to higher energies further away from the interface. The depletion area forms.

c. When a stronger positive bias is applied, the additional bending of the bands cause E_I to cross E_F, and minority carriers (electrons) start pooling close to the interface, where the inversion region forms (analogous to **Figure 40b**). The channel is now ready to be exploited through a source-drain voltage, and current can be extracted (as in **Figure 40c**).

This is exactly what happens when capacitance-voltage curves are measured: the polarization of the dielectric is measured by appling a voltage between a metal and a semiconductor and recording the capacitance of the dielectric within (MIS Capacitors). Under the gradual channel assumption (or Shockley hypothesis) which states that the variation of the electric field along the channel is way smaller than the variation of the field as one moves from the dielectric interface into the bulk, or

$$\frac{\partial F_x}{\partial x} \ll \frac{\partial F_y}{\partial y} \qquad [1]$$

, one can derive the dependencies of the source-drain current I_{SD} from the device and operational parameters of the MOSFET (for a full application of this model, see reference[2]), yielding

$$I_{SD} = \frac{W}{L}\mu C_i \left\{ \left(V_G - 2\varphi_B - \frac{V_D}{2} \right) V_D - \frac{2}{3}\frac{\sqrt{2\varepsilon_S q N_A}}{C_i} \left[(V_D + 2\varphi_B)^{3/2} - (2\varphi_B)^{3/2} \right] \right\} \qquad [2]$$

We already know what q, V_G and V_D are, W is the width of the channel, L is the length of the channel, μ is the mobility of the charge carriers, C_i is the capacitance per unit area of the dielectric, ε_S is the electric permittivity of the semiconductor, N_A is the majority carriers concentration and φ_B is the difference between the Fermi energy and intrinsic Fermi energy levels.

This fairly complex equation can be streamlined by dividing the operation of the transistor in two regimes. One of them is identified whenever V_S is small, which affords the equation for I_{SD} in the linear (or triode) regime:

$$I_{SD,lin} = \frac{W}{L}\mu C_i (V_G - V_T) V_D \quad when \quad V_D < (V_G - V_T) \qquad [3]$$

where V_T we already defined as the threshold voltage, i.e. the voltage at which the strong inversion regime is reached. This model hypothesizes a constant doping throughout the channel. The other regime is more relevant at higher V_D, and yields the equation for I_{SD} in the saturation region:

$$I_{SD,sat} = \frac{W}{2L}\mu C_i (V_G - V_T)^2 \quad when \quad V_D > (V_G - V_T) \qquad [4]$$

A typical plot of I_{SD} vs V_G can be found in **Figure 42a**. These are called transfer plots. In **Figure 42b**, instead, you can find a typical output plot, i.e. a scan of I_{SD} as V_D changes (V_G is fixed). Several curves describe the effect of As can be easily noticed, the current increases as the gate voltage increases, and the curve is clearly separated into two different regimes: a linear one and a constant one.

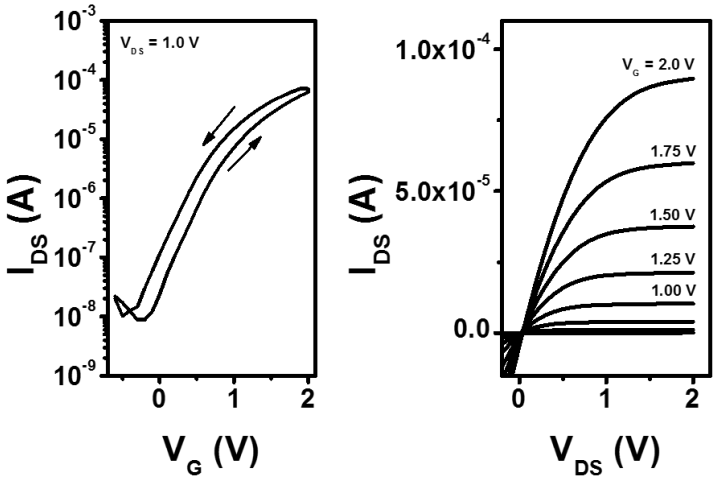

Figure 42: *electrical characteristics of a FET featuring Indium Yttrium Oxide as the semiconductor and Z-SAND (vide infra) as the dielectric. (left) transfer plot at a fixed drain voltage; (right) output plots with varying gate voltages. Reprinted from reference*[3].

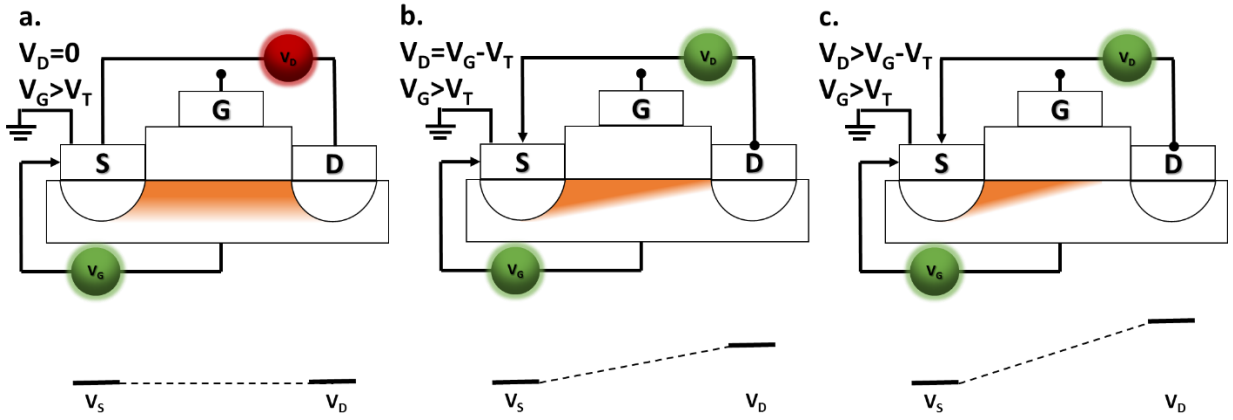

Figure 43: *(above) cartoon representation of the channel spatial distribution inside the semiconductor; (below) potentials of the corresponding electrodes during the drain-source operation.*

The linear behavior can be compared to that of a linear resistor whose resistance is modulated by the gate voltage. The origin of the saturation regime, instead, is a little less straightforward. Let us consider the drop of potential between the drain and the source: when the channel has been formed (i.e. the gate potential is already above the threshold voltage) there is no voltage across the FET and there is no current (**Figure 43a**). Once we crank the drain-source bias up, though, ohmic behavior causes a drop of voltage across the channel. The continual increase of V_D causes an ever-faster depletion of the channel due to an exhaustion of the charge carriers. When V_D=V_G-V_T, the system reaches the pinch-off voltage, meaning that at the physical boundary between the drain and the bulk the width of the channel has reached zero (**Figure 43b**). As the drain voltage keeps on increasing the pinch-off point moves across the channel and widens the depletion zone (**Figure 43c**). This, however, does not cause an interruption in the current due to the high electric field between the pinch-off point and the drain, which manages to keep the current constant as V_D increases.

All devices have to abide by certain figures of merit. In particular, the most common parameters associated with MOSFETs are:

- **μ**, the charge carrier mobility throughout the channel. It's measured in $cm^2\ V^{-1}\ s^{-1}$. The benchmark material is amorphous hydrogenated Silicon (a-Si:H), averaging at 1 $cm^2\ V^{-1}\ s^{-1}$. One can extract two different mobilities from the two different formulas for I_{SD}, the saturation mobility usually being the more significant of the two because most of the MOSFETs are usually used in digital circuitry in the saturation (also called "active") regime.
- **C_i,** the capacitance per area unit of the dielectric, measured in $nF\ cm^{-2}$. This parameter is of the utmost importance to improve performance of the devices, since I_{SD} scales linearly with it. Capacitance is an extensive property of the device, though, and in particular it is bound to the geometry of the metal-insulator-semiconductor system, which can be modelled as a parallel plate capacitor. From capacitor physics we recall that $C_i = \varepsilon_0 \kappa / d$ [5], where ε_0 is the vacuum dielectric constant ($8.85 \times 10^{-12}\ F\ m^{-1}$), κ is the dielectric constant of the medium and d is the thickness of the capacitor. The most commonly used dielectric in MOSFETs is thermally grown SiO_2 (κ=3.9),

but some years ago Intel announced the replacement of SiO_2 with atomic layer deposition-grown hafnium oxide[4] (κ=25).

- **I_{ON}/I_{OFF},** that is the ratio between the current in the saturation region and the drain leak current when the device is off, and it is usually in the range of 10^6. This number is of paramount importance when computing the consumption of the total device. I_{ON} ultimately decides what technology the MOSFETs are applicable to: power-intensive applications, such as OLED TVs, requires higher currents than others, e.g. digital circuitry.
- **V_T,** the threshold voltage. We already discussed this figure of merit and its meaning. It Is worth mentioning that the V_T directly correlates to the device energy consumption and is influenced by the insulator dielectric constant and its thickness.
- **SS,** the subthreshold swing, measured in V decade^{-1}. This parameter measures how fast the device turns on when $V_G \approx V_T$. Standard Si/SiOx MOSFET have a theoretical inferior limit of 60 mV/dec, but are around 70-80 mV/dec on the lab scale.

Organic transistors

The main difference between MOSFET and OFET lies in the semiconducting material. Whereas MOSFETs employ mainly doped Silicon and Germanium, OFETs use organic materials, both polymeric and molecular. There are some major changes when dealing with organic materials:

a. Organic materials are usually non-intentionally chemically doped (with few notable exceptions). The formation of the channel follows the same mechanism than for MOSFETs, with the major difference that these devices work exclusively in an enhancement mode, and not in a depletion one.
b. The successful diffusion of charges inside the channel from the contacts is dependent on the energetics of the materials in the solid state. We can distinguish between n-type materials (conducting electrons) and p-type materials (conducting holes) by analysis of their molecular energy levels. As a rule of thumb, the Highest Occupied Molecular Orbital (HOMO) and the Lowest Unoccupied Molecular Orbital (LUMO) and their energetic alignment with the contacts work function determine whether a material will be n- or p-conducting.
c. The charge transport mechanism across the channel is profoundly different from the inorganic materials case. The latter is mainly based on delocalized excitons (i.e. Wannier-Mott excitons; the delocalization arises mainly from the higher dielectric constants, which shield the carriers from the space charges in the lattice and are therefore loosely bound[5]) and band conduction; it is hindered by the presence of phonons (whose presence is higher as T goes up), which scatter the charge carriers. On the other hand, free charge carriers in organic materials are extremely localized in space in quasi-particles called polarons due to the low dielectric permittivities of the materials. The transport mechanism is phonon-assisted and is therefore favored at higher temperatures. Each charge carrier hops from one energy level to the other (LUMO for electrons, HOMO for holes), or, if the material is crystalline enough, in sub-bands. The defects of the morphology of the material act as charge carrier traps by introducing energy levels in the gap which are filled as carriers travel by. The release mechanism follows an Arrhenius distribution[6], and is therefore more likely when temperature is higher.

How are OFETs faring compared to their inorganic counterparts, under the performance point of view? **Figure 44** summarizes the best mobilities reported until 2010 for OFETs. By looking at this chart we can immediately determine two things:

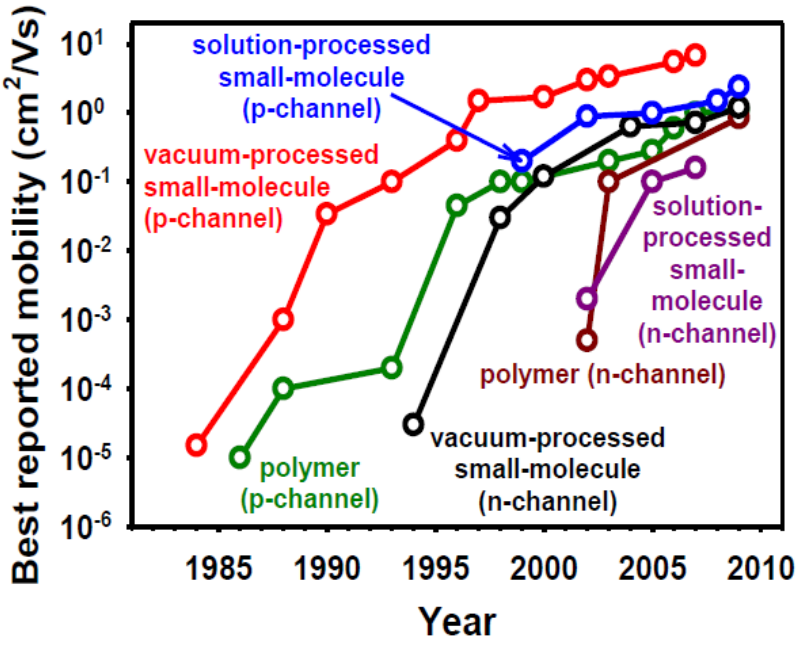

Figure 44: *best reported mobilities in OFETs. Different colors represent different types of fabrication technique or class of organic materials. Reprinted from reference*[7]*.*

1. There is a big difference between the fabrication of devices using solution processes and vacuum processes, which is mainly due to the augmented morphological order in slowly evaporated organic semiconductors. While the latter have been, for a long time, better performing, the former are definitely more viable economically. In the last few years solution processed materials have approached and in some cases surpassed top-notch evaporated semiconductors, which gives hope for large-scale reproducible printable electronics.
2. n-conducting organic materials have gotten late into the scene, and the community is still struggling to find air-stable n-type semiconductors, since only a few are available as of now. This is because the energy level requirements for electron conduction dictate a LUMO level lower than 4.9 eV (with respect to the vacuum level). Were this requirement not to be fulfilled, in fact, the material could be subject to oxygen oxidation and prevent conduction in environmental atmosphere.

As already pointed out, one of the most challenging aspects of this technology arises from the morphological control of the material. Not only the semiconductor has a better conductivity when the domain size increases, but the orientation of the molecules with respect to the flow of charge carriers in the channel is also of the utmost importance. It has in fact been demonstrated that “edge-on” packing with respect to the dielectric-semiconductor interface instead of the “face on” one greatly improves performances and mobilities. This is because when the bias is perpendicular to the orientation of the molecules the carriers have an easier time hopping from one π-cloud to the other.

It is possible to show[8] that by solving Poisson’s equation one can reasonably pin down the extension of the channel inside the bulk. As reported in **Figure 45**, the effect of the gate voltage in the semiconductor extends for 2-3 monolayers, within the 10 nm mark. The penetration depth (also called Debye length) of the voltage depends on both the gate bias and the capacitance of the dielectric.

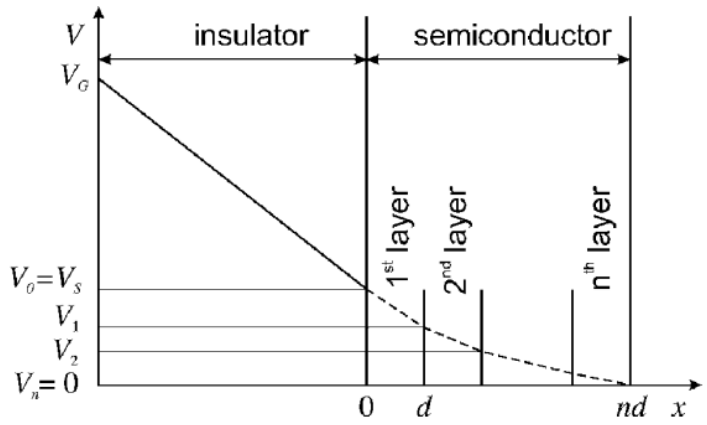

***Figure 45**: effective spatial extension of the potential in the semiconductor. Adapted from reference*[9].

Orientation of molecules on a surface can be tricky. It is regulated largely by non-predictable behaviors and interactions between the molecular nature of the semiconductor and the surface of the underlying dielectric. In order to guide growth of a material onto a surface a huge amount of work has been dedicated to the reliable functionalization of surfaces with self-assembled monolayers (SAMs) which would favor a certain type of growth on another[10], or to prevent the formation of traps on surface defects[11].

***Figure 46**: chemical structures of OTS and HMDS.*

SAMs exploit the reactivity of a certain chemical species towards well specified moieties, and aims at forming dense and well-packed films on a surface. Two of the most common chemicals used to functionalize a silicon surface are octadecyltrichlorosilane[12] (OTS), which leads to an 18-atoms long alkyl functionalization, and hexamethyldisilazane[13] (HMDS), which yields trimethylsilyl moiety cappings. Both of them (**Figure 46**) contain silane groups which are very prone to being hydrolyzed by dangling bonds found on the surface of Silicon Oxide, and therefore tend to create robust, self-limiting and chemically bound monolayers on said surfaces.

The large variety of possible OFET architectures has generated a vast array of SAM functionalizations, but they can probably be channeled into 3 big families:

a. **Silicon-based compounds**: OTS and HMDS belong to this family. These compounds are mainly used to functionalize Silicon Dioxide surfaces due to the spontaneous and irreversible formation of strong Si-O-Si bonds. All of these compounds are easily hydrolyzed when exposed to environmental atmosphere, and therefore the formation of these SAMs has be carried out under strictly controlled conditions.

b. **Sulfur-based compounds**: the exploitation of the (fairly stable) S-Au bond allows for an easy functionalization of gold surfaces, i.e. contacts. This approach has proven extremely useful to reduce electron injection barriers from electrodes to the semiconductor (i.e. contact resistance) in bottom gate bottom contact architectures[14]. This approach has in fact led to more crystalline morphologies due to extended nanodomains and improved connectivity of the islands. Albeit weaker, thiols have been reported to bind to other metallic surface, most notably Silver, Copper, Palladium. In one of such cases the treatment of Silver contacts with pentafluorothiophenol

lowered the work function of the metal by more than 0.6 eV, aligning the energy levels of the electrodes with the HOMO of the OSC and resulting in lower charge traps at the interface, as deduced from subthreshold behavior analysis[15].

c. **Phosphorous-based compounds**: the exploitation of phosphorous compounds in SAMs is probably the most recent among the ones reported. These compounds are usually phosphonic acids, but functionalization of surfaces using phosphonate esters is also not unheard of[16]. The acid character of these molecules make them ideal candidates for basic surfaces functionalization. This comprises a vast majority of metal oxide surfaces[17], ranging from Aluminum Oxide to Zirconium Oxide[18] and Hafnium Oxide[19]. The driving force behind the functionalization is the extremely robust Zr(Hf)-O-P bond, which allows for easy grafting and consistent results.

In the hunt for ever higher mobilities and most promising performances the community has devolved intensive care to the research and application of new dielectrics which could boost performances.

Such materials must exhibit very large capacitance, high breakdown strength, low parasitic current leakage, low trap density, and high thermal stability. Other desirable attributes include amenability to solution or alternative low-cost fabrication methods and compatibility with arbitrary substrates (cloth, plastics, glass, etc.). Generally, Silicon Oxide fails to satisfy many of these requirements and its relatively low dielectric constant compromises optimal device performance.

Some of the new approaches include sodium β-alumina gate dielectrics[20] and solution-processed ion gel materials[21], which have achieved capacitance densities greater than 1 μF cm^{-2}. Such systems, nonetheless, rely on mobile ions for the large capacitance, and this might be frequency and temperature dependent. Furthermore, the materials may not always be solids at room temperature and above. The reports on sodium β-alumina (Na−Al2O3) multilayers also indicate that high-temperature annealing (>700 °C) is required for stable low-leakage performance, implying incompatibility with roll-to-roll processing, organic semiconductors, and low-cost plastic substrates.

Now that we have a more or less clear point of view of the state of the art, it is time to introduce our contribution to the field.

RESULTS AND DISCUSSION

Recently the group by Professor Facchetti and Professor Marks at Northwestern University devised a new strategy for solution-processable high-κ dielectrics. They manufactured hybrid organic-inorganic dielectrics (see **Figure 47a**) with high polarizability by stacking alternating layers of solution-processed zirconia[18] (and later hafnia[22]) and solution-grafted organic molecules (see **Figure 47b**, which we will call **PAE**). The high order, regularity and the low per-layer defectivity of these structures were made possible by the asymmetric affinity of the capping moieties of the organic molecule, i.e. the strong bonding between the phosphonic acid and the zirconia favors a non-centrosymmetric packing and the presence of a net total dipole in the stack.

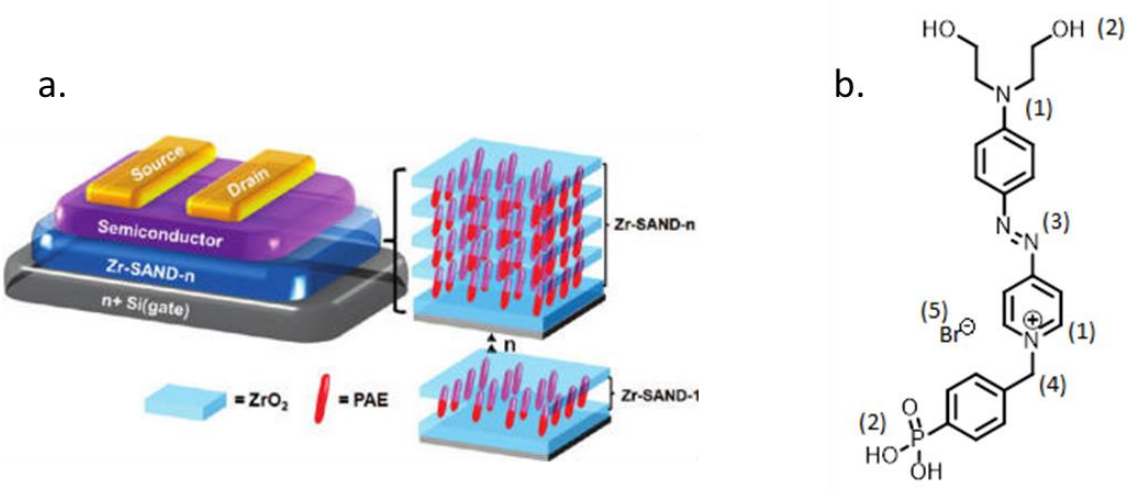

Figure 47: *(a) cartoon representation of a multilayered SAND stack (reprinted from reference[18]); (b) chemical structure of PAE.*

Science is, by definition, a recursive and evolutionary process. As for evolution, a common pool of "genes", or seminal ideas, can be branched out in different directions and yield spectacularly different results. It should not be surprising, then, that this molecular structure was adapted from previous expertise of the authors in the non-linear optics (NLO) field[23]. For this applications, in fact, very high electronic polarizability and definitive non-centrosymmetric packings are required (for a complete introduction to non-linear optics and the marvels of multi-photon absorption see these references[24,25]). Since high polarizability stems from high electronic density and in turn implies a high dielectric constant (which by definition measures the capacity of a molecule or material to respond to an external electromagnetic stimulus), one can begin to see the parallelism between these two apparently different applications. The numbers in **Figure 48** point out some features of this structure which are worth being addressed, and which show a fine example of structure-properties relationship:

1) The presence of both an electron-rich aniline and of an electron-poor pyridinium moieties creates a donor-acceptor structure where a net dipole is formed along the molecular axis, from the aniline towards the pyridine. The dipole effect was not studied in Facchetti's *et al*. original paper and it was mainly a remnant of the already mentioned original application, NLO. In fact in one of the main models for NLO properties of organic molecules, namely the two-states approximation, the difference between the ground state molecular dipole and the charge-transfer state molecular dipole is one of the major contributors to second order hyperpolarizability β;

2) The capping moieties show asymmetric reactivity towards the inorganic priming layer of zirconia. In particular, the Zr-O-P bond is among the strongest bonds reported in literature, allowing for a quick grafting of phosphonic acids (or esters) on the surface. On the other hand, the two alcoholic moieties at the top are not as reactive, and thus favor a non-symmetric packing on the surface, at the same time enabling a multi-layered structures when higher temperatures are involved (i.e. the alcohols can react with a zirconia capping layer if the substrate is heated at a high enough temperature);
3) The diazo bridge between the donor and acceptor parts of the molecule is chemically and thermally more stable than a double or triple bond, less subject to oxidation or electrophilic attacks and inherently more electron-rich (i.e. two electrons per nitrogen atom instead of only one, as with carbon); last but not least, the diazo bridge has a bathochromic effect, allowing for easy UV-Vis monitoring of its grafting kinetics;
4) The unconjugated sp^3 carbon next to the pyridinium core is designed to give flexibility to the molecule once it has been anchored on the zirconia substrate. This allows for maximized coverage and non-centrosymmetric orientation as the dipoles align themselves after electric field-induced orientation;
5) The fact that the molecule itself is a salt provides ample supplies of electronic density to be polarized once an electric field is applied. This contributes to the κ of the layer and in turn enhances the mobility of the final transistor (see the Introduction or any Introduction to Electronics book, such as these:);

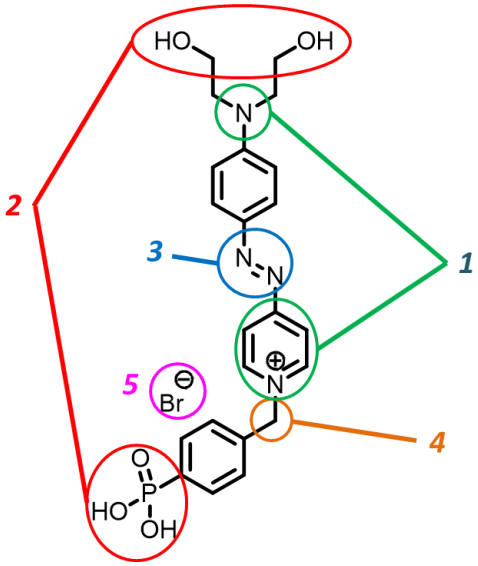

***Figure 48**: schematic representation of the structure-properties relations as highlighted in the main text.*

The dielectrics which were built using this hybrid approach were aptly named **S**elf-**A**ssembled **N**ano**D**ielectrics (**SAND**s) and showed interestingly low leakage currents (10^{-7} A/cm^2), high capacitance (750 nF/cm^2 for a 1-layer SAND), high temperature stability (up to 350° C) and ultrathin thicknesses (12-13 nm). The dielectric showed compatibility with both organic (Pentacene) and inorganic (Zinc Tin Oxide) semiconductors.

In further studies Facchetti *et al.* switched out the zirconia component with solution-processed hafnia, increasing the capacitance to 1100 nF/cm^2 for a single layer capped (i.e. HfOx-PAE-HfOx) dielectric. This

enhancement has been attributed to the higher density of the inorganic layer upon annealing and to the hypotesized higher surface coverage of PAE onto the metal oxide.

Part of this thesis work was dedicated to the exploration of new organic structures to be used in these hybrid multilayered dielectrics. Our interest laid mainly in the effect of the dipole of the organic molecule on the main parameters of a finished OFET device.

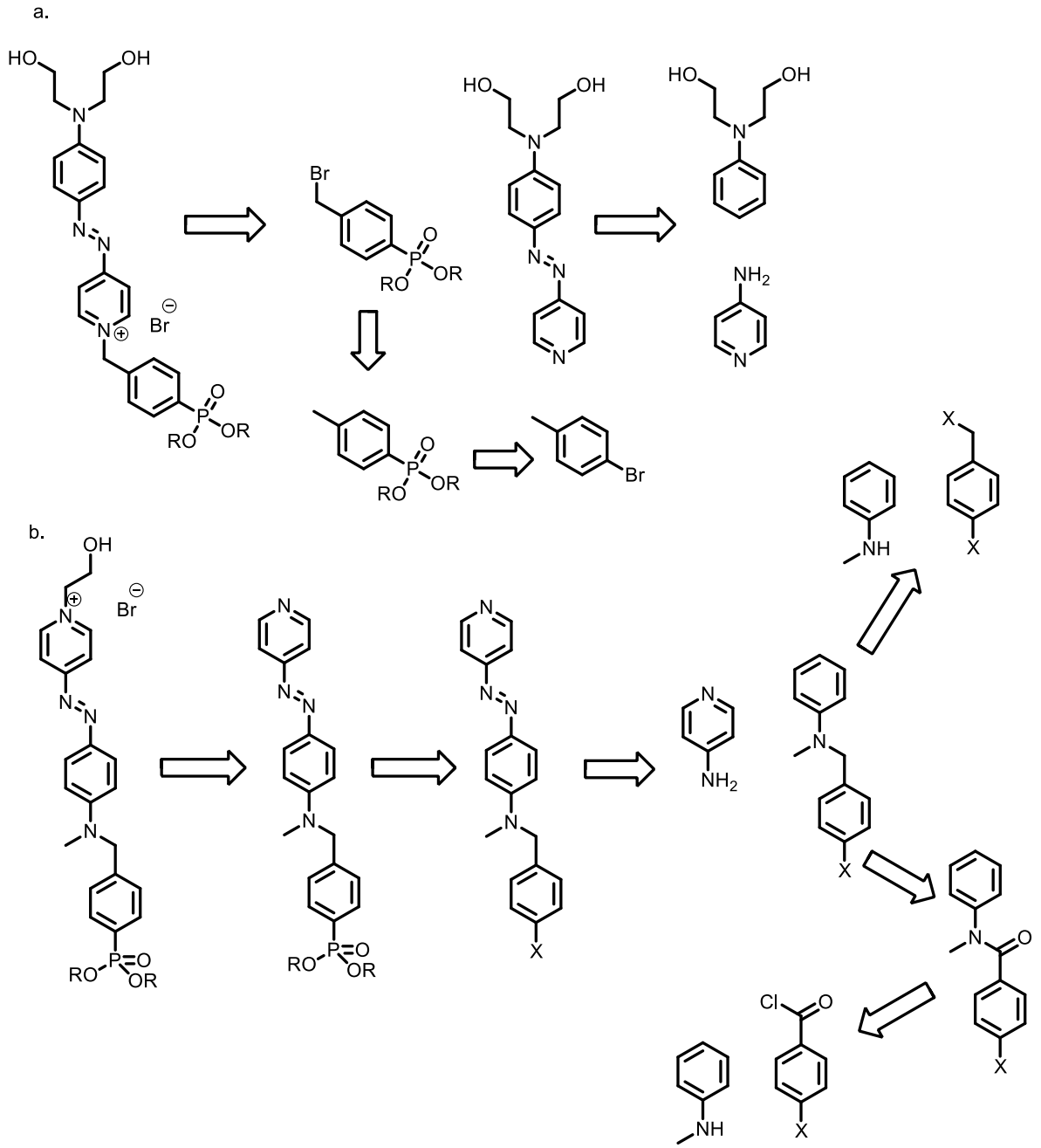

Figure 49: *retrosynthetic approach to: a) PAE; b) IPAE.*

In order to do this we designed a structure having an inverted dipole with respect to PAE (i.e. IPAE, **Figure 49b**). As it can be easily noticed, this is nothing but a “capsized” PAE. It is worth noting, though,

that the structural affinity does not entail a chemical affinity of the intermediates. **Figure 49** shows the retrosynthetic approach for both of the compounds (these schemes do not report the unlocking of the phosphonic esters using trimethylsilyl bromide, *vide infra*, because they are common and trivial).

First thing right off the bat is that the synthesis of PAE is a convergent one, meaning faster and shorter. The simple alkylation step of the already-formed diazo compound allows the introduction of the phosphonic ester derivative using a simple lithiation followed by quenching with diethyl chlorophosphate. During the synthesis of IPAE, though, the necessity to form the aromatic core first and introduce all the subsequent moieties later (due to possible side-reactions or unlocking during the diazotization step) hinders this approach. In order to avoid this, the phosphonate group was planned to be introduced later via homogenous Pd-catalyzed Hirao coupling between a halogen derivative and diethylphosphate.

Synthesis

As per the retrosynthetic scheme, the first step was the formation of the tertiary aromatic amine. This can be done in more than one way, but the pathways we explored mainly referred to amide formation + reduction (Scheme 1a) and to direct formation of the aniline through substitution of an amine on a benzyl position (Scheme 1b). While the former is one step longer and requires more careful chemistry (hydrogenation of amides can be tricky), the *p*-iodobenzoyl chloride precursor was readily available in our laboratory and afforded higher chances of success for subsequent steps (i.e. Hirao coupling). Therefore we proceeded to the formation of the amide under Schotten-Bauman conditions, affording iodo-substituted amide **1** in an 80% yield, and then tried reducing **1** to the tertiary aniline **2**. This reaction proved to be harder than expected, and our endeavors with lithium aluminum hydride or sodium borohydride/triflic anhydride failed miserably. We had to recur to the borane : tetrohydrofuran complex to finally afford the aniline in reproducible and acceptable yields.

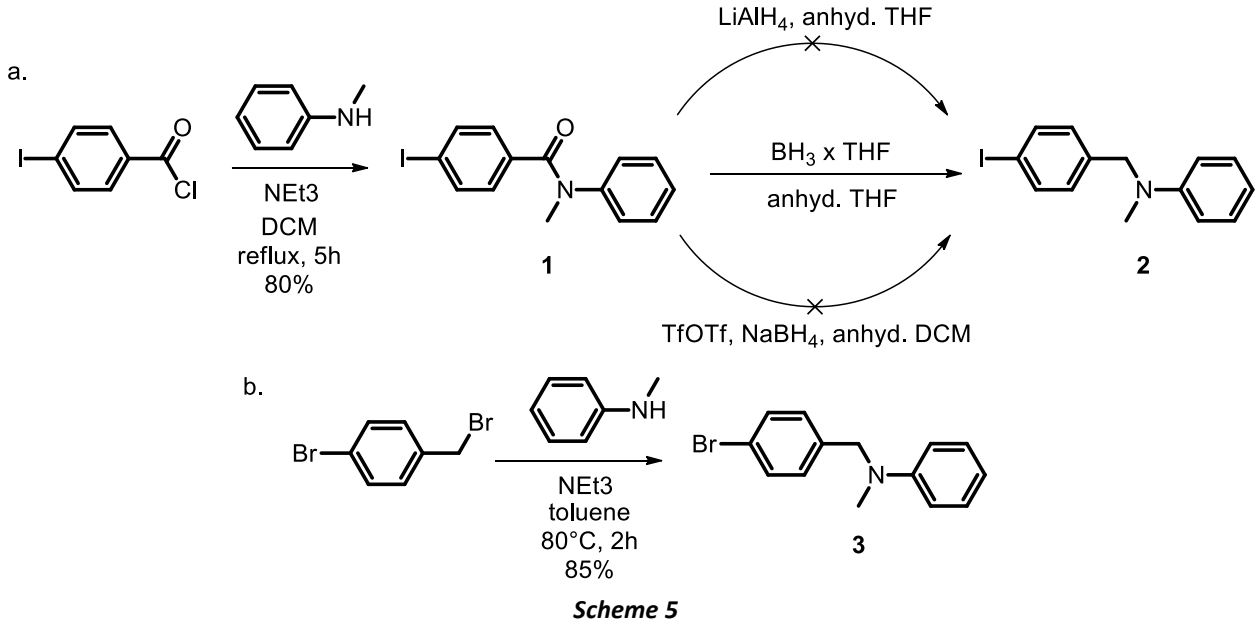

Scheme 5

Nonetheless, aniline **2** turned out to be unstable upon storage under nitrogen in a freezer, evolving elemental iodine. Once the opportunity of having an already installed iodide vanished, we abandoned this

pathway and approached the more facile and immediate benzyl substitution. Aniline **3** was therefore synthesized from the easily available *p*-bromobenzyl bromide and the ubiquitous *N*-methylaniline, once again in Schotten-Bauman conditions. We chose toluene as a solvent for both its high boiling point and the low affinity toward salts. This allowed prompt precipitation of triethylammonium bromide and fast reaction times. Using *N*-methylaniline in slight excess (1.1 equivalents) allows for easy purification via distillation. Compound **3** is a viscous liquid, which turns into a solid once cooled to -10°C. If not cooled it will develop a green hue (maybe a radical cation?) in less than 3 days.

Once we were able to obtain **3** we focused on the diazo coupling. Once subjected to the same conditions used for the synthesis of PAE, though, we noticed **3** did not show the same kind of reactivity. In identical experimental setups 3-aminopyridine showed higher reactivity and afforded the diazo-bridged compound of Scheme 2. Alternatives were tested out (e.g. nitrosonium tetrafluoroborate in acetonitrile/sulfolane, coupling of the nitroso derivative of archetypical substrates with 4-aminopyridine, disodium salt of the nitro group) but yielded no significant results. The at-first surprising lack of information on pyridine-based diazo compounds in literature started to make sense.

Our previous tests with diazonium salts had left us under the impression that the diazonium salt of 4-aminopyridine would hydrolize before it could couple with the nucleophilic site on aniline **3**, which, to add insult to injury, was almost unsoluble in the reaction solvent (i.e. water). The known thermal and chemical instability of diazonium salts was counteracted by reacting 4-aminopyridine with tetrafluoroboric acid before exposition to sodium nitrite. Reports in literature in fact indicate that tetrafluoroborate diazonium salts are more stable to temperature gradients and have a - albeit short - non-null shelf life. Moreover, compound **3** was dissolved into ethanol instead of water, in order to homogenize the reaction mixture and speed up coupling reactions. This afforded the diazocompund **4** in good yields (62%) after a brief silica plug.

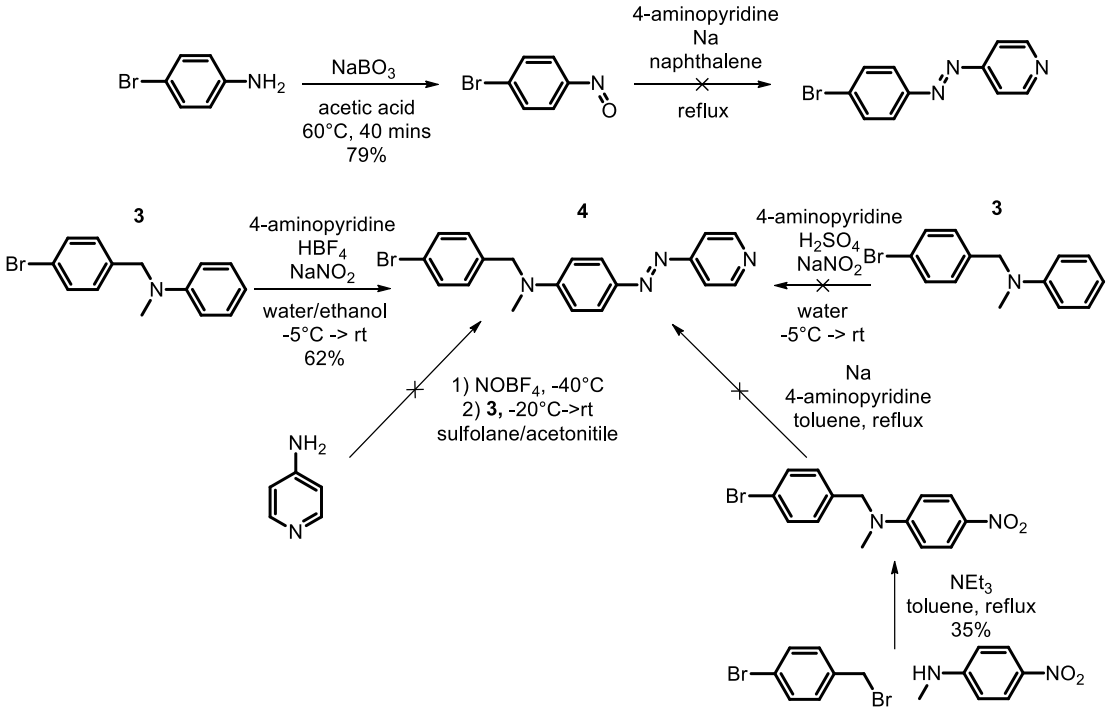

Scheme 6

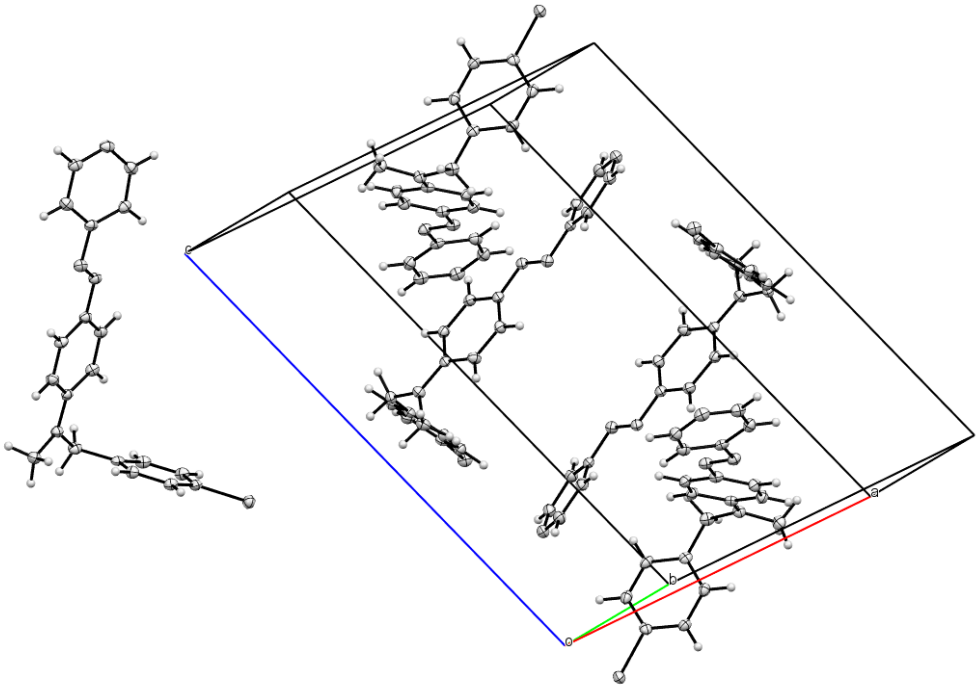

Figure 50: *structure derived from the XRD of 4.*

In order to ascertain the nature of the compound we grew single crystals from slow evaporation of dichloromethane in the form of beautiful 3 to 4 mm-long orange crystalline needles. Both the single molecule and the packing structure of the elemental cell are reported in **Figure 50** (ORTEP format). The space group of the cell is $P12_1/c1$ and features 4 molecules per cell, coupled up in two pairs. The two sets are almost perpendicular one to the other and feature head-to-tail motifs, as expected from the presence of a net dipole along the molecular axis. The non-conjugated portion of the molecule (i.e. the benzyl moiety) forms an angle of 90° with the rigid portion of **4**, and the capping bromides are in close contact with the bromides of adjacent cells. The π-conjugated part unexpectedly shows partial twisting.

Once the protocol for diazotization was optimized we focused on the next step of the synthesis, namely the installation of a phosphonate moiety using Pd-catalyzed Hirao coupling. Several reports in literature hinted at a facile and standardized reactivity, but as you might imagine by now, things didn't really go as planned.

Standard (tetrakis(triphenylphosphine) Palladium (0), triethylamine or Huenig's base, reflux in toluene) or modified (Palladium(II) diacetate, diphenylphosphinoferrocene, potassium acetate and triethylamine, reflux in toluene) Hirao conditions did not yield any conversion to the desired product. We tried resorting to a Nickel(0)-assisted coupling (basically a Michealis-Arbuzov metal-assisted substitution) but we were only able to recover the pure reagent, after either standard heating or microwave irradiation (Scheme 3).

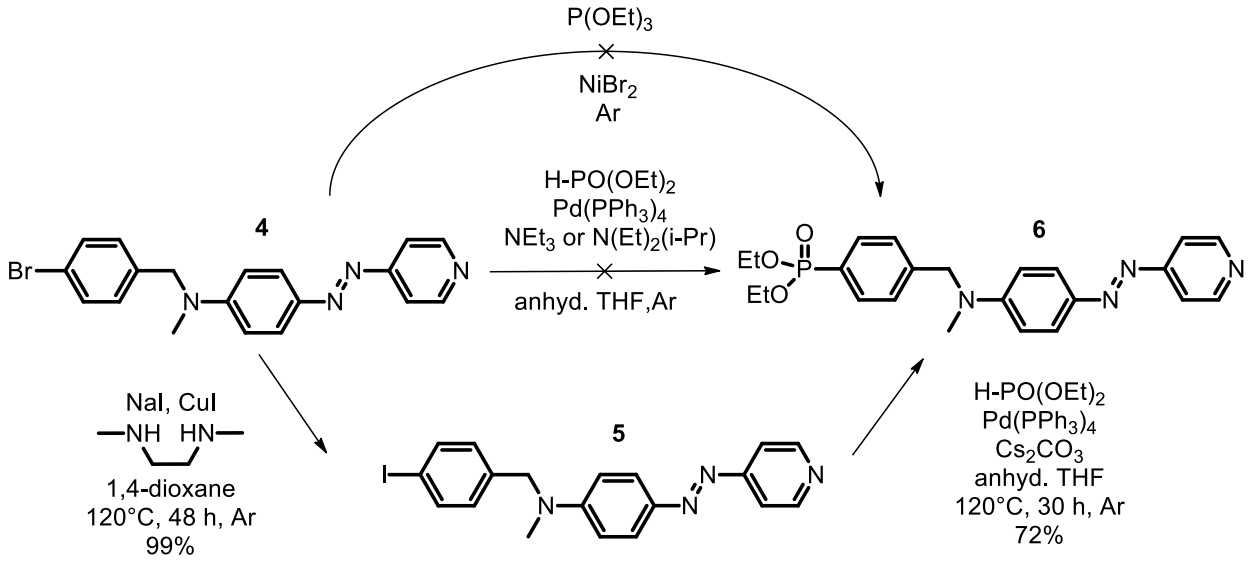

Scheme 7

Dumbstruck by the total lack of reactivity of **4** towards metal(0)-catalyzed coupling (which we tentatively attributed to the presence of an electron-rich *para*-substituent), we resorted to the milder and more classical lithium/halide substitution-nucleophilic attack tandem combo (not reported in Scheme 3). Nonetheless the complexity of the molecule we were working on inhibited selective substitution on the bromide and lithiation occurred preferentially on the 2-position of the pyridine ring.

Eventually we opted for a Finkelstein halide exchange and swapped out the bromide on the benzylic moiety with an iodide. We employed a non-hygroscopic Cu(I) catalyst, copper iodide, and a (more hygroscopic) source of iodide, sodium iodide. The ligand we used to activate the copper complex is DMEDA (dimethylethylenediamine), a pincher ligand which favors the reductive elimination process. This reaction had quantitative yields and easy workup. Once the iodide was in place we were able to substitute it with a phosphonate under Pd(0)-catalyzed Hirao coupling conditions. Our (meager) endeavors to couple the two reactions (Finkelstein + Hirao) in a single pot failed. Nonetheless more accurate screening of the conditions could yield the desired product in one swift maneuver.

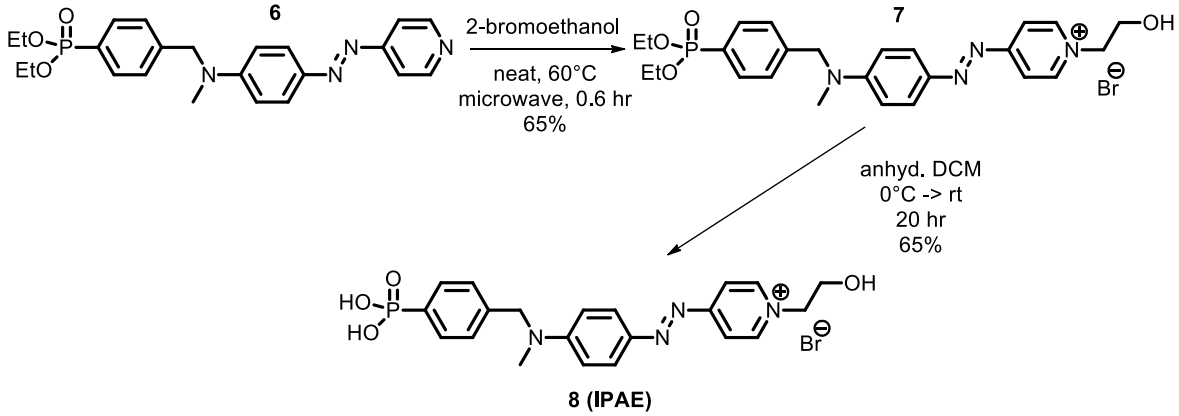

Scheme 8

Table 2: *reaction conditions for the alkylation of* ***6*** *into* ***7****.*

Solvent	Bromoethanol (N)	Reaction time (hr)	Yield (%)
1,4-dioxane	5	72	65
Methanol	5	72	64
Acetone	5	96	66
-	Neat (2 ml)	8	98

What we *did* screen accurately, though, were the conditions for the alkylation of the pyridinic nitrogen. The same reaction was brought out in several polar solvents (1,4-dioxane, acetone, methanol) and in the neat reagent (2-bromoethanol). Not surprisingly, the fastest and highest yielding reaction occurred in the latter conditions, with the solution steering in color from orange to dark purple within seconds (see Table 1). The temperature for the alkylation process resulted being of paramount importance: above 90°C the mixture afforded black tarry byproducts, probably due to the intermolecular condensation of the phosphonates, yielding gummy and insoluble polymers. The crude was worked-up by extracting the product in deionized water and evaporating the residual solvents at 80°C and reduced pressure, affording a very hygroscopic green powder with a golden sheen. The final step of the synthesis was performed by unlocking the diethyl ester of the phosphonic acid using trimethylsilyl bromide in anhydrous DCM at -78°C. The almost complete absence of water, the low temperature and the slow addition of the diluted silyl compound were of the utmost importance. Under any other condition in fact the material degrades.

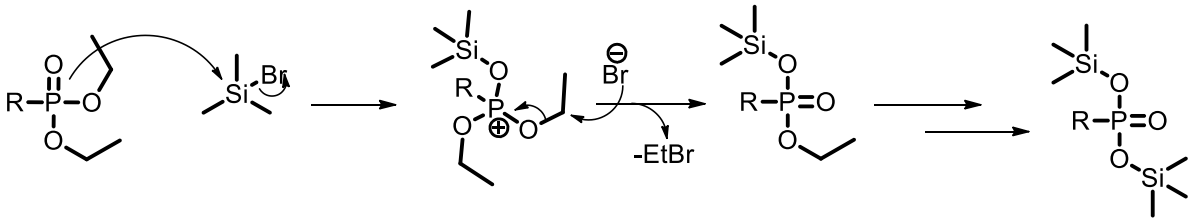

Scheme 9

The reaction mechanism is reported in Scheme 5. It is similar to a Michaelis-Arbuzov reaction, leading to evolution of ethylenebromide. The disubstituted silyl ester is extremely prone to hydrolysis and readily unlocks to phosphonic acid once exposed to either water or methanol. The byproducts are volatile and can be removed at low pressures. Care must be exercised during the workup because the addition of water or wet solvents causes massive evolution of HBr due to the excess of trimethylsilylbromide.

Characterization of IPAE

The final product **8** is less hygroscopic than compound **7**, not turning into a shiny dark green goo minutes after exposition to ambient atmosphere.

Both **PAE** and **IPAE** have interesting halochromic properties, mainly arising from the contemporary presence of an acid (phosphonic acid, pKa_1~1-2) and of a base (azo bridge, pKa~3-4[26]) in the same molecule. This is not so surprising when considering that one of the most common laboratory pH indicators, methyl orange, is an azo dye which is, by definition, halochromic. Its protonated form, heliantin, is commonly used in the dying industry for cotton and wool (**Figure 51**).

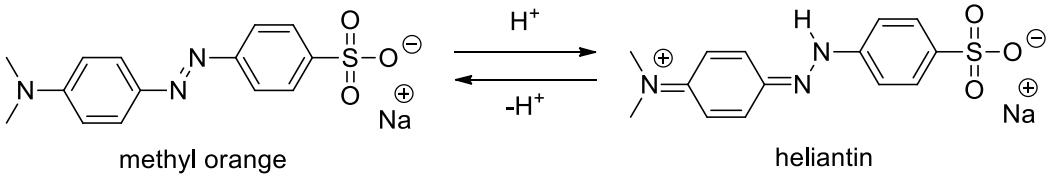

***Figure 51**: chemical structures of methylorange and its protonated form, heliantin.*

Analogously, concentrated (i.e. >0.1M) solutions in polar solvents of PAE or IPAE appear red due to the their self-protonation; upon dilution, though, and consequent pH increase, the absorption spectra steer towards what is reported in **Figure 52**, i.e. the neutral form of the chromophores, which is purple.

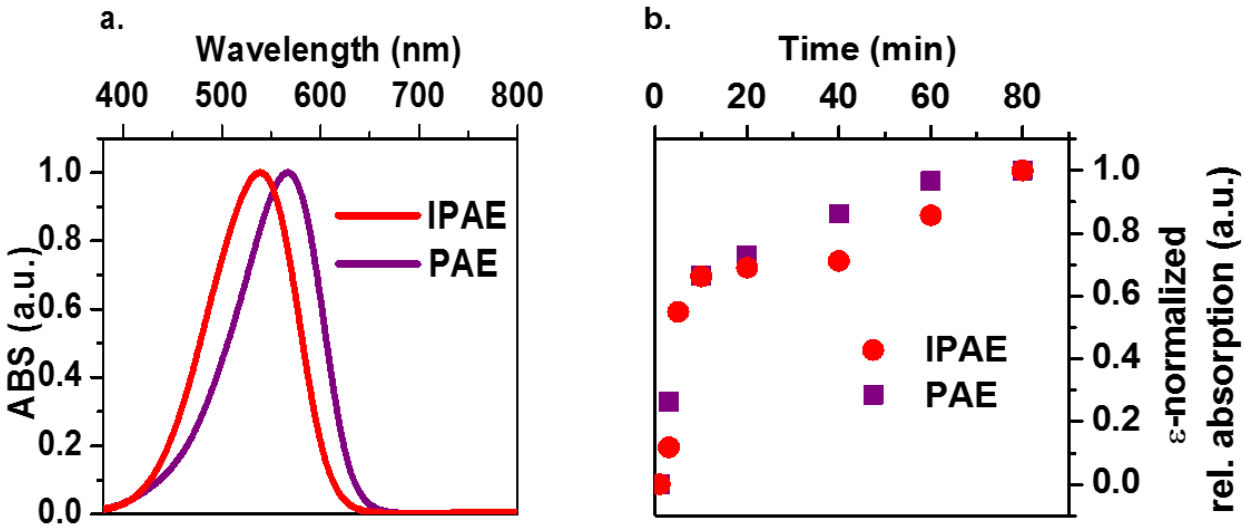

***Figure 52**: (left) UV-Vis absorption spectra of diluted IPAE and PAE solutions in methanol; (right) grafting kinetics on glass/zirconia.*

Noticeably, **IPAE** features an hypsochromic (i.e. blue-) shift of ~30 nm in its absorption. This result is likely due to the different role of the phosphonic acid electron-withdrawing residue in the two compounds. In fact, the $PO(OH)_2$ moiety increases the pull- character of the electron poor pyridinium moiety in **PAE**, thus bolstering the oscillator strength along the molecular axis and red-shifting the absorption. On the other

hand in **IPAE** the electron withdrawing effect decreases the total amount of charge available on the amine push-nitrogen, thus decreasing the total oscillator strength and the donor-acceptor coupling.

This should also motivate the lower molar extinction coefficient ε of IPAE in comparison to PAE, as reported in Table 2.

***Table 3**: optical properties of IPAE and PAE methanol solutions.*

	λ_{MAX} (nm)	ε (L cm^{-1} mol^{-1})
IPAE	538	5.30×10^4
PAE	567	2.59×10^4

Grafting Kinetics

In order to fabricate dielectric stacks one of the most important parameters is the velocity of grafting of the organic molecules onto a surface. Ideally, the surface should reach total coverage by the organic self-assembled monolayer. In practice, this does not happen due to steric hindrance of the molecules (each phosphonic acid head in tridentate bonding occupies 24 $Å^2$, but the molecular footprint ultimately limits the amount of material assembled on the surface).

The driving force for surface assembly is the strong Zr-O-P bond which is formed upon covalent bonding of (I)PAE on the zirconia. The grafting mechanism itself has not been thoroughly studied and can be either acid or base catalyzed.

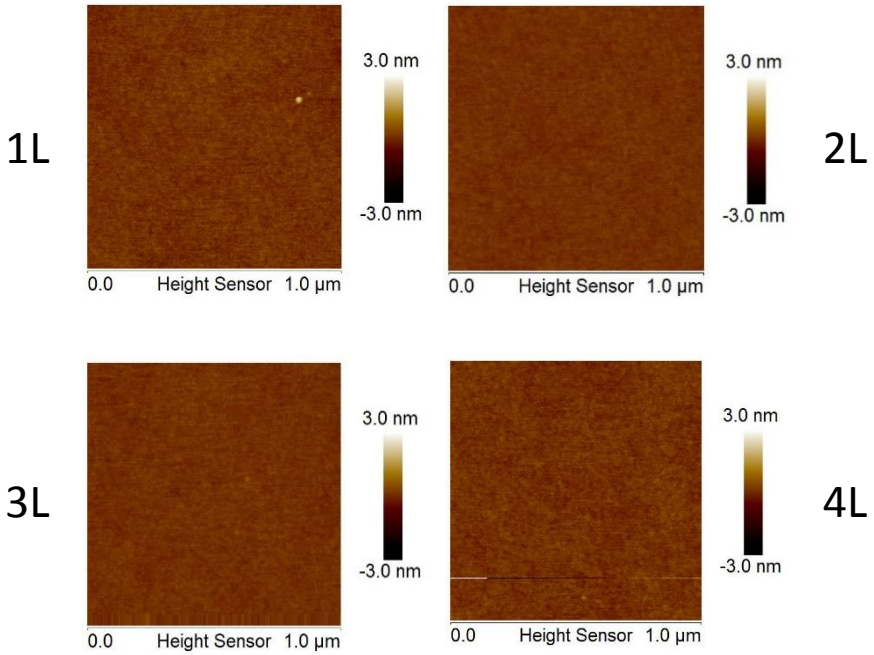

***Figure 53:** AFM height scans of 1-, 2-, 3- and 4-layered IZ-SAND. The exposed surface is made of ultrasmooth Zirconia.*

The zirconia layer is prepared by sol-gel. In particular, $ZrCl_4$ is dissolved in absolute ethanol and mixed with a catalytic amount of aqueous nitric acid. The nitric acid reacts *in situ* with the solvent to form nital, a strong oxidizing species which favors the formation of zirconium oxide in solution. The spin-casting of a dilute solution on a glass or Silicon/Silicon Dioxide substrate and the subsequent mild (150-200°C) thermal treatment allows the formation of a solid smooth and very thin film (under 10 nm, depending on the

concentration of the solution). This promotes anchoring of phosphonic acid-based molecules on the surface. In harsher heating conditions (i.e. 375 – 400°C for less than 5 minutes) the film densifies and shrinks. In order to counteract the high roughness of the glass slides the solution is more concentrated than the one employed for the dielectric fabrication (0.2 M instead of 0.01 M).

After deposition of the ZrOx thin layer on glass slides and subsequent annealing, the different substrates were submerged into a solution of IPAE in methanol at 60°C for different times; their light absorption was subsequently measured via UV-Vis. This allowed for an estimate of the grafting kinetics on the surface by plotting the intensity of the absorption maximum against grafting time. The results are reported in **Figure 52**. It is clear that by the 60 minutes mark the functionalization density of the surface has reached a *plateau*. When compared to the results for PAE, it is interesting to note that both molecules behave almost identically towards the surface, and that apparently their different chemical nature doesn't hamper nor facilitate acid-base interactions on the surface.

Dielectric Fabrication

Once the grafting capabilities of the phosphonic acids were established, we tackled the problem of obtaining a method which would allow for easily reproducible dielectrics. In order to do this n^{++} P-doped silicon wafers were cut in 2.0 cm x 2.5 cm pieces, washed with ethanol in a sonicator at 50°C, Oxygen plasma-treated for 10 minutes and immediately brought into a laminar flow hood. Here a 0.02 M ZrOx precursor solution was spuncast at 5000 rpm for 30 seconds, annealed at 200°C for 20 minutes to densify the priming layer, and dipped into warm methanol (60°C) for 40-50 minutes. Once the grafting is done the organic layer is capped using a diluted solution of the precursor and annealed once again.

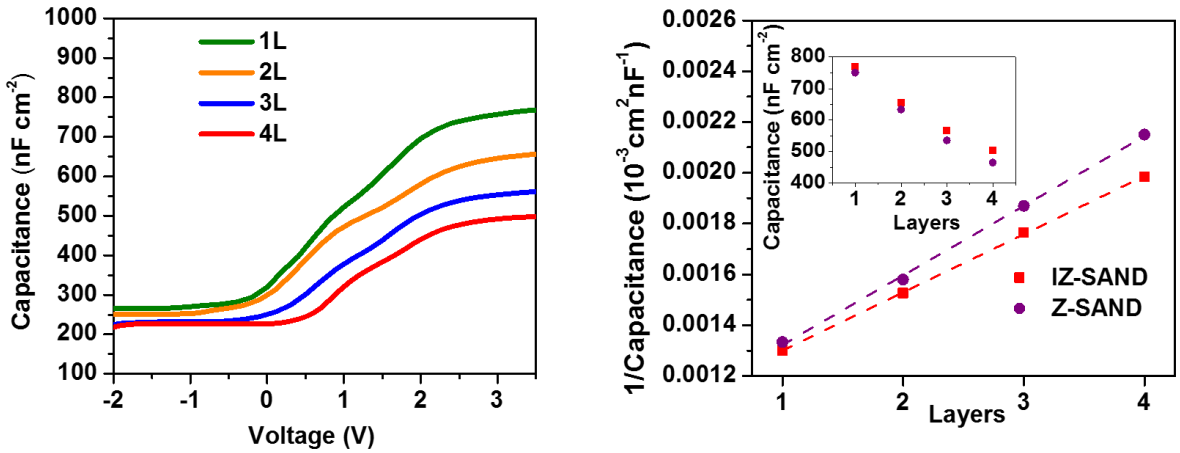

Figure 54: *(left) C-V curves of 1 to 4 layers of IZ-SAND; (right) linear dependency of 1/C from the number of layers; inset: the value of C with varying layers.*

The same procedure can be easily scaled to the desired number of layers in the dielectric, obviously affecting the final number of layers, its thickness and its overall capacitance (see Eq. 5). AFM images of the zirconium capping layers are reported in **Figure 53** for varying number of layers. The surfaces are very smooth, as demonstrated by their low (<1 nm) height rms, and appear to be pin-hole and defect free. This is extremely important for thin dielectric surfaces because inhomogeneity in the film can cause short

circuit due to diffusion of the capping metal to the gate and increase the current leak during operation of the finished device.

In order to test the capacitance of the dielectric, metal-insulator-semiconductor (MIS) capacitors were built. A brief run-down of the theory behind these measurements can be found in the Introduction to this chapter (*vide supra*).

The Capacitance-Voltage curves reported in **Figure 54** show a decrease in the capacitance @ 3 V as the number of layer increases. This is true for both IPAE- and PAE-based dielectrics (i.e. **IZ-SAND** and **Z-SAND**, respectively) and is to be expected due to the increasing thickness of the final dielectric (see again Eq. 5).

By modeling the dielectric as a series of capacitors,

$$\frac{1}{C_{TOT}} = \sum_n \frac{1}{C_n} = \frac{1}{C_{SiO2}} + \frac{1}{C_{Zpr}} + n\left(\frac{1}{C_{ZOx}} + \frac{1}{C_{Org}}\right) \qquad [6]$$

Where C_{SiO2}, C_{ZPR}, C_{ZOX} and C_{ORG} are the capacitances of the native Silicon Dioxide layer, of the priming zirconia layer, the subsequent additional zirconia layers and of the organic molecule layers, respectively. The results can then be fitted to a linear regression; this yields some useful insights into the structure of the dielectric, hinting at a reproducible multilayered structure. The difference in the capacitance values can be attributed to the different κ of the organic molecules (always see Eq. 5) or to the thickness of the materials.

Table 4: *electrical characteristic of MIS built on Gold/(I)Z-SAND/Silicon*

	Capacitance (nF cm^{-2})				K_{ORG}
	1 Layer	**2 Layers**	**3 Layers**	**4 Layers**	
IPAE/IZ-SAND	770	655	566	503	13
PAE/Z-SAND	750	633	535	465	9

Li Zeng (part of Professor Bedzyk's group at Northwestern University, IL) helped us discern among the two possibilities by using X-Ray Reflectivity (XRR) techniques and modeling. This mixed experimental and modeling-reliant technique in fact allows to characterize a thin film by measuring the reflectivity of an X-ray monochromatic beam upon impingement on the surface and by evaluating its interference fringes as the radiation bounces back from the material, interacting with itself.

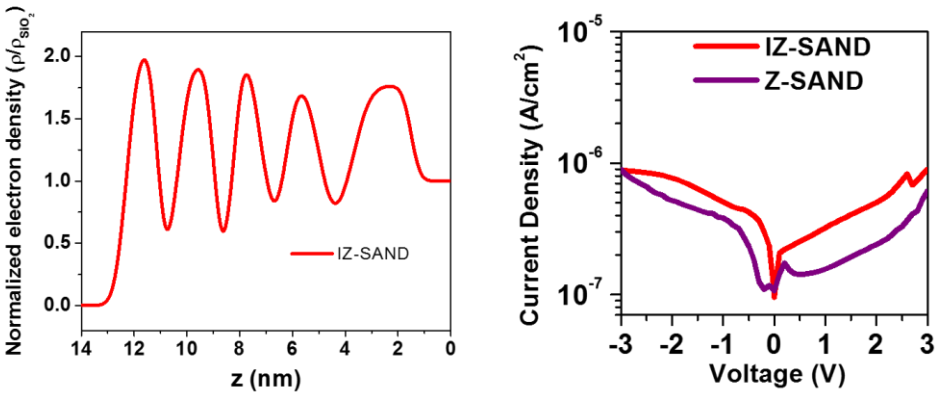

Figure 55*: (left) XRR scan of a 4-layered IZ-SAND dielectric, plotting the electron density distribution throughout the layers; (right) leakage current throughout the stack.*

One of the information which can be extracted from such measurements is the electronic density of the layer, as reported in **Figure 55**. By considering the second derivative of this plot one can determine with Ångstrom resolution the position of the interface between organic (low electronic density) and inorganic (high electronic density) portions of the multistack.

This helped us in determining that the thicknesses of the layers for both PAE and IPAE are very similar (1.2 nm, with a 10% inaccuracy). This implies that the only contribution to the different overall capacitance of the materials arises from their different κ. In particular, plotting Eq 5 into Eq 6 allows us to calculate κ as 9 and 13 for PAE and IPAE monolayers, respectively.

Interestingly enough, the C-V curves do not shift with the change of the dipole in the organic structure. In fact previous literature reported different behavior for self-assembled monolayers on the surface of Silicon or Aluminum Oxide. In our opinion, the absence of a shift when switching from PAE to IPAE is consistent with the lack of a shift when the number of layers in the stack change. If the dipoles were relevant for C-V curves we would see a progressive shift going from 1-layer to 4-layers multistacks. We are currently looking into this peculiar behavior.

We tested the insulating of a 4-layered stack by measuring their leakage currents (namely, the amount of current flowing through the dielectric once a voltage is applied across it). The dielectrics show currents below 10^{-6} A/cm^2 in the ±3V range. This indicates a good spatial uniformity of the dielectric and the absence of pinholes or percolation pathways which would favor short-circuiting across the dielectric. Also, the lack of an evident breakdown of the dielectrics indicates that the material is able to withstand electric fields up to 2.3 MV/cm.

Organic Field Effect Transistors

The thus-fabricated 4-layered dielectrics were subsequently employed in the fabrication of top-contact bottom-gate organic field effect transistors. Archetypical representative semiconductors (pentacene, **P5** for p-type materials and hexadecafluoro copper phthalocyanine, **F16CuPc** for n-type materials, as seen in Fig X) were purified by zone sublimation twice and evaporated onto the dielectrics. In order to decrease the possible total amount of defects in the semiconducting layer, the organic materials were evaporated in 5 mm x 8 mm rectangles using Al foil masks.

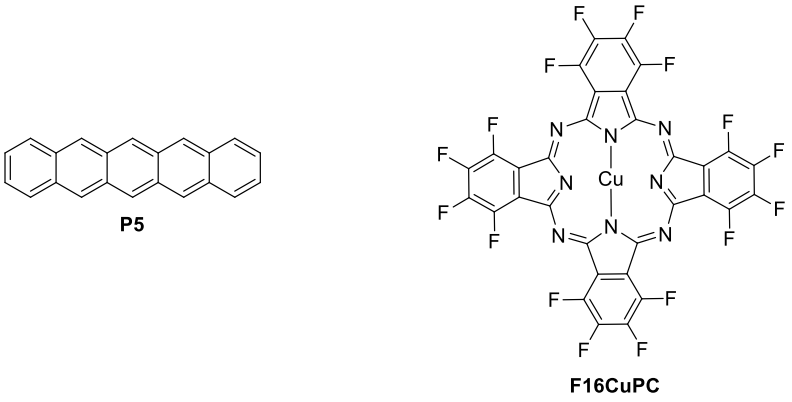

***Figure 56**: chemical structures of pentacene (left) and hexadecafluoro copper phthalocyanine (right).*

As already pointed out in the Introduction (*vide supra*), the charge accumulation layer extends into the organic semiconductor for the first few "monolayers" of the material. In order to maximize the performances of the materials, hence, it is of the utmost importance to obtain crystal grains of adequate size. In order to do this the evaporation rate has to be as low as possible, within the detection limits of the quartz crystal balance (0.1 Å/s).

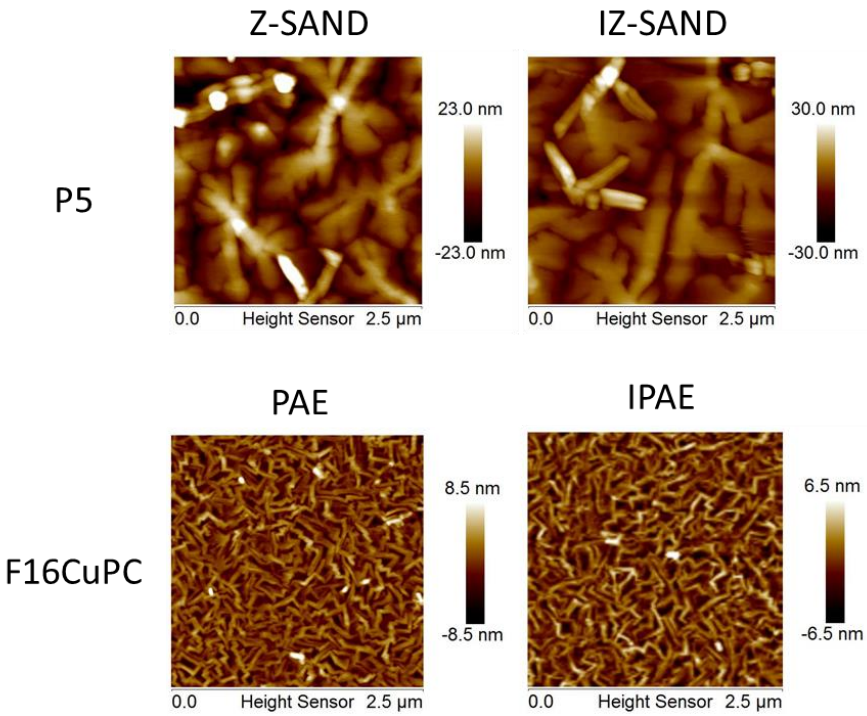

***Figure 57**: AFM height scans of (above) P5 and (below) F16CuPC on (left) Z-SAND and (right) IZ-SAND.*

The cohesion and morphology of the evaporated materials were verified by AFM. P5 shows large dendrimeric domains several hundred nanometers in size, which is what is usually expected from optimum grade semiconducting pentacene. The phthalocyanine F16CuPC also shows wire-like domains oriented parallel to the surface. Most noticeably, the morphology of both semiconductors is almost identical on both Z-SAND and IZ-SAND. These films were contacted by evaporating Gold through a mask (W = 5 mm, L = 100 µm; note that W>>L in order to decrease the distortion of the electric field at the borders of the device).

The results are now summarized by showing the transfer plots for the resulting OFETs. The dielectrics only differ for the organic molecule included in the multistack (**IPAE** for **IZ-SAND** vs **PAE** for **Z-SAND**, as reported in **Figure 58**). Each set of data is 20+ samples strong, allowing for meaningful comparisons between data distributions, which are also corroborated by box-and-whiskers (bnw) plots when relevant. Most important figure of merits for these datasets are reported in Table 4.

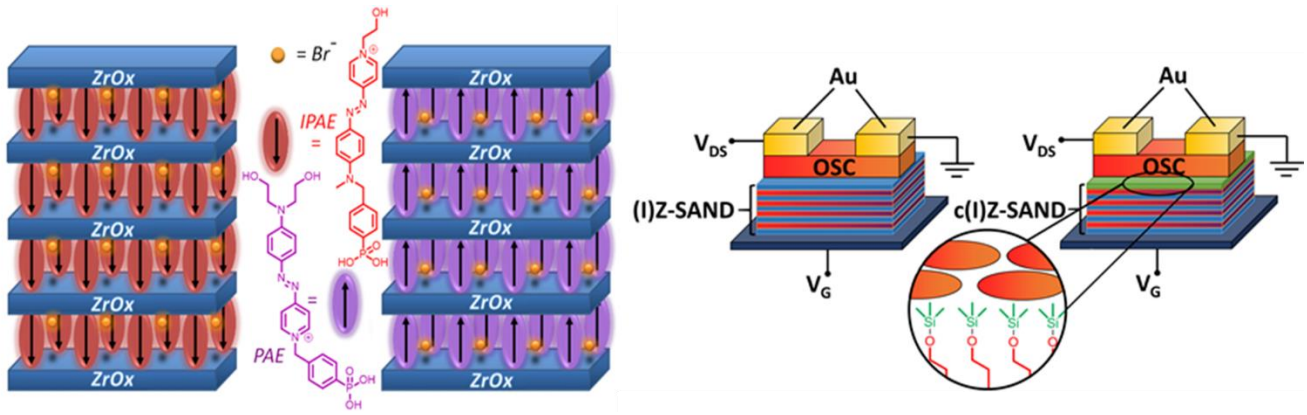

***Figure 58**: (left) cartoon representation of the final four-layered dielectric; (right) cartoon representation of the final OFET architecture.*

We first analyzed the set employing P5 as a semiconductor. The quality of the OFET is high, showing a decent on-off ratio (see Table X), high mobility and very low subthreshold swing. Most noticeably, the threshold voltage for both Z-SAND and IZ-SAND is in the range of -1V, i.e. there is no dipole effect stemming from the threshold voltage, only reporting a small – albeit consistent – negative of ΔV_{TH} = 50 mV shift going from Z-SAND to IZ-SAND. If instead of using the threshold voltage we refer to the turn-on voltage (*vide supra*) the shift ΔV_{ON} is -150 mV. Literature points out that the direction of the shift is consistent with a dipole inversion of the dielectric stack, but the effect is smaller than expected.

***Table 5:** summary of the electrical characterization of OFETs built on 4-layers (I)Z-SAND. a. HMDS-capped four-layers Z-SAND; b. HMDS-capped four-layers IZ-SAND; c. Values represent the average of 20+ devices and are reported with their relative errors; the values between parenthesis are the maximum values; d. these values are non-significant due to a very low ION/IOFF ratio.*

	P5			
	Z-SAND	**IZ-SAND**	**cZ-SAND[a]**	**cIZ-SAND[b]**
μ^c ($cm^2 V^{-1} s^{-1}$)	0.44±0.04 (0.58)	0.55±0.05 (0.69)	0.032±0.004 (0.05)	0.17±0.01 (0.20)
I_{ON}/I_{OFF}	10^5	10^5	10^3	10^4
V_{TH} (V)	-0.95±.0.01	-1.00±0.01	-1.40±0.03	-1.65±0.03
V_{ON} (V)	0±0.01	-0.15±0.02	0.65±0.05	-0.65±0.04
SS (V/dec)	-0.18±0.01	-0.18±0.02	-0.40±0.05	-0.20±0.02
	F16CuPC			
μ^c ($cm^2 V^{-1} s^{-1}$)	0.051±0.003 (0.066)	0.055±0.002 (0.070)	0.0013±0.0001 (0.0018)	0.0010±0.0001 (0.011)
I_{ON}/I_{OFF}	10^2	10^2	10	~10
V_{TH} (V)	-0.25±0.08	-0.55±0.07	[d]	[d]
V_{ON} (V)	-0.8±0.01	-1.3±0.02	[d]	[d]
SS (V/dec)	1.26±0.04	1.20±0.03	-[d]	-[d]

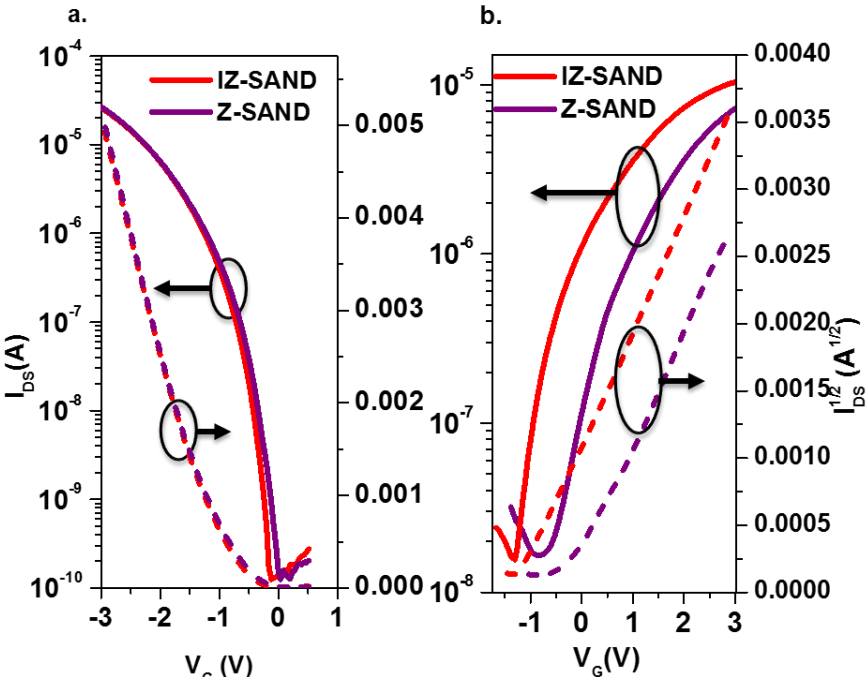

***Figure 59**: transfer plots of OFETs built on 4-layers (I)Z-SAND based on (a). P5 and (b). F16CuPC as semiconductors.*

Interestingly enough, when we switch from a p-conductor as P5 to an n-conductor as F16CuPC, the shift varies greatly. In fact ΔV_{TH} is 300 mV, and the ΔV_{ON} goes up to 500 mV. We infer that the different behaviour might arise from the nature of the charge carriers involved in the process. Let us begin by considering the p-channel OFETs.

We can hypothesize that the presumably mobile negative charge in the dielectric (that is, the bromide ion) can migrate to the (I)PAE-ZrOx interface, creating bound states which partially stabilize the polarization of the stack. In turn, this added negative charge can create more electrons in the organic semiconductor more easily. Since both PAE and IPAE have mobile negative charges, the effect of the dipole seems to be shielded by this interfacial "exciton".

On the other hand, in n-channel OFETs the positive charge is fixed, since it is covalently bound to the matrix. Migration of the charge along the conjugated molecular axis could be possible (given the zwitterionic nature of the framework) but less likely due to a lack of stabilization. Plus, the alkyl moieties capping (I)PAE would prevent the spatial vicinity needed to create the intimate vicinity of the charges.

In order to verify if this dampened effect was due to the final zirconia capping layer, we fabricated devices by avoiding the spinning of the top zirconium oxide layer and by functionalizing the exposed hydroxyl moieties from the organic layer with hexamethyldisilazane (HMDS), affording trimethylsilyl (i.e. TMS)-capped surfaces. The device performances show that by replacing the ~1 nm ZrOx with TMS the threshold voltage shift becomes stronger, albeit this also causes a modest FET performance deterioration and the arise of an asymmetry in key parameters in a cZ- vs cIZ-SAND comparison. For P5 OFETs, for instance, the removal of the capping zirconia layer causes a threshold voltage shift of ~300 mV, from -0.25 to -0.55 V.

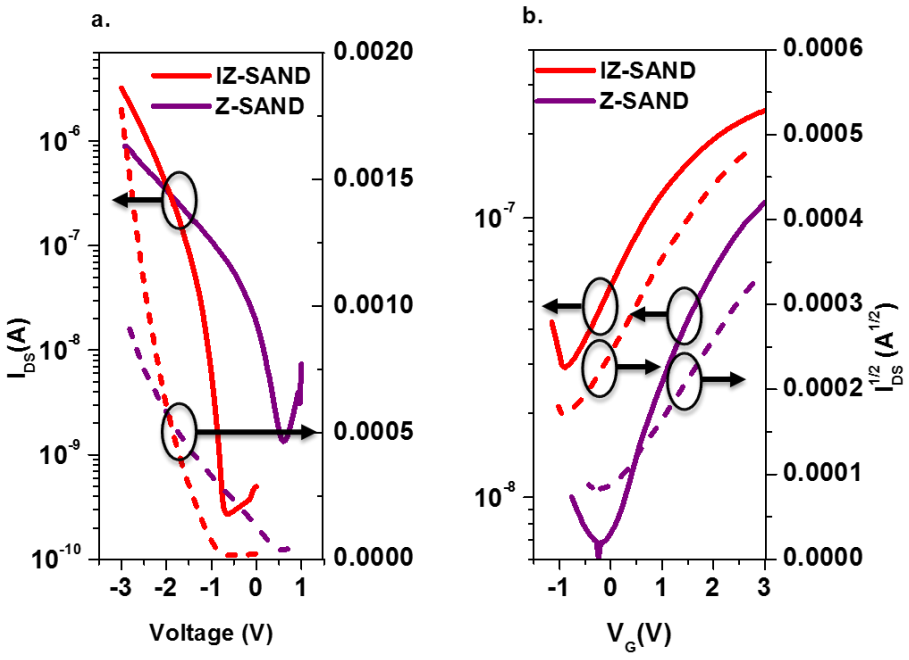

***Figure 60**: transfer plots of OFETs built on 4-layers (I)Z-SAND based on (a). P5 and (b). F16CuPC as semiconductors*

If, instead, we use the turn-on voltage V_{ON} as a figure of merit, the shift between the two stacks polarities amounts to 1.3V. It is worth noting that cIZ-SAND devices maintain most of their characteristics intact, allowing to move V_{ON} to almost halfway of the operating range of the transistor. This, together with a fast turn-on (i.e. low subthreshold swing), are essential requirement for digital switches, where the difference between the "0" and "1" states must be abrupt and shielded from noise levels (i.e. far from 0V).

The direction of these shifts is in accordance with literature reports regarding SAM dipole inversion, hinting that IPAE could feature an inversed dipole with respect to PAE. The F16CuPC OFETs on HMDS-

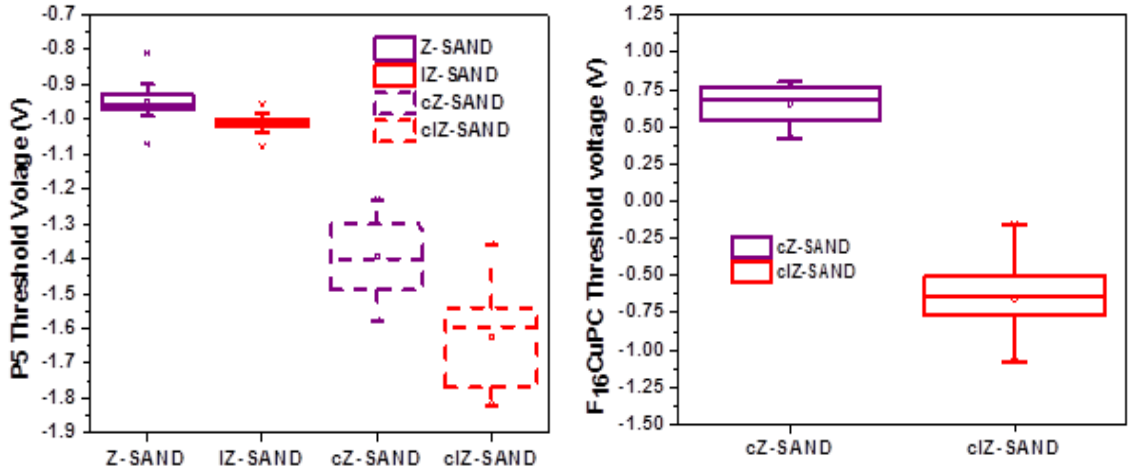

***Figure 61:** box-and-whiskers plots showing the effective difference of threshold voltage in the analyzed datasets.*

capped dielectrics, on the other hand, show below-average performances. AFM phase images of the material show sub-50 nm crystallites with abundant grain border surface, and a complete loss of cohesion in the semiconducting layer. We infer that the different surface energies of the substrates and the proximity of the molecular dipole to the interface might be the reason for the inconvenient morphology of the semiconductor.

Using the difference ΔV in turn-on voltage between the c(I)Z-SAND and the regular (I)Z-SAND stacks (which

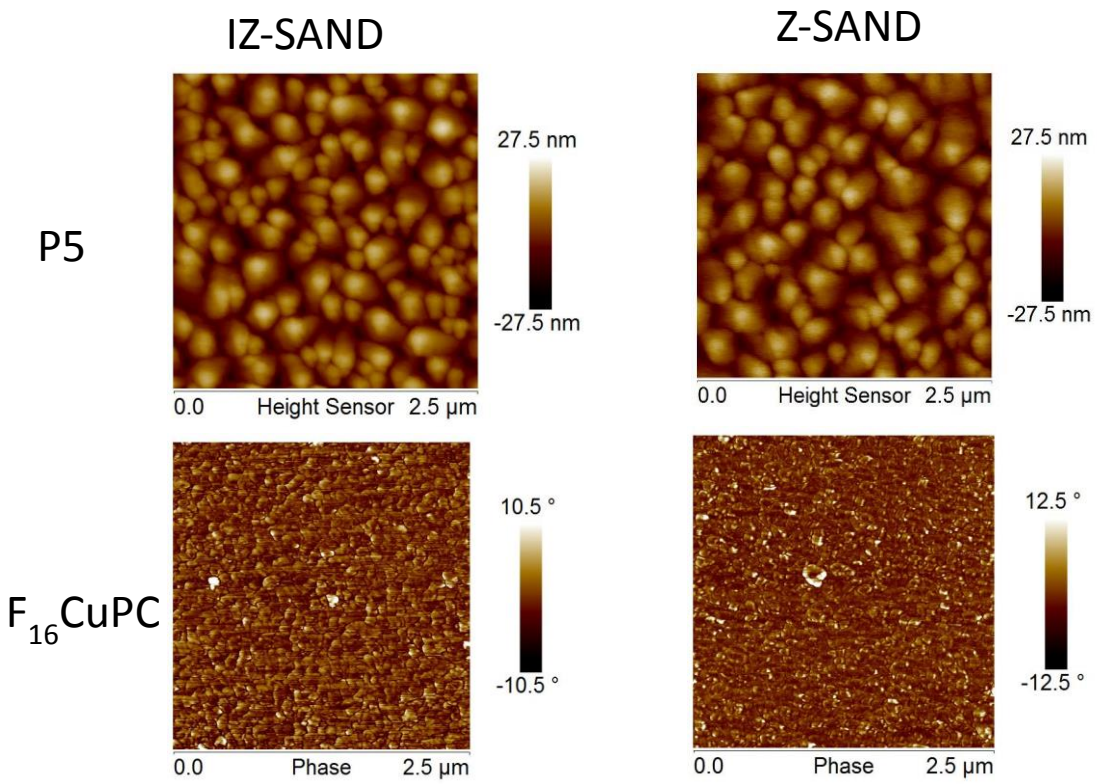

***Figure 62**: (above) AFM height scans of P5 and (below) AFM phase scans of F16CuPC on (left) IZ-SAND and (right) Z-SAND.*

showed limited V_{ON} shifts) for P5 based devices, it could be possible to evaluate the direction of the dipole through the equations $\Delta V = N\mu/\varepsilon_0\kappa$, where N is the surface density of the (I)PAE SAMs (2.5×10^{14} cm^{-2}, as per our XRR measurements), ε_0 is the vacuum dielectric constant, κ_{IPAE}~13 and κ_{PAE}~9 are the relative dielectric constants of the organic SAM (as per C-V measurements) and μ is the molecular dipole along the main axis. Considering the presence of 4 layers of organic materials, the dipole moments for IPAE and PAE are 2.00 D and -1.45 D, respectively (note: "positive" dipole magnitudes indicate a dipole pointing from the OSC towards the dielectric). This result only takes into account the dipole along the molecular axis of the organic portion of the stack, and therefore does not contain information on the position of the anion in the stack. These results are in accordance to previous reports of similar effects.

Nonetheless, the minimum shift of the C-V curves for (I)Z-SAND (*vide supra*) one respect to the other imply that at least part of the effect is due to surface dipoles acting on the OSC surface. This is corroborated by two observations:

1) In going from 1-layer to 4-layer (I)Z-SAND we do not notice a change in the onset voltage for the charge accumulation in the dielectric, hinting that the dipole moment in the stack is only marginally hampering or favoring charge movement throughout the stack;
2) In independent experiments ran by Katie Stallings at Northwestern University we noticed that by varying the distance between the PAE (sandwiched in ZrOx) and the OSC layers and leaving the total thickness of the stack unaltered, one could see a threshold voltage shift towards lower voltages as the spatial distance between the layers increased, implying that at least part of the effect is due to the surface dipole.

Additional seminal experiments ran by Li Zeng using X-Ray Standing Wave techniques seem to hint at a difference in position of the Bromide ions in the (I)Z-SAND stacks, which can probably account for the different dipole of the molecules.

In conclusion, we were able to synthesize and fully characterize a novel phosphonic acid-functionalized azastilbazolium dye, whose SAM-forming properties we studied in detail, with both kinetic studies and X-ray surface techniques. Moreover, we analyzed and compared its dielectric properties in MIS structures and in OFET devices with p- and n-semiconductors, obtaining high quality transistors. Finally, we were able to fine-tune the threshold and switch-on potentials of aforementioned devices by uncapping the dielectric and by functionalizing it with HMDS. Everything we studied aims in the direction of an inversion of the layer dipole, even if we were not yet able to ascertain the position of the bromide and thus first-hand verify this statement.

We are currently investigating the position and the mobility of the bromide in the stack. This approach to dielectrics opens the way to new mixed organic SAMs in SAND structures which would allow the fine tuning of the switch-on voltage as desired and the preemptive design of digital circuitry. We are currently looking into the properties of mixed SANDs, which would offer extreme flexibility in the manipulation of device characteristics.

EXPERIMENTAL

Preparation of the sol-gel solutions: solutions used for the fabrication of the ZrOx layers were prepared by dissolving 93.2 mg of Zirconium(IV) Chloride (Sigma Aldrich) precursor in 4 ml of absolute ethanol affording a 0.1 M solution. After 5 minutes of stirring, 300 mg of 68% wt./wt. HNO_3 are added and the solution is heated at 60°C for 3 hours, then aged at room temperature for 12 hours. From this solution 0.01 and 0.02 M solutions are prepared by dilution with ethanol.

Fabrication of the dielectric stacks: Substrates (2 cm x 2.5 cm, n^{++}-Si/native SiO_2) were cleaned by sonication in ethanol at 50°C for 10 minutes, followed by oxygen plasma cleaning (400-500 mTorr) for 10 minutes. Fabrication of the dielectric stacks is carried out in a Class-10 HEPA filtered laminar flow clean hood (NuAire) to minimize contamination. All substrates are left in methanol during down times and are nitrogen-blown before use. Solutions are filtered through 250 nm HTPE filters. Fabrication can be divided in steps:

- **Step 1, Priming**: The priming metal oxide layer was prepared by spinning the 0.02 M precursor solution at 5000 rpm for 30 seconds, then by baking the substrate at 200°C for 30 minutes.
- **Step 2, Self-Assembly**: The organic molecule was self-assembled on the surface by immersion in a 3mM methanol solution of the azastilbazolium compound of interest (PAE for Z-SAND and IPAE for IZ-SAND). The substrates were cleaned by sonication in methanol for 5 seconds using two different methanol baths.
- **Step 3, Capping:** The capping layer is fabricated by spinning the 0.01 M precursor solution at 5000 rpm for 30 seconds, then baked at 200°C for 30 minutes.

The last two steps (self-assembly + capping) are repeated for the desired amount of layers. The capped stacks were fabricated by exposing uncapped 4 layers stacks to room temperature HMDS vapors for 1 week or by spinning pure HMDS on top of the stack (5000 rpm, 30 s), followed by annealing at 130°C for 20 minutes.

MIS Capacitors: In order to fabricate metal-insulator-semiconductor capacitors, Gold contacts were thermally evaporated at a 0.3 Å/s rate from a base pressure of 3 x 10^{-6} Torr through 200 µm x 200 µm shadow masks. C-V curves were recorded at 10 kHz using a flexible Tungsten 1 µm whisker probe (SE-SM, Signatone) as a cathode and a Beryllium Copper alloy probe (SE-BC, Signatone) as an anode. Leak currents were recorded using the same probes. For high temperature-annealed stacks (tZ-SAND and tIZ-SAND), the substrates were baked at 375°C for 5 minutes in air before Gold deposition.

OFETs: Pentacene (P5, 99%, Sigma-Aldrich) and hexadecafluoro copper phthalocyanine (F16CuPC, 98%, TCI Chemicals) were sublimed twice (base pressure: 7.0 x 10^{-6} Torr) in a three-zone sublimator prior to use. Temperatures for pentacene: 290°C, 275°C, 230°C. Temperatures for F16CuPC: 460°C, 400°C, 300°C. Semiconductors films (50 nm thick) are patterned during thermal evaporation (0.1 Å/s, base pressure 3.5 x 10^{-6} Torr) through 5 mm x 8 mm shadow masks. The substrates were kept at room temperature for the evaporation of P5 and were heated at 125°C for the evaporation of F16CuPC. OFET architecture was completed by thermal evaporation (50 nm, 0.3 Å/s, base pressure 3 x 10^{-6} Torr) of Gold contacts (W = 5 mm, l = 100 µm). Transfer and output plots were recorded using flexible Tungsten 1 µm whisker probes (SE-SM, Signatone) as source and drain contacts, and a Beryllium Copper alloy probe (SE-BC, Signatone) as a gate contact.

AFM Characterization: AFM images were collected on a Bruker ICON System at a frequency of 1.0 Hz in tapping mode, using ACTA-50 n-doped Silicon tips (<10 nm tip radius) from AppNano. Images were elaborated using NanoScope 1.40.

Synthesis of **3:**

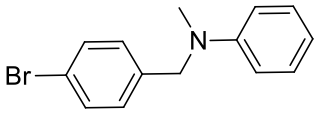

Freshly distilled *N*-methylaniline (6.60 g, 56.56 mmol) was dissolved in 55 ml of anhydrous toluene in a 250 ml one-neck round-bottomed flask. 4-bromobenzyl bromide (14.00 g, 56.00 mmol) dissolved in 11 ml of toluene was added to the solution and the mixture was heated at 65°C for 3 hours under nitrogen atmosphere. 50 ml of water were added and bilayer mixture was sonicated until complete dissolution of the precipitate. Organic phase washed with water (50 x 3), dried on sodium sulfate and evaporated at reduced pressure to afford a pale yellow liquid. The crude was further distilled under high vacuum (0.3 Torr, 60°C) to remove excess starting reagent, affording a yellow viscous oil (yield 85%). Product should be kept refrigerated (solid below 0°C) or can be stored as the stable sulfate salt.

^{1}H-NMR ($CDCl_3$ @ 500 MHz): δ 7.44, m, 2H; δ 7.24, m, 2H; δ 7.12, d, 2H; δ 6.74, m, 3H; δ 4.48, s, 2H; δ 3.02, s, 3H.

^{13}C-NMR ($CDCl_3$ @ 126 MHz): δ 149.52, 138.11, 131.66, 129.24, 128.50, 120.59, 116.89, 112.47, 56.24, 38.59.

High-resolution EI-MS calculated for C14H14BrN: 275.0310. Found: 275.0308.

Synthesis of **5:**

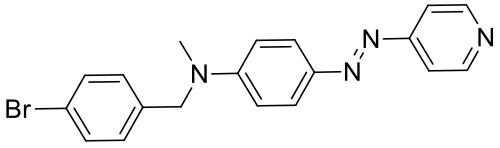

In a 100 ml beaker 4-aminopyridine (2.73 g, 2.9 mmol) was added to 29 ml of water, to which 30 ml of aqueous HBF_4 (48% wt./wt.) were slowly added. The cloudy solution was sonicated for 5 minutes and then cooled down to 0° C via ice bath. $NaNO_2$ (2 g, 29 mmol) was dissolved into 10 ml of water and also cooled down to 0° C, and then slowly added to the first solution. After 5 minutes the diazonium salt is slowly added to an ice-cooled solution of **3** (8.00 g, 29 mmol) in 40 ml of ethanol. Left to react for 10 minutes at 0°C under vigorous stirring, then basified to neutral pH using a 10% wt/wt KOH aqueous solution. Extracted with dichloromethane (70 ml), washed with water (3 x 50 ml). Organic phase is dried on sodium sulfate and evaporated at reduced pressure. The crude oil is filtered through a silica plug under suction using dichloromethane first and a 1:1 dichloromethane : ethyl acetate mixture later. The second fraction is evaporated to afford bright orange crystals (yield 62%).

^{1}H-NMR ($CDCl_3$ @ 500 MHz): δ 8.72, d, 2H; δ 7.89, m, 2H; δ 7.63, m, 2H; δ 7.46, m, 2H; δ 7.08, d, 2H; δ 6.78, m, 2H; δ 4.48, s, 2H; δ 3.02, s, 3H.

^{13}C-NMR ($CDCl_3$ @ 101 MHz): δ 157.85, 152.54, 151.02, 143.97, 136.44, 131.92, 128.13, 126.00, 121.10, 116.01, 111.69, 55.65, 38.95.

High-resolution EI-MS calculated for $C_{19}H_{18}BrN_4^+$ = $(M+H)^+$: 381.0709. Found: 381.0722.

Synthesis of **6:**

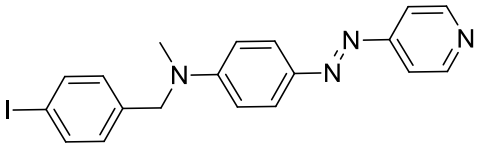

N,*N*'-dimethylethylenediamine (54 mg, 0.60 mmol), anhydrous copper iodide (58 mg, 0.30 mmol), anhydrous sodium iodide (0.89 g, 5.92 mmol) and **5** (1.13 g, 2.96 mmol) were loaded in a 100 ml oven-dried pressure vessel and dissolved in 20 ml of anhydrous 1,4-dioxane. Argon was bubbled in the mixture for 20 minutes, then vessel was sealed and the mixture was heated at 120°C for 48 hours. Water (80 ml) was added, the precipitate was sonicated for 10 minutes, filtered and abundantly washed with deionized water to afford an orange powder (yield 99%).

^{1}H-NMR ($CDCl_3$ @ 500 MHz): δ 8.71, d, 2H; δ 7.87, m, 2H; δ 7.65, m, 2H; δ 7.61, m, 2H; δ 6.94, d, 2H; δ 6.77, m, 2H; δ 4.61, s, 2H; δ 3.16, s.

^{13}C NMR ($CDCl_3$ @ 101 MHz) δ 152.41, 150.80, 143.83, 137.73, 137.01, 128.24, 125.86, 115.91, 111.55, 92.36, 66.91, 55.60, 38.83.

High-resolution EI-MS calculated for $C_{19}H_{18}IN_4^+$ = $(M+H)^+$: 429.0571. Found: 429.0590.

Synthesis of **7:**

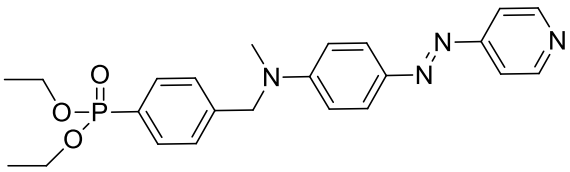

Diethyl phosphonate (0.70 g, 5.14 mmol), tetrakis(triphenylphosphine)palladium(0) (0.28 g, 0.24 mmol), and **5** (2.00 g, 4.67 mmol) were loaded in a 100 ml oven-dried pressure vessel and dissolved in 20 ml of anhydrous tetrahydrofuran. Argon was bubbled in the mixture for 20 minutes, then caesium carbonate (1.67 g, 5.14 mmol) is added, cap is tightened and mixture is heated to 140°C for 30 hrs. Reaction is quenched with water (60 ml) and extracted with dichloromethane. The organic phase is then washed with a saturated aqueous solution of ammonium chloride, dried on sodium sulfate and evaporated at reduced pressure. The resulting oil is filtered on a silica plug under suction with a 1:1 dicholomethane : ethyl acetate mixture first and with a 10:1 ethyl acetate : methanol mixture later. Second fraction is evaporated at reduced pressure to afford a red viscous oil which solidifies upon standing (yield 72%).

^{1}H-NMR ($CDCl_3$ @ 400 MHz): δ 8.74, d, 2H; δ 7.89, m, 2H; δ 7.79, dd, 2H; δ 7.63, d, 2H; δ 7.30, dd, 2H; δ 6.79, m, 2H; δ 4.72, s, 2H; δ 4.12, m; δ 3.20, s, 3H.

^{13}C NMR ($CDCl_3$ @ 101 MHz): δ 157.84, 152.50, 151.02, 144.04, 142.32-142.29 (d, *C*-C-C-C-P), 132.38-132.28 (d, *C*-C-P), 128.51-126.62 (d, *C*-P), 126.48-126.33 (d, *C*-C-P), 125.98, 116.00, 111.69, 62.13-62.08 (d, *C*-O-P), 56.07, 39.11, 16.35-16.28 (d, *C*-C-O-P).

^{31}P-NMR ($CDCl_3$ @ 162 MHz): δ 18.38.

High-resolution EI-MS calculated for $C_{23}H_{28}N_4O_3P^+$ = $(M+H)^+$: 439.1894. Found: 439.1901.

Synthesis of **8**:

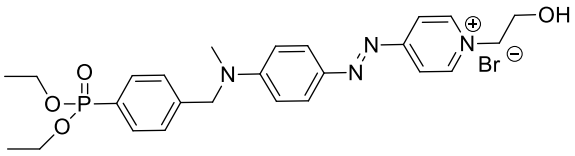

2-bromoethanol (0.60 g, 5.52 mmol) and **7** (0.20 g, 0.46 mmol) were loaded in a 5-ml microwave vial and heated at 60°C for 40 minutes (80 W, air-cooling, no pressure limit). The solution was then evaporated at reduced pressure, dissolved into deionized water and ethyl acetate, extracted 3 times with ethyl acetate and the aqueous phase was evaporated at reduced pressure to afford a tarry golden paste, which solidified upon extensive drying under high vacuum (yield 65%). Compound is very hygroscopic and should be handled under vacuum before next step of the synthesis.

^{1}H-NMR (CD_3OD @ 400 MHz): δ 8.83, d, 2H; δ 8.15, d, 2H; δ 7.98, m, 2H; δ 7.75, dd, 2H; δ 7.40, dd, 2H; δ 6.97, m, 2H; δ 4.93, s, 2H; δ 4.62, t, 2H; δ 4.09, m, 4H; δ 4.00, t, 2H; δ 3.33, s, 3H; 1.29, t, 6H.

^{13}C NMR (CD_3OD @ 101 MHz) δ 163.81, 157.10, 147.32, 146.37 - 144.02 (d, *C*-C-C-C-P), 143.99, 133.36 - 133.25 (d, *C*-C-C-P), 128.90 - 126.99 (d, *C*-P), 128.07 - 127.91(d, *C*-C-P), 119.89, 113.95, 63.92, 63.87, 63.81, 61.75, 56.80, 40.03, 16.63, 16.56.

^{31}P-NMR ($CDCl_3$ @ 162 MHz): δ 18.90.

High-resolution EI-MS calculated for $C_{25}H_{32}N_4O_4P^+$ = $(M+H)^+$: 483.2156. Found: 483.2174.

Synthesis of **IPAE**:

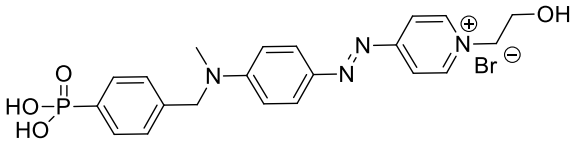

In a flame-dried 10 ml round bottomed flask, **8** was dissolved in anhydrous dichoromethane under a nitrogen atmosphere and the solution was cooled to 0°C via ice bath. Trimethylsilyl bromide was dissolved in 1 ml of anhydrous dichloromethane and added dropwise in a 10 minutes time. Reaction was stirred overnight, then volatiles were evaporated, the residue was dissolved in methanol and the solvent was evaporated again. This is done three times. Eventually the tarry solid is dried under high vacuum to afford a green solid with golden luster (yield 100%).

^{1}H-NMR (CD_3OD @ 400 MHz): δ 8.83, d, 2H; δ 8.15, d, 2H; δ 7.98, m, 2H; δ 7.75, dd, 2H; δ 7.40, dd, 2H; δ 6.97, m, 2H; δ 4.93, s, 2H; δ 4.62, t, 2H; δ 4.09, m, 4H; δ 4.00, t, 2H; δ 3.33, s, 3H; 1.29, t, 6H.

^{13}C NMR (CD_3OD @ 101 MHz) δ 163.81, 157.10, 147.32, 146.37 - 144.02 (d, *C*-C-C-C-P), 143.99, 133.36 - 133.25 (d, *C*-C-C-P), 128.90 - 126.99 (d, *C*-P), 128.07 - 127.91(d, *C*-C-P), 119.89, 113.95, 63.92, 63.87, 63.81, 61.75, 56.80, 40.03, 16.63, 16.56.

^{31}P-NMR ($CDCl_3$ @ 162 MHz): δ 18.90.

BIBLIOGRAPHY

1. Horowitz, G. Organic Field-Effect Transistors. *Adv. Mater.* **10,** 365–377 (1998).

2. Shockley, W. A Unipolar "Field-Effect" Transistor. *Proc. IRE* **40,** 1365–1376 (1952).

3. Hennek, J. W., Kim, M.-G., Kanatzidis, M. G., Facchetti, A. & Marks, T. J. Exploratory combustion synthesis: amorphous indium yttrium oxide for thin-film transistors. *J. Am. Chem. Soc.* **134,** 9593–6 (2012).

4. Chau, R. S. The High-k Solution. *IEEE Electron Device Lett.* at <http://spectrum.ieee.org/semiconductors/design/the-highk-solution>

5. Wannier, G. The Structure of Electronic Excitation Levels in Insulating Crystals. *Phys. Rev.* **52,** 191–197 (1937).

6. Craciun, N., Wildeman, J. & Blom, P. Universal Arrhenius Temperature Activated Charge Transport in Diodes from Disordered Organic Semiconductors. *Phys. Rev. Lett.* **100,** 056601 (2008).

7. Klauk, H. Organic thin-film transistors. *Chem. Soc. Rev.* **39,** 2643–66 (2010).

8. Sze, S. M. *Physics of Semiconductor Devices*. 868 (John Wiley & Sons, 1981). at <http://books.google.com.au/books/about/Physics_of_Semiconductor_Devices.html?id=LCNTAAAAMAAJ&pgis=1>

9. Horowitz, G. Organic thin film transistors: From theory to real devices. *J. Mater. Res.* **19,** 1946–1962 (2011).

10. Mottaghi, M. & Horowitz, G. Field-induced mobility degradation in pentacene thin-film transistors. *Org. Electron.* **7,** 528–536 (2006).

11. Chua, L.-L. *et al.* General observation of n-type field-effect behaviour in organic semiconductors. *Nature* **434,** 194–9 (2005).

12. Kobayashi, S. *et al.* Control of carrier density by self-assembled monolayers in organic field-effect transistors. *Nat. Mater.* **3,** 317–22 (2004).

13. Knipp, D., Street, R. A., Völkel, A. & Ho, J. Pentacene thin film transistors on inorganic dielectrics: Morphology, structural properties, and electronic transport. *J. Appl. Phys.* **93,** 347 (2003).

14. Kymissis, I., Dimitrakopoulos, C. D. & Purushothaman, S. High-performance bottom electrode organic thin-film transistors. *IEEE Trans. Electron Devices* **48,** 1060–1064 (2001).

15. Hong, J.-P. *et al.* Tuning of Ag work functions by self-assembled monolayers of aromatic thiols for an efficient hole injection for solution processed triisopropylsilylethynyl pentacene organic thin film transistors. *Appl. Phys. Lett.* **92,** 143311 (2008).

16. Queffélec, C., Petit, M. & Janvier, P. Surface modification using phosphonic acids and esters. *Chem. Rev.* (2012). at <http://pubs.acs.org/doi/abs/10.1021/cr2004212>

17. Kraft, U. *et al.* Fluoroalkylphosphonic acid self-assembled monolayer gate dielectrics for threshold-voltage control in low-voltage organic thin-film transistors. *J. Mater. Chem.* **20,** 6416 (2010).

18. Ha, Y. *et al.* Solution-deposited organic-inorganic hybrid multilayer gate dielectrics. Design, synthesis, microstructures, and electrical properties with thin-film transistors. *J. Am. Chem. Soc.* **133,** 10239–50 (2011).

19. Acton, O. *et al.* Dielectric surface-controlled low-voltage organic transistors via n-alkyl phosphonic acid self-assembled monolayers on high-k metal oxide. *ACS Appl. Mater. Interfaces* **2,** 511–20 (2010).

20. Zhang, B., Liu, Y., Agarwal, S., Yeh, M.-L. & Katz, H. E. Structure, sodium ion role, and practical issues for β-alumina as a high-k solution-processed gate layer for transparent and low-voltage electronics. *ACS Appl. Mater. Interfaces* **3,** 4254–61 (2011).

21. Cho, J. H. *et al.* Printable ion-gel gate dielectrics for low-voltage polymer thin-film transistors on plastic. *Nat. Mater.* **7,** 900–6 (2008).

22. Everaerts, K. *et al.* Ambient-processable high capacitance hafnia-organic self-assembled nanodielectrics. *J. Am. Chem. Soc.* **135,** 8926–39 (2013).

23. Facchetti, A. *et al.* Design and Preparation of Zwitterionic Organic Thin Films: Self-Assembled Siloxane-Based, Thiophene-Spaced N -Benzylpyridinium Dicyanomethanides as Nonlinear Optical Materials. *Langmuir* **17,** 5939–5942 (2001).

24. Beverina, L. & Pagani, G. A. π-Conjugated Zwitterions as Paradigm of Donor-Acceptor Building Blocks in Organic-Based Materials. *Acc. Chem. Res.* (2013). doi:10.1021/ar4000967

25. Delaire, J. A. & Nakatani, K. Linear and Nonlinear Optical Properties of Photochromic Molecules and Materials. *Chem. Rev.* **100,** 1817–1846 (2000).

26. Tian, M., Furuki, M., Iwasa, I. & Sato, Y. Search for squaraine derivatives that can be sublimed without thermal decomposition. *J. Phys. Chem. B* 4370–4376 (2002). at <http://pubs.acs.org/doi/abs/10.1021/jp013698r>

hapter IV:

Stokes shift/emission efficiency trade–off in donor-acceptor perylene monoimides for luminescent solar concentrators

THEORETICAL INTRODUCTION

We have discussed the capabilities of recent photovoltaic systems and have analyzed some techniques employed to improve the efficiencies of this budding and fundamental technology. While we have dealt with the tinkering of cell parameters by working on the molecular and supramolecular structure of its components, we have not addressed the possibility of new engineering schemes. Before discussing this a very brief introduction about geometrical optics and total reflectance is in order.

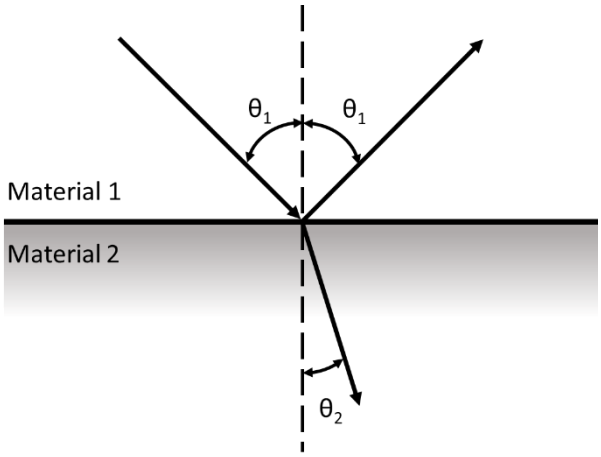

***Figure 63**: refraction and reflection of radiations at the interface between two non-absorbing isotropic continua.*

Let us consider an electromagnetic wave impinging on the interface between two materials with an angle θ_1 with respect to the normal. If we stick to geometrical optics and do not venture in the wave formalism, it is possible to argue that part of the radiation is reflected by the interface with an angle θ_1, while part of the radiation will pass in the second material forming an angle θ_2 with the normal.

Snell's law states that the relationship between the two angles is strictly dependent on the refractive indices of the two materials involved, namely n_1 and n_2. The refractive index, also known as optical density, can be defined as the ratio between speed of light in a vacuum and speed of light in the medium, that is

$$n = \frac{c}{v}$$

(this only refers to the phase velocity of the light and not to the group velocity, therefore n can be less than 1 and, in the case of metamaterials[1], less than 0). Optical densities are a function of the wavelength of the electromagnetic wave, and can be modeled as a sum of a real and imaginary part.

Snell's law can be derived from Fermat's *principle of least time*[2] and states the following:

$$n_1 \sin\theta_1 = n_2 \sin\theta_2$$

This implies that the ratio of the optical densities is able to predict exactly how a ray of light will behave in a medium. If, for example, we set θ_1 as $\pi/2$, the resulting equation is

$$\sin\theta_2 = \frac{n_1}{n_2} \rightarrow \theta_2 = \arcsin\frac{n_1}{n_2}$$

This is known as critical angle, and indicates the angle at which the impinging light is not refracted at the interface inside the second material, but only reflected, causing a phenomenon called total internal reflection (TIR, **Figure 64**). This phenomenon can only take place when the ratio between n_1 and n_2 is less

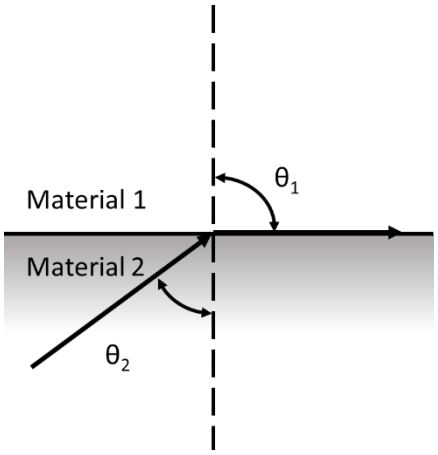

***Figure 64:**. conditions of total internal reflection in an interface between two different materials.*

than 1, i.e. when $n_1<n_2$. The direct implication is that when light is travelling from a higher refractive index to one of lower refractive index if it hits the interface at an angle greater than the critical one all of the radiation will be reflected inside the material with the higher refractive index.

***Table 6:** refractive indices for typical optically used materials.*

Material	n @ 589 nm
Vacuum	1
Air	1.000293
Water	1.333
PMMA	1.49
Diamond	2.42
Glass	1.46

Some typical refractive indices are reported in Table 1. Polymethyl methacrylate (PMMA), water and glass are all materials which can show total internal reflection. Attenuated Total Reflectance (ATR) modules are used in Fourier transform infrared spectroscopy and greatly simplify the operation of FT-IR machinery. Optical fibers exploit the higher refractive index of glass with respect to air to create TIR and avoid loss of signal during the transmission of information.

TIR is also central in the technology used for luminescent solar concentrators (LSC), which are a range of technologies focused on the improvement and ease of application of photovoltaics. A schematic of an LSC is shown in **Figure 65**.

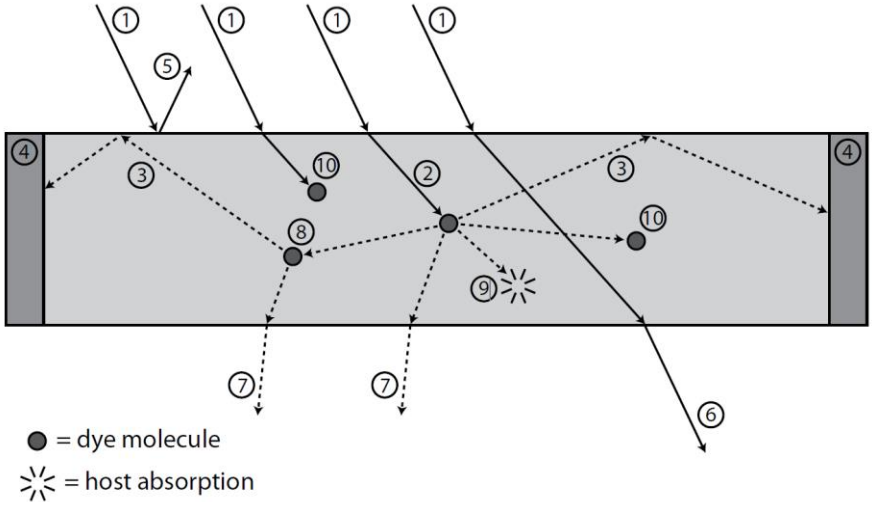

***Figure 65**: schematic working principle of a LSC; the different elements of the picture are described throughout the text. Adapted from reference*[42]

The typical LSC consists of a sheet of transparent material (host) which has been doped with a fluorophore. Namely, a fluorophore is a material capable of absorbing incident radiation and emitting fluorescence photons at a lower energy. By connecting solar cells to the edges of the sheet, these concentrated photons can be easily converted into electricity.

With reference to **Figure 65**, what follows is a quick description of the various elements:

1) Incident light, impinging on the surface of the host material. The intensity of the radiation is usually non-relevant for the functioning of the device, mainly because the device itself acts as a concentrator (see point 3) and is able to convert both direct sunlight and diffuse light into useful radiation for the solar cells[3].
2) Refracted light inside the host. Not all of the refracted radiation will reach the dye, mainly because whatever type of host we are using, we are sure at least a part of the radiation will be absorbed (e.g. photons whose energy is above 8 eV will be absorbed by Silicon Oxide, 700 nm red light will be absorbed by stretching and bending overtones in PMMA, see point 9). The refractive index of the host material has to be lower than the refractive index of air, to ensure TIR[4]. The remaining radiation will be ideally absorbed by the fluorophore, depending on the absorption coefficient of the fluorophore employed.
3) The fluorophore will emit light inside the slab of host material. The quantity of emitted light is strictly dependent on the fluorescence quantum yield of the molecule we are using. The radiation whose angle of incidence against the host-air interface is greater than the critical angle will be completely reflected inside the host matrix.
4) The fluorescence will thus be directed to the side solar cells. If the emission spectrum of the fluorophore is superimposable with the absorption spectrum of the solar cell, light will be absorbed and converted into electricity following the solar cell parameters (See Chapter II).
5) Some of the impinging light will be reflected by the host surface and therefore should not be taken into account when considering the final efficiency of the device.
6) Depending on the amount of the fluorophore and on its absorption spectrum, some of the light might not be absorbed by the LSC and could pass unscathed though the whole device.
7) Fluorescence from inside the slab which impinges on the interface at an angle lower than the critical one is partially transmitted to air and is therefore lost.
8) Some of the emitted light inside the slab might be reabsorbed by another molecule of fluorophore. This is strictly dependent from the difference between the absorption and emission spectra of the molecule and their shift one respect to the other (i.e. the so-called Stokes shift[5]).
9) As mentioned above, some of the light might be absorbed by the host itself before or after the fluorescence event.
10) Depending on the fluorescence quantum yield of the materials involved, only a certain percentage of the absorbed photons will be re-emitted as fluorescence. A part of the radiation might simply be absorbed by the material and the electrons in the first excited state might thermalize to the ground state.

From the above-reported analysis it is clear that the dye and the host have a central role in determining the total efficiency of the concentrator. In particular, some of the most important parameters are the refractive index of the host, the absorption coefficient of the dye, its thermo- and photostability, its Stokes shift and its quantum yield of fluorescence.

Several different loss mechanisms were mentioned above in the description of LSC operation. The reduction or elimination of these losses is one of the major challenges in LSC development.

The overall optical efficiency of an LSC, η_{OPT}, is defined as the ratio between the power collected at the edges of the LSC and the light impinging on the surface of the host. This efficiency takes into account all the losses of each process inside the LSC[6].

$$\eta_{OPT} = (1 - R) \cdot P_{TIR} \cdot \eta_{ABS} \cdot \Phi \cdot \eta_{St} \cdot \eta_{TIR} \cdot \eta_{Host} \cdot \eta_{Self}$$

This equation is in truth simplified, since the real factors are interdependent.

(1-R) is the loss of radiation due to the Fresnel reflection at the surface of the host material. It can be shown[7] that in the case of normal incidence,

$$R = \left(\frac{n-1}{n+1}\right)^2$$

R is usually around 4% for a PMMA matrix (n=1.49, ref **Table 1**), allowing ~96% of the incident radiation into the LSC. P_{TIR} is the efficiency of total reflection, and is mainly ascribed to the presence of loss cones after fluorescence when the emitted light doesn't impinge on the surface with an angle greater than the critical one. It can be shown[8] that the radiation loss due to missed TIR is

$$P_{TIR} = \frac{\sqrt{n^2 - 1}}{n}$$

and that the product of (1-R) and P_{TIR} has a minimum for n~2.0, as shown in **Figure 66**. The total loss for n=1.49 is ~25%. There are ways to reduce this number, obviously, such as applying reflecting coatings to the top and bottom of the host matrix.

η_{ABS} is determined by the matching of the absorption spectra of the dye and the absorption spectra of the solar cell. To maximise the power output, the LSC sheet has to absorb the greatest possible range of incident solar wavelengths with corresponding photon energies greater than the bandgap of the solar cells at the edges of the sheet. A sheet which can absorb all incident wavelengths below 550 nm, for example, has η_{ABS} = 0.26, since 26% of the AM1.5g solar spectrum lies below this wavelength[9]. For optimum performance with Si cells, the sheet should ideally absorb all wavelengths < 950nm and emit in

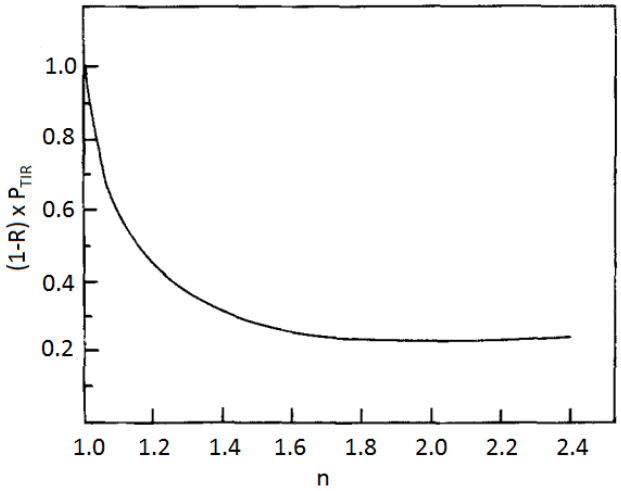

Figure 66: *trend of the (1-R)xPTIR function, showing a slight minimum for n~2.0. Adapted from reference[9].*

the 950-1000 nm range, which corresponds to the maximum spectral response of the cell. If it becomes possible to absorb all wavelengths <950 nm, η_{ABS} increases to 0.71.

Φ indicates the fluorescence quantum efficiency of the dye in the LSC. A quantum yield is essentially a probability of reemission after a photon has been absorbed. This number needs to be high to take into account multiple absorption-emission events inside the slab, since each single event counts in the computation of the total efficiency. For example, if Φ=95%, 5 consequent absorption-emission events lower the total efficiency to $(0.95)^5$=0.77.

η_{ST} is the efficiency of the Stokes shift. While a mismatch between the absorption and the emission of the dye is useful to avoid reabsorption (which, as we have just shown, lowers the number of total emitted photons due to non-unity Φ), it also inherently lowers the energy of the photons, since in linear optics the energy of an emitted photon is always lower than the absorbed one. One useful parameter to determine the efficiency of the Stokes shift is calculating how much the absorption and the emission spectra can be superimposed, expressed in percentages.

η_{TIR} indicates the efficiency of the TIR process. While theoretically this phenomenon should have unitary efficiency, the presence of foreign particles such as dust or moisture droplets on the surface of the sheet can cause light to be scattered out of the sheet. Physical damage to the sheet surface, such as scratching, will obviously result in the loss of trapped light. In addition, the surface may possess a microstructure, depending on the method of manufacture, which will also lead to a loss. It has been reported[10] that carefully cleaned PMMA surfaces measured fractional losses as low as 0.0002 per reflection, corresponding to η_{TIR} = 0.9998. Surface microstructure in the 0.1-1 μm size range were also observed. It was concluded that this formed during the shrinkage of the PMMA in the glass-plate mold, despite the PMMA remaining in contact with the surface of the glass. Whatever the cause of the loss, it only results in an extremely small decrease in trapped fluorescence, even after several hundred reflections (i.e, the fraction remaining after 200 reflections is $(0.9998)^{200}$ = 0.96).

η_{HOST} describes the efficiency of light transmission throughout the bulk of the LSC host matrix. While of little importance at visible wavelengths, where most polymers and glasses are highly transparent[11], care must be taken when operating at near-infrared (NIR) wavelengths above 700 nm, as many polymers exhibit strong absorption in this region from overtones of IR-active stretches[12]. For a PMMA host and fluorescence in the visible region, η_{HOST} is typically 0.95-0.98.

η_{SELF} takes into account the possibility of reabsorption of an emitted photon by a dye molecule, and is strictly dependent on the Stokes shift of the dye, where the higher the Stokes shift, the lower the self-absorption becomes[13]. Although it may seem at first that re-absorption could help to reduce escape-cone losses by re-directing escape-cone photons back into the sheet, this is less likely to occur as the pathlengths involved are on the order of the thickness of the sheet, rather than the length or width. Photons in an LSC can experience multiple re-absorption events, each one increasing the chance of the photon being lost. η_{SELF} for an LSC containing an organic dye is typically on the order of 40-80 %, although this depends greatly on concentration and Φ.

With all this being said, obviously not all the factors are equally important in the evaluation of the total efficiency of an LSC module. The most relevant parameters are P_{TIR}, η_{ABS}, η_{ST}, η_{SELF}. These must be improved to achieve higher LSC efficiencies. Improving P_{TIR} is difficult, since it only depends on the refractive index of the host, which offers little variations. However, several manufacturing techniques can be used to

reflect some of the escape-cone losses back into the bulk of the LSC. Among them, hot mirrors, photonic filters[14], and oriented dyes[15]. η_{ABS} can be increased by using a mixture of several dyes in either the same or multiple LSC sheets to increase the absorption range, although problems arise because of the generally lower Φ of longer-wavelength dyes[16]. η_{ST} will always be present, as it is inherent in the wavelength-shifting process which occurs in an LSC. It is a tradeoff with η_{SELF}, which can be lowered by increasing the Stokes shift.

Materials - Hosts

As should be clear by now, the materials employed in the fabrication of LSCs are of the utmost importance when trying to maximize their efficiencies. Hosts are definitely one of the most prominent components in the manufacturing of the modules, and historically two main materials have been used as a host: glass and PMMA.

By far the most common host material is the polymer poly(methyl methacrylate), also known as PMMA (**Figure 67b**) or Plexiglas. Its main advantages are its low cost, high optical clarity and the ease of doping with fluorophores as these can simply be dissolved in the monomer prior to polymerisation. It also has good photostability, with lifetimes of up to 17 years.

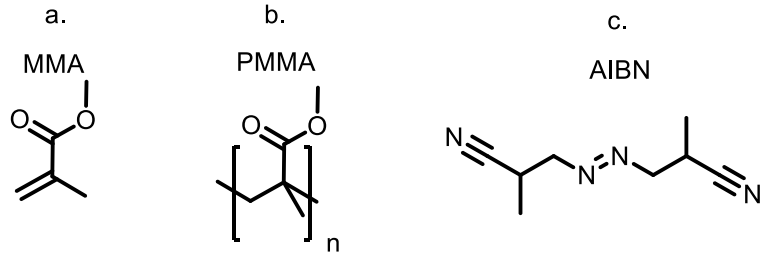

Figure 67*: chemical structures of (a) methylmethacrylate, MMA, (b) polymethymethacrylate, PMMA, and (c) azobisisobutyronitrile, AIBN.*

MMA is a liquid and needs to be cast into a mold before controlled polymerization can occur. Usually LSCs employ PMMA polymerized through radical reactions, which are brought out by including a small amount of thermal radical initiators such as azobisisobutyronitrile (AIBN, **Figure 67c**) in the prepolymer.

The polymer is denser than the monomer, and therefore a reduction in volume occurs during the thermal casting of the host. In order to avoid excessive shrinkage the monomer is partially polymerized until it obtains the consistency of a thick syrup, and then it is cast in the mold and polymerized at 60°C in a water bath with efficient heat distribution.

Due to the substantial increase in density as the reaction progresses the slabs thus obtained need to be post-cured at a temperature higher than the glass temperature of PMMA (i.e. T_g=105° C) in order to either remove or react the remaining unreacted monomer. Its presence, in fact, if left unchecked can alter the refractive index of the mold and affect the photostability of the dyes[17].

However, although PMMA exhibits good optical transparency in the visible region of the spectrum, it begins to show absorption peaks above 700 nm. These are caused by harmonics and overtones of the C-H and C-O bond vibrations in the molecule, and are common to all polymers in which these bonds are present. Host absorption losses therefore become significant when using fluorophores with emission wavelengths >700 nm.

In addition to host absorption, the C-H and C-O vibrations can lead to an increased probability of non-radiative relaxation of the flurophore when the energy gap of the fluorophore corresponds to the bond frequencies, leading to a reduction in quantum yield. These problems can be reduced by either deuterating or fluorinating the host polymer. The larger, heavier deuterium and fluorine atoms shift the absorption peaks, reducing the probability of host absorption and leading to an increase in quantum yield.

Glass has also been used as a host material. Because of its inorganic nature, it has higher transparency in the NIR region when compared with plastics and it is not subject to photodegradation. However the high temperatures (> 600°C) used to cast the melt make the use of organic dyes or quantum dots totally impossible.

Instead of producing glass from a melt, it can also be prepared from a sol-gel, which allows the process to be carried out at room temperature[18]. It becomes possible to incorporate a range of different fluorophores into the glass material, including organic dyes and rare-earth or inorganic ions.

Since they are entirely inorganic, sol-gel glasses do not suffer from photodegradation and show improved transparency in the NIR compared with polymers. The range of pore sizes in the final glass is in the range 1.5-10 nm, which is much smaller than the wavelength of visible light. As a result, they are transparent and exhbit little scattering at wavelengths above 250 nm.

Liquids have also been used as host materials[19]. The solvent in which the dye was dissolved was contained between two glass plates to form a large, thin cuvette. The main motivation has been the limited photostability of the organic dyes which were used. Using a solution of the dye made it possible to easily replace the dye once it had photodegraded. However, the availability of dyes with good photostabilities renders this an uneccessary and impractical method.

Materials – Dyes

Nanocrystals of inorganic compounds such as lead sulphide (PbS) or lead selenide (PbSe) (called quantum dots) exhibit broad absorption spectra, high absorption coefficients and emission wavelengths which can be tuned from 850 nm to 1900 nm by simply altering the diameter of the quantum dot[20].

Although Φ of up to 80% have been achieved for laboratory-produced quantum dots[20], commercial quantum dots are limited to 30-50% and are both expensive and exhibit poor photostability[21].

Figure 68 shows absorption and emission spectra of both cadmium selenide/zinc sulphide (CdSe/ZnS) core/shell quantum dots with a diameter of 5 nm and PbS quantum dots with a diameter of 8 nm. The PbS dots are capable of absorbing all wavelengths below 900 nm, an ideal characteristic for LSC use.

However, despite the wide absorption range, there is still a large overlap of the absorption and emission spectra. Combined with the relatively low quantum yield compared with the near-unity quantum yield of the Lumogen organic dyes (*vide infra*), this results in large reabsorption losses. Furthermore, the widths of the absorption and emission spectra (and hence the amount of spectral overlap) are determined by the distribution of diameters in a quantum dot sample.

Improvements in quantum dot production techniques which result in a narrower size distribution could result in lower re-absorption losses from quantum dot samples.

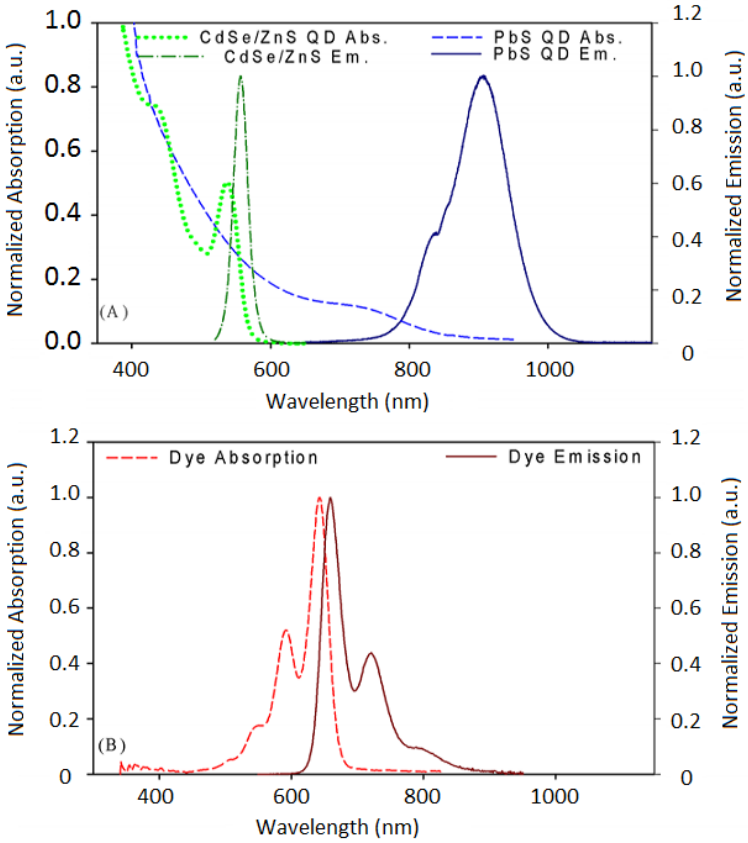

Figure 68: *absorption and emission spectra for (above) inorganic QDs and (below) Lumogen Red F300t. Adapted from reference*[43]*.*

Organic dyes, on the other hand, are cheaper to produce on a large scale and some classes of organic dyes show impressive themo- and photostability, but usually lack the panchromatic absorptions of QDs. Several types of dye have been used thus far in LSCs, among which we can find rhodamines and coumarines, oligothiophenes, phycobilisomes, merocyanine and perylenebisimides. A summary of the most used structures is reported in **Figure 69**. Among these we can identify coumarins[22] (**Figure 69a**), which feature high Φ, elevated molar extinction coefficients, good Stokes shifts but low photostabilities, albeit higher than rodamines (**Figure 69b**). The latter, on the other hand, have very high (close to unity) Φ, low Stokes shift (the superimposition of emission and absorption is 48% of the total spectrum for Rodamine 6G) and limited photostability. These two classes of dyes, which constitute the historical bulk of dyes used in the '80s for LSCs, are in truth better employed as lasering dyes[23] and/or fluorescent biological probes[24], where the irradiation time is shorter and weaker or the dye can be easily substituted once it photodegrades.

Another interesting class of molecular absorbers is the cyanine one (**Figure 69c**). Their high conjugation leads to absorptions in the red and NIR regions (which is in the interesting range for the inorganic solar cells on the edge of the slab), but show limited photostability and low fluorescence quantum yields. Recently a cyanine-based colorless LSC module with very low dyes loading (~5 mg per liter of syrup) and Φ~0.3 has shown >0.4% efficiencies[25]. If the losses in this system were to be minimized, the result would be incredibly interesting for the architectural world.

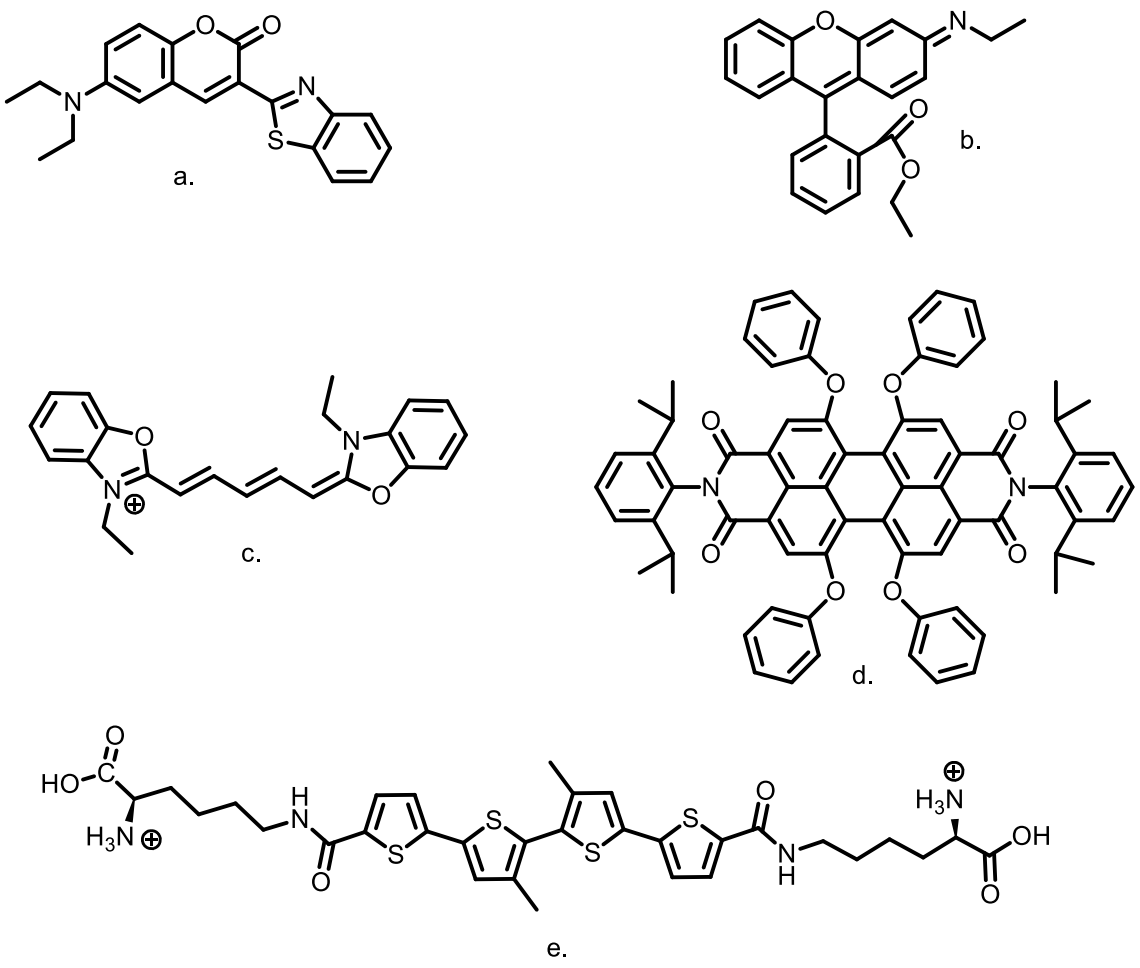

Figure 69: *main organic dye structures employed in LSC literature: (a) Coumarin 6; (b) Rhodamin 6G; (c) cyanine derivative; (d) Lumogen Red F300; (e) biologically-functionalized oligothiophene.*

As of now, some of the most interesting dyes, showing enhanced photostability, very high absorptions, and near-unity quantum yields are the rylene family dyes[26]. The most relevant are probably the BASF Lumogen series ones (**Figure 69d**), whose planar structure has been twisted by the introduction of bulky phenoxy substituents in *bay* position. This, aided by the 2,6-diisoproplylbenzyl moieties on the imidic nitrogen, affords enhanced solubility and ease of processability. Nonetheless, as is shown in **Figure 68,** their Stokes shift is limited, and thus the energy loss is significant.

Recently a lysine-functionalized quatertiophene[27] has been synthesized and incorporated in silk fibers to afford eco-sustainable LSC (**Figure 69e**). This system showed interesting Stokes shift (~130 nm) but limited absorption in the NIR region (where most of the solar radiation is). Nonetheless, if the absorption and emission were to be bathocromically shifted the resulting LSC could be of interest, mainly because of its green approach (water is the only solvent used in the fabrication of the module).

The photostability of these dyes largely depends on the processing parameters of the host slab. In the case of PMMA, in fact, the presence of oxygen can lead to singlet oxygen generation and to the subsequent bleaching of the dye by reactive oxygen species-mediated oxidation[28].

RESULTS AND DISCUSSIONS

By the hereby reported summary one can easily understand that as of now, the most interesting candidates for LSC modules are perylenediimides (PDIs). In fact, PDIs are highly absorptive, efficiently fluorescent, highly stable and compatible with direct radical bulk polymerization of various monomers, including MMA. The latter feature enables the straightforward and low cost production of doped PMMA slabs by cast molding of a solution of PDI in MMA[3].

Thus, the only real limitation of such compounds lies in a strong superimposition of their emission and absorption spectra, direct consequence of their planar, rigid and symmetric molecular structure. Re-absorption losses limits the dimensions of single layer LSC based on PDIs.

Molecules featuring a large Stokes shift pertain to two main classes, having in common a large change in the molecular structure upon optical excitation:

a) donor-acceptor derivatives (D-A);

b) twisted (TW) structures.

In D-A derivatives the optical transition involves a redistribution of the electron density from an electron-rich group (the donor) to an electron-poor one (the acceptor), through a conjugated bridge. This is by far the broader class of large Stokes shift derivatives, finding applications for example in fluorescence bio-imaging. Efficient D-A fluorophores feature rigid, planar and easily polarizable conjugated bridges enabling for large changes in the electronic distribution upon optical excitation.

Conversely, TW molecules possess conjugated bridges having substantial deviation from planarity. The p-terphenyl molecule represents a good example of this class of materials. Optical excitation involves a transition from the aromatic and twisted ground state structure to a quinoidal excited state structure having formal double bonds connecting the neighboring benzene rings.

The resulting major variations in the molecular electronic structure translates into a large Stokes shift[29,30].

While the PDI core cannot be manipulated to fit in any of two such classes, perylenemonomides (PMIs) can display a rather pronounced D-A character, provided that they carry a strong electron donating substituent in one or both free *peri* positions[31]. Also, substitution at the same positions with bulky arenes, leads to TW-type structures having relevant Stokes shifts, as recently demonstrated by the PMI dimers prepared by the Langhals group[32].

In specific cases, i.e. when the arene introduced at one of the free *peri* positions is bulky and is also a donor group, the resulting PMI will behave according to a combination of the D-A and TW governed regimes. The capability to control the interplay of the TW vs. D-A contributions in PMIs could provide a unique tool for further optimization of these compounds for LSC applications. In fact, while twisted structures usually feature high fluorescence efficiency and modest molar absorptivity, the opposite occurs for donor-acceptor compounds.

Part of this thesis has been dedicated to understanding and defining the optoelectronic characteristics of a range of PMI materials, and the influence of the donor residue electronic and steric characteristics on the Stokes shift and emission efficiency for single layer LSC.

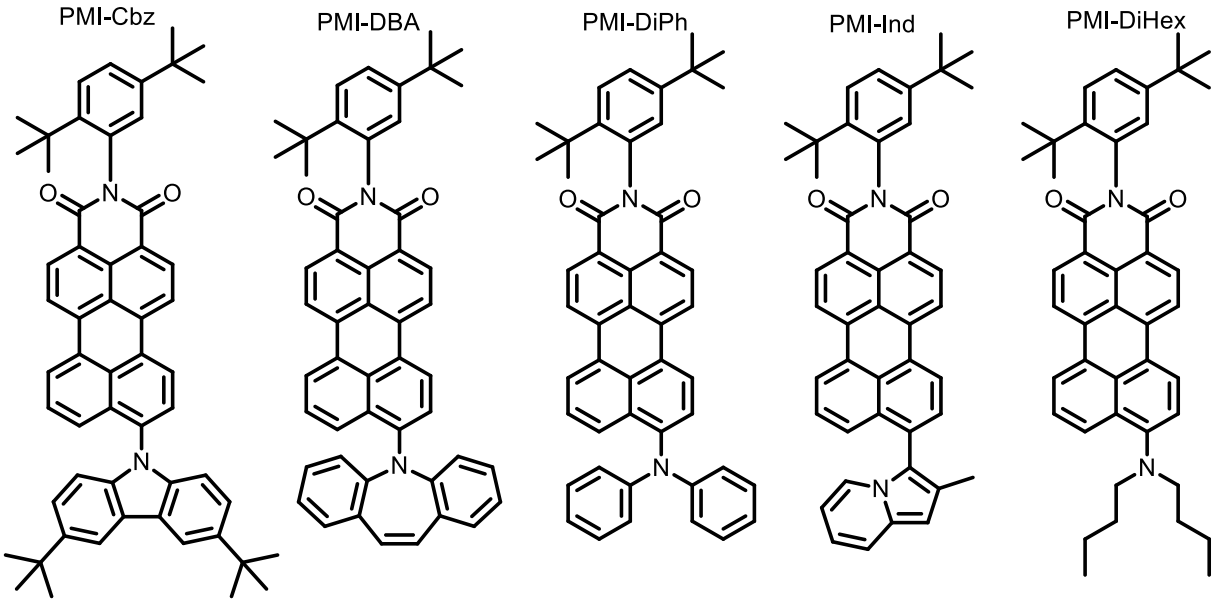

Figure 70: *PMIs synthesized and characterized in this work.*

The objective molecules are a series of partially twisted fluorophores obtained from a common PMI skeleton, where the oscillation strength of the D-A moieties is regulated through the change of the donating moity in *peri* position. These moieties, except for **PMI-Ind**, all show the same source of electron-richness, i.e. a nitrogen atom lone pair, whose electronic surrounding changes according to the nature of the donating moiety.

PMI-Ind features an indolizine donor where the nitrogen lone pair involved in the substituent π orbital makes the pentatomic ring π-excessive, and thus electron donating. The molecule is connected to the PMI core through its 1-position. This is the only member of this series featuring a carbon-carbon bond between the donor and the perylene core.

PMI-Cbz possesses a carbazole donor directly connected to the perylene core through the nitrogen atom. Since the central ring of carbazole is aromatic the nitrogen lone pair, involved in the carbazole π orbital, is not particularly prone to delocalization towards the PMI electron-withdrawing end.

PMI-DiPh and **PMI-DiBut** have already been described in the literature as D-A molecules[33,34]. In terms of donating capabilities, it can be anticipated that a dialkylamine will be a stronger donor due to the lack of delocalization of the nitrogen lone pair over aryl substituents rather than the perylene core. Moreover, **PMI-DiBut** is the only member of the series that can be described as a purely D-A molecule without TW contribution, mainly due to the total lack of lone pair delocalization.

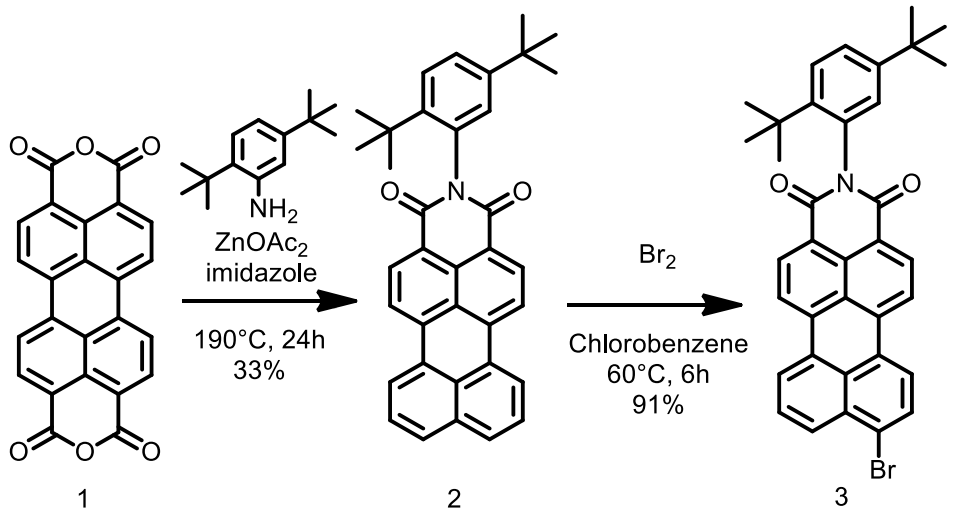

***Scheme* 10**

Finally, **PMI-DBA** features a dibenzoazepine donor, directly connected with the perylene core though its nitrogen atom. The central ring of the dibenzoazepine features 8 π electrons, and as such it is by definition antiaromatic (Hückel rule, stating that systems with 2n electrons are antiaromatic). Thus, the nitrogen lone pair should be extremely prone to delocalization, since the dibenzoazepine ring would gain aromatic stabilization. It should be noted that Hückel's definition applies to monocyclic, planar compounds[35]. The case of dibenzoazepine is slightly more complicated than that, and therefore deviations from a purely antiaromatic behavior are to be expected[36].

Synthesis

The synthesis of the target derivatives is reported in **Scheme 2**. The key intermediate for all of the compounds is the unsubstituted perylene monoimide **2**. The latter can be prepared, according to the method of Langhals[37], by the condensation/decarboxylation reaction of perylendianhydride **1** and 3,5-di(*tert*-butyl)aniline (**Scheme 1**)

This reaction was carried out using imidazole as the solvent and in the presence of zinc(II) acetate in a steel autoclave at 190°C for 24 h. Pure compound **2** is isolated in 33 % yield after chromatographic purification. Regioselective bromination of **2**, following Nagao procedure[38], affords halogenated derivative **3** in 91% yield after chromatographic purification.

PMI-Ind was prepared by direct arylation of 2-methylindolizine with bromide **3**. Recent developments in oraganometallic catalysis have ushered chemistry in a new exciting era of direct arylation. This type of reactions are becoming relevant due to the lack of toxic/difficult to remove organometallic intermediates and the generally high yields, once the reaction conditions are optimized.

We obtained the best results working under Fagnou conditions[39], using DMAc at 100 °C with a Palladium(II) Diacetate/tricyclohexylphosphine tetrafluoroborate catalyst/ligand tandem in the presence of pivalic acid and potassium carbonate as a base. Against all predictions, **PMI-Ind** proved to be unstable in air.

Subjecting **3** to Buchwald-Hartwig amination[40] conditions using 4,7-di-*tert*-butylcarbazole, diphenylamine, dibutylamine and dibenzoazepine afforded compounds **PMI-Cbz** (41%), **PMI-DiPh** (70%), **PMI-DiBut** (75%) and **PMI-DBA**, respectively.

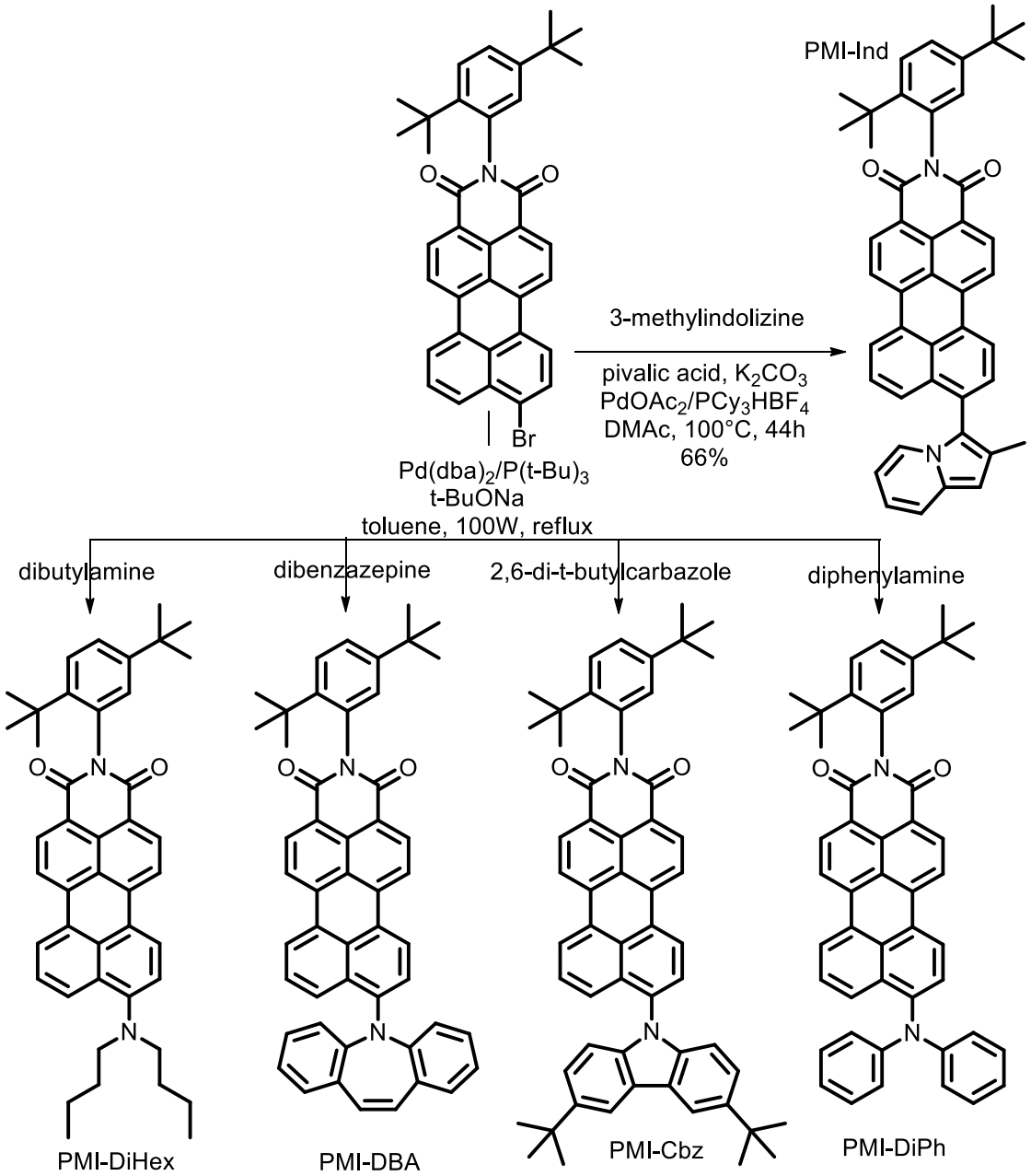

Scheme 11

The reaction conditions were the same for all of the compounds: we used a Palladium(0) dibenzylacetone /tri(*tert*-butyl)phosphine catalyst/ligand tandem in refluxing toluene with sodium *tert*-butanoate as the base.

While tributylphosphine is a dangerous material (it is pyrophoric when exposed to air), the extreme electronrichness of the central Phosphorous is of the utmost importance for the oxidative addition step

in the catalytic cycle. On the other hand, the presence of bulky substituents on the ligand is fundamental during the ligand exchange step, where the steric encumbrance of the tertiary carbons help drive the reaction towards the elimination of the phosphine. The pyrophoricity of the material can be counteracted by using a solution of the ligand in anhydrous toluene.

Even if sodium *tert*-butanoate is more sensitive to water than its potassium counterpart, its use is favoured because the byproduct of the coupling reaction, sodium bromide, is less soluble in toluene than potassium bromide, thus driving the reaction forward by precipitating from toluene.

These reactions where brought out under microwave irradiation for 6-8 hours. Microwave irradiation has thus far provided affordable, fast and reliable synthetic pathways with great advantages on their thermal counterpart. It is especially relevant during metal-catalyzed cross-couplings, where reaction times can be severely shortened (see Chapter 3, C-P coupling).

The conversion to the desired product was complete in all cases, with yields reflecting the nucleophilicity of the donor nitranion.

Molecular Computations

In order to obtain insights into the electronic structure and geometry of the PMI derivatives, and in particular into the molecular planarity upon donor variation, we carried out molecular orbital computations.

Figure 71 shows the calculated ground state geometries, HOMO and LUMO energies, torsional angle between donor and perylene core, and the dipole moments of the 5 products, together with the reference molecule PMI-Qs. **PMI-Ind** and **PMI-Cbz** exhibit remarkably large torsional angles with respect to the perylene core (61° and 62°, respectively).

MO calculations afford a higher ground state dipole moment for **PMI-Ind** (5.93 Debye) than for **PMI-Cbz** (4.75 Debye). **PMI-DiPh** is also considerably twisted (45°) and shows a calculated dipole moment of 6.70 Debye, which is larger than both **PMI-Ind** and **PMI-Cbz**.

Finally, **PMI-DBA** structure shows that the central ring of the dibenzoazepine residue is sizably bended (its two benzene rings forming an angle of 122°). This is consistent with the reported X-Ray structure of dibenzazepine.

Moreover, the whole donor residue is almost to the perylene plane (80° of torsional angle). Its calculated ground state dipole moment is 5.98 Debye, lower than that of **PMI-DiPh**, due to the severe deviation from planarity.

With the exclusion of **PMI-DiBut** (dipole moment 8.14 Debye), which is a purely D-A compound, all other molecules can be described as a combination of the D-A and TW archetypes. In fact, all of them show a sizeable deviation from planarity, but at the same time, the variation in the ground state molecular dipole with the donor group (increasing in the order **PMI-DiBut**>**PMI-DiPh**>**PMI-DBA**>**PMI-Ind**>**PMI-Cbz**) indicates the presence of a D-A behavior.

This hypothesis is further strengthened by the fact that the reference compound, **PMI-Qs**, shows the lower ground dipole moment in the series. This is due to the fact that the quinoxaline derivative in *peri*

position is, in fact, weakly electron-withdrawing, therefore lowering the total dipole of the molecular ground state.

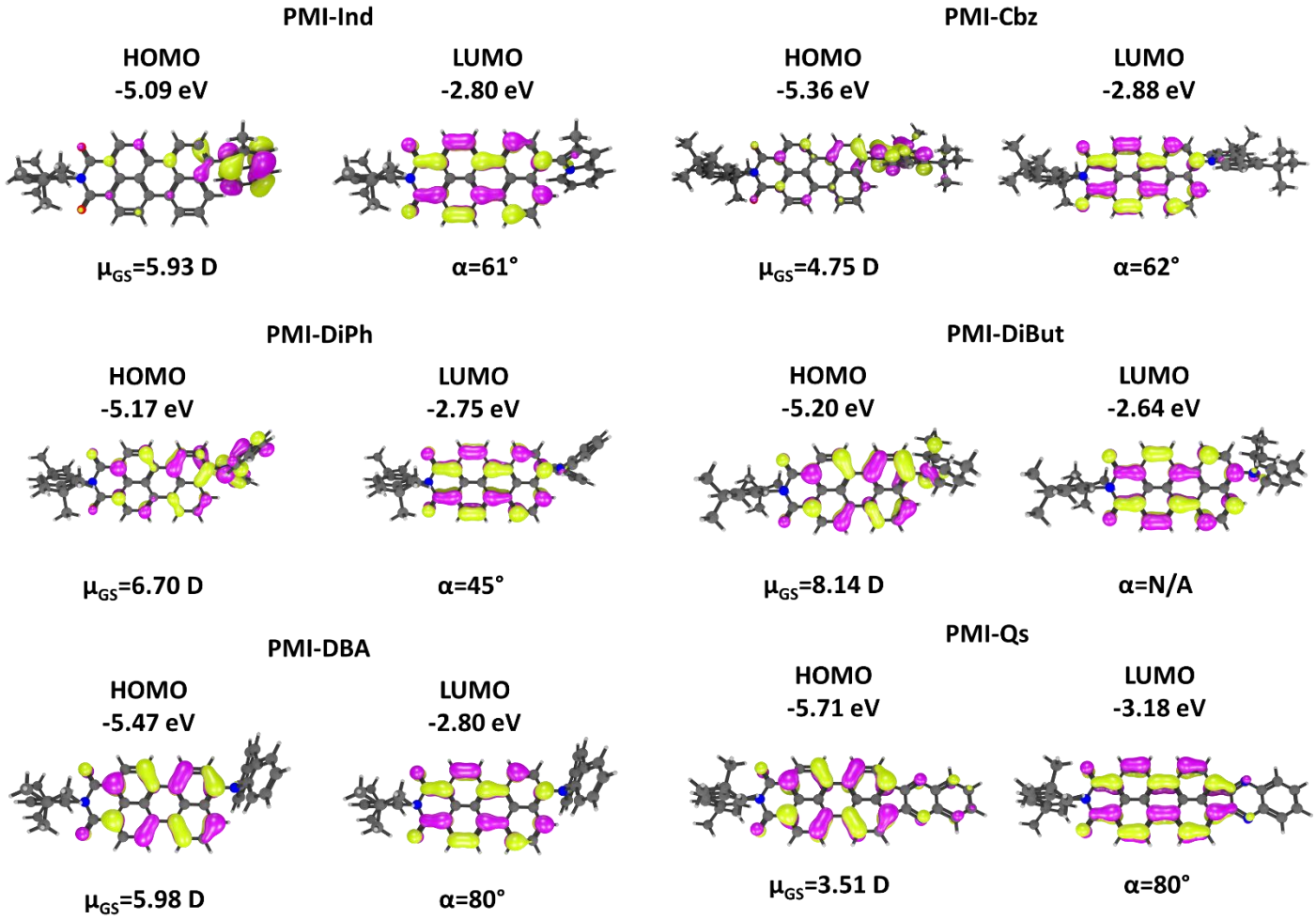

Figure 71: *calculated HOMO and LUMO energy levels, ground state geometries, molecular orbitals, ground state dipole moments and torsional angle of the nitrogen double pair with respect to the perylene core. The acceptor region of the molecule is on the left of the structures, the donors on the right.*

Electrochemical Characterization

The inspection of the differential pulse voltammetry (DPV) plots of a D-A compound family possessing the same acceptor and conjugated core enables to rank the donating capabilities of a donor series. In this study we used DPV instead of the more commonly employed cyclic voltammetry (CV) since some of our PMIs do not exhibit reversible oxidations.

DPV techniques provide higher resolution than normal CV scans, mainly thanks to the differential nature of the measurement and to their ability to remove capacitive background current[41]. A pulse of voltage is applied to the electrodes, and current is measured immediately before and after the voltage pulse. By plotting the difference in currents against the voltage one obtains peak-shaped curves. The area below

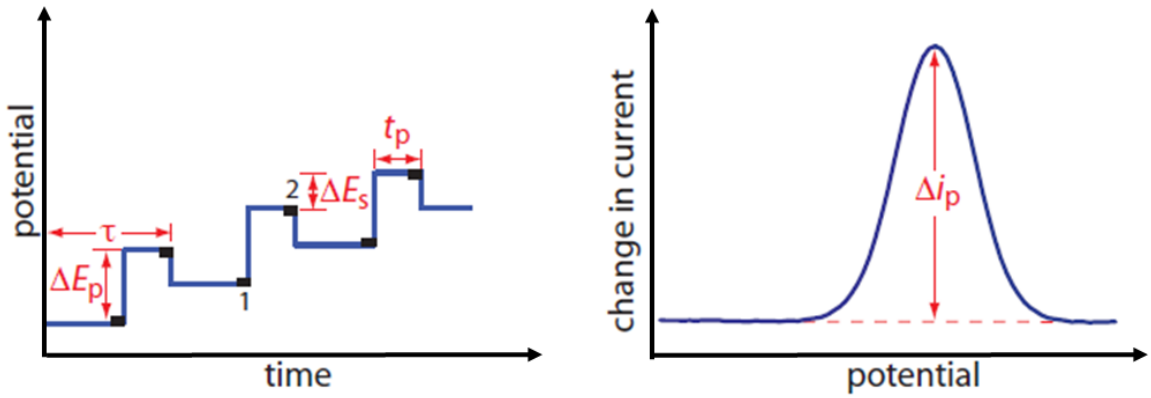

Figure 72: *experimental description of a DPV scan; (left) pulsed variation of the potential vs time: ΔE_P indicates the variation of potential during the pulse, ΔE_S the step variation between one pulse and the other, τ the total time between one pulse and the other and t_P the time duration of the voltage pulse; the black squares represent the time at which the current is measured; (right) output of the measurement with varying potential.*

the oxidation peak is equal to the one of the reduction only if the redox reaction is totally reversible. This technique is also useful for scantly soluble materials, as the threshold concentration is ~10^{-8} M.

Donating substituents are expected to increase the electrochemically-derived HOMO energy according to their specific strength. Furthermore, if the donor and the acceptor ends are efficiently coupled, an increasing donating strength should also increase the LUMO energy as the accepting end, where most likely the LUMO is localized, becomes harder to reduce.

Thus, when a particular donor mostly affects the HOMO energy without altering the LUMO, its coupling with the acceptor (and the extent of the π-conjugation) may be considered weak. The likely reasons for such behavior are excessive bridge conjugation length and/or the presence of a sizeable torsional angle between the donor and the acceptor (the acceptor being, at least in our case, forced to be coplanar with the bridge).

As such, the simultaneous inspection of both reduction and oxidation processes in a molecule series enables to rank the donor strength in terms of electron density effectively transferred toward the acceptor.

DPV plots show that **PMI-Ind**, the only compound exhibiting poor air stability, features the lowest oxidation potential and HOMO in this series (+0.25 V/-5.48 eV), with those of **PMI-Cbz** (+0.79 V/-6.02 eV), **PMI-DiPh** (+0.52 V/-5.75 eV), and **PMI-DiBut** (+0.29 V/-5.52 eV) located at higher potentials.

Under the electrochemical point of view, indolizine is the strongest donor. Among the nitrogen lone pair-based donors, the **PMI-DiBut** is the strongest one followed by **PMI-DiPh** and next by **PMI-Cbz**. Interestingly, the use of dibenzoazepine, a supposedly very strong donor, leads to an electrochemical HOMO (-5.59 eV) intermediate between those of **PMI-DiPh** and **PMI-DiBut**. This result can be rationalized by the peculiar geometry of **PMI-DBA**.

First of all, the dibenzoazepine residue is bent, according to reported crystal structure. As discussed previously, this bending prevents the dibenzoazepine from showing antiaromatic character and consequently strong donor behavior. Moreover, the dibenzazepine moiety is severely twisted, thus reducing its donating capability. Dibutylamine remains the stronger nitrogen-based donor since its

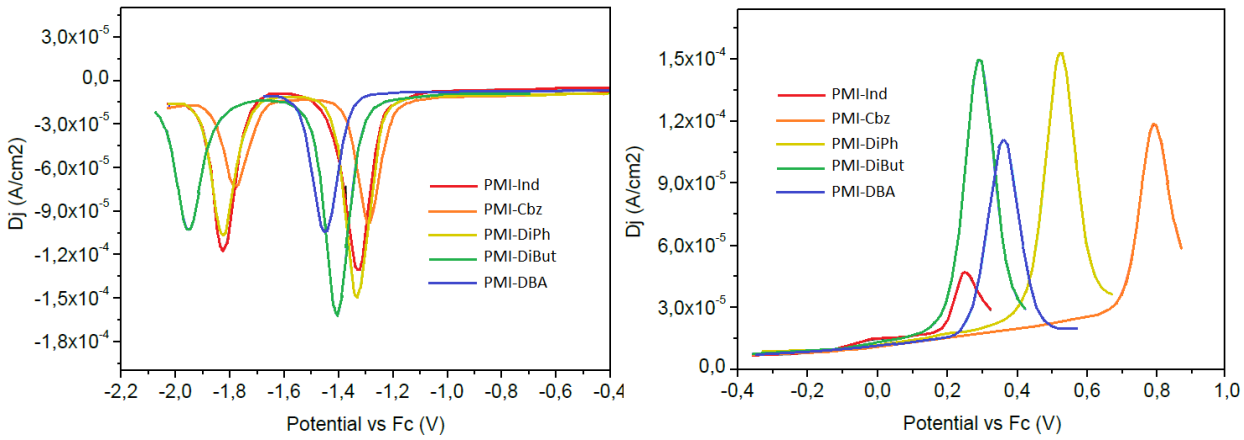

Figure 73: *DPV scans of the 5 investigated compounds. Their potentials are reported against the ferrocene/ferrocenium oxidation. (left) reduction plots; (right) oxidation plots.*

nitrogen lone pair can be fully delocalized over the perylene bridge, since it's not being shared by any other conjugated residue. The electrochemical LUMO levels (Table 2) show the same trend of the corresponding HOMOs, even though the differences in the corresponding energies are less pronounced.

Most of the HOMO and LUMO energy data available in the literature for D-A compounds are estimated from solution electrochemistry and/or a combination of solution electrochemistry and UV-Vis spectroscopy.

It is worthwhile noting that DPV is not a direct vertical ionization technique, and therefore solvent stabilization of charged species and reorganizational energies of the ionic compounds always impact the electrochemically-derived HOMO and LUMO levels. Since most of literature data is obtained through solution techniques, we thought worthy of investigation an analysis of their energetic levels in vacuum.

Thus, in parallel with electrochemical techniques we also employed Ultraviolet Photoelectron Spectroscopy, UPS, and compared the results to the data from DPV.

Ultraviolet Photoemission Spectroscopy

UPS is a vertical ionization spectroscopy, which is carried out on solid thin films under ultra-high vacuum (~10^{-8} mbar) using the He I emission line (21.22 eV) generated from a discharge lamp.

These measurements are therefore solvent independent. We included in the experiment the strongly electron-deficient derivative **PMI-Qs**, which was previously used for luminescent solar concentrators. **Figure 74** shows the high-binding energy cutoff region of the normalized photoemission spectra under a -9V bias for the whole range of compounds, barring **PMI-DiBut**.

The figure inset shows the full photoemission spectra. The ionization potential of all solids equals to the difference between the high-binding (low kinetic) cut-off energies and the low-binding (high-kinetic) Fermi edge onsets. **Figure 74** also shows the low-binding energy cutoff region highlighting the difference in the first ionization shoulder (*vide infra*).

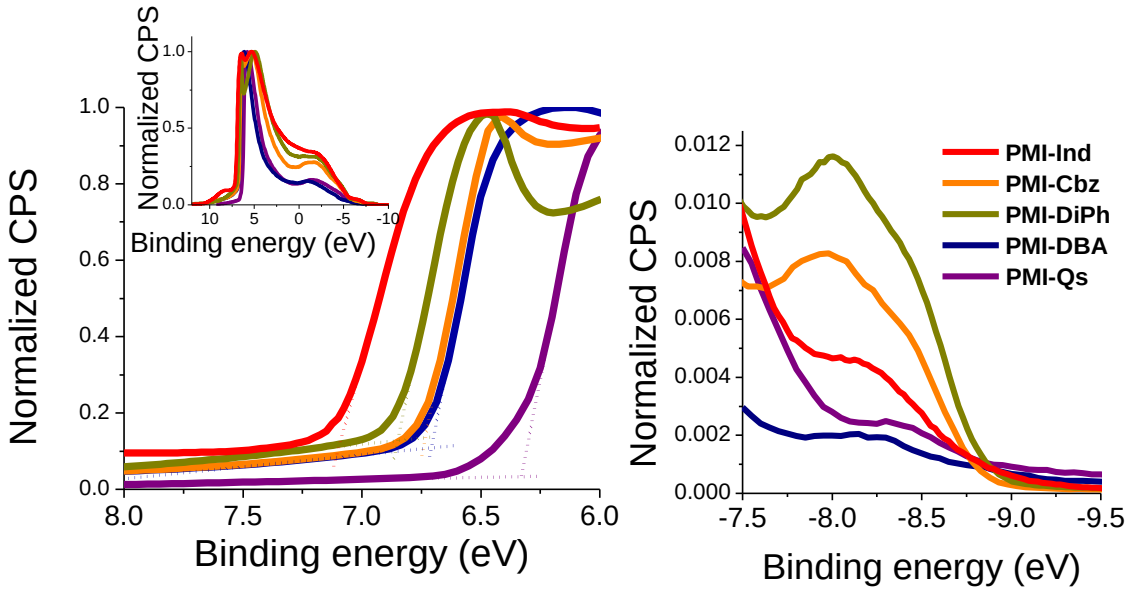

Figure 74: *Normalized photoemission spectra under a -9V bias for our series of PMI compounds; (left) high-binding energy cutoff region. The onset for all of the spectra has been moved to -8.92 eV in order to evidence the arising difference in ionization potentials. Inset: full photoemission spectra; (right) low-binding energy cutoff region highlighting the difference in the first ionization shoulder.*

The deviations between DPV and UPS datasets are ascribed to solvent/aggregation effects associated to the DPV experiments. However, in our case, the UPS and DPV datasets are almost superimposable for **PMI-DBA**. Moreover, UPS data report the same HOMO energy levels for **PMI-DBA** and **PMI-Cbz**.

Additionally, if we examine the low-binding energy region of the UPS spectra one can notice that while indolinzine-, carbazole- and diphenyl-functionalized PMIs show a shoulder attributed to the first ionization process, both **PMI-Qs** and **PMI-DBA** show a weaker signal.

While the lack of a peak is expected for the former – an all acceptor compound – this result is unexpected for the latter. As observed previously, though, the molecule is so severely twisted that D-A charge transfer becomes strongly impaired. In the solid state derivatives **PMI-Cbz** and **PMI-DBA** share the same deep HOMO level (-5.60 eV), closer to that of the all-acceptor derivative **PMI-Qs** (-5.95 eV).

Conversely, the DPV data place derivative **PMI-DBA** HOMO energy well above those of derivatives **PMI-Cbz** and **PMI-DiPh**. This inconsistency questions the real charge transfer nature of the HOMO-LUMO transition of **PMI-DBA**. Indeed the inspection of its orbital densities in the gas phase suggests a marginal role of the donor group in both the ground and the first excited state electron densities. Such conflicting data can be explained by taking onto account a likely different geometry of the compound in solution with respect to both the solid state and the gas phases.

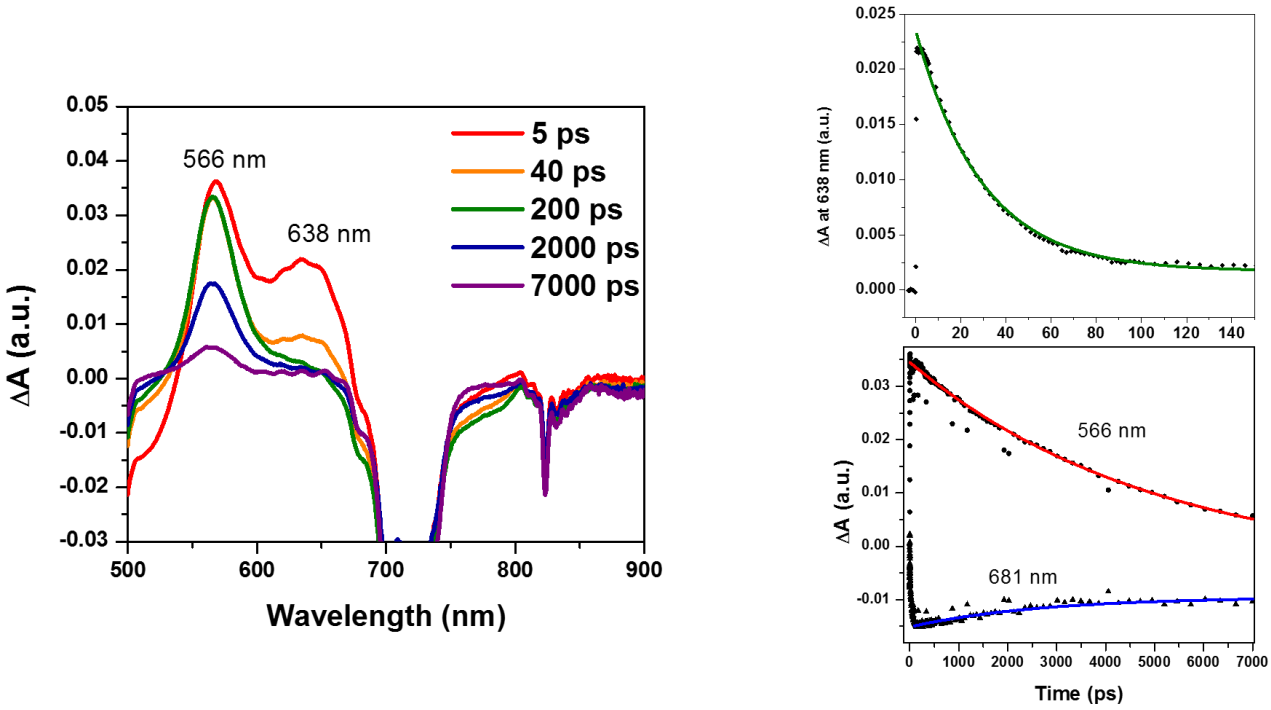

***Figure 75**: (left) differential transient absorption spectra of **PMI-DBA** (1.5 × 10^{-5} M) for 7 to 7000 ps after laser pulse irradiation at 480 nm in deaerated dichloromethane at 298 K; (right) time decay of the 638 nm (green), 566 nm (red) and 681 nm (blue) peaks in the transient absorption experiment.*

Transient Absorption

To better characterize the nature of **PMI-DBA** HOMO-LUMO transition in solution, we carried out time-resolved transient absorption experiments in deaereated dichloromethane at room temperature and we compared the results with a spectroelectrochemical analysis in the same solvent.

A transient absorption measurement is a technique used to determine the destiny of electrons on the nanosecond scale after they have been excited by a photon of the appropriate wavelength. The presence of two different lasers (one used to excite the molecule at a certain wavelength, pump, and the other to measure how the absorption of the dye changes once it has been excited, probe) and the change in the shape of the ground state absorption allow to determine which energy levels become depleted and at what rate the excited states decay.

The transient spectra of **PMI-DBA** in the 500-700 nm region show intense absorption bands at 566 and 638 nm. These spectra correspond to the sum of the reduced (radical anion) and oxidized (radical cation) forms, as obtained by a spectroelectrochemical experiment (**Figure 76**). Bleaches (i.e. negative ΔA) at λ < 520 nm and λ > 700 nm are due to ground state depletion and stimulated emission, respectively.

The decay time of the absorption bands at 566 and 638 nm is in the order of a few nanoseconds. The absorption band at 638 nm decays with a first-order rate constant of 3.7 × 10^{10} s^{-1} (**Figure 75**), while the change in the absorption at 566 nm occurs in two steps with first-order rate constants of 3.7 × 10^{10} s^{-1} and 2.3 × 10^{8} s^{-1}.

The initial fast process may be attributed to a conformational change of the molecular excited state, **PMI-DBA***, (e.g. increased planarity and sp^3->pseudo-sp^2 geometry of the linking dibenzoazepine nitrogen). A direct excitation of the dibenzoazepine moiety and the consequent energy transfer from (PMI-

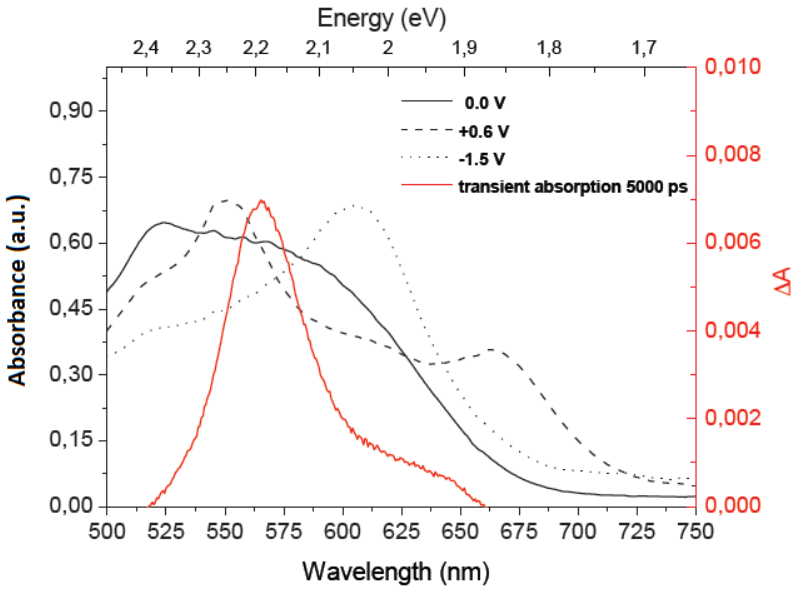

Figure 76: *Comparison between the transient absorption spectrum at 5000 ps of a dichloromethane solution of* ***PMI-DBA*** *and the corresponding absorption spectra of a CH_3CN solution of the same compound at no applied bias (solid line), -1.5 V (dotted line) and + 0.6 V (dashed line). Potentials are reported versus the Fc/Fc+ redox couple.*

^{1}dibenzoazepine*) to (^{1}PMI*- dibenzoazepine) should be excluded because the dibenzoazepine moiety does not absorb in the 480 nm region (i.e. excitation wavelength).

Afterwards the signal decays according to a charge-transfer process from the dibenzoazepine donor to the PMI acceptor, in agreement with a D-A behavior. These spectra correspond to the sum of the reduced (radical anion) and oxidized (radical cation) forms of the molecule as obtained by a spectroelectrochemical experiment. The rate constant of the charge transfer process (2.3×10^8 s–1; 4.3 ns) is consistent with the fluorescence lifetime of analogous PMI derivatives (~3 ns).

Multinuclear NMR investigation

Table 7: ppm for positions 5,6,7,8 in the range of PMIs.

Compound	5 - ^{1}H (ppm)	5 - ^{13}C (ppm)	6 - ^{1}H (ppm)	6 - ^{13}C (ppm)	7 - ^{1}H (ppm)	7 - ^{13}C (ppm)	8 - ^{1}H (ppm)	8 - ^{13}C (ppm)	6b - ^{13}C (ppm)
PMI-Ind	8.69	132.90	8.52	121.32	8.61	124.62	7.73	131.48	130.26
PMI-Cbz	8.72	132.90	8.54	121.57	8.64	124.82	7.77	128.34	130.40
PMI-DiPh	8.65	132.82	8.39	121.73	8.45	125.57	7.41	128.26	127.64
PMI-DiBut	8.60	132.92	8.30	119.64	8.38	125.44	7.25	119.19	124.10
PMI-DBA	8.55	132.97	8.29	120.41	8.29	124.92	7.28	127.21	123.81

Multinuclear ^{1}H and ^{13}C NMR spectroscopies can be of further aid in characterizing the effective electron donating capabilities of our donors. In fact, the inspection of the chemical shift of selected positions across the perylene bridge provides qualitative information about the amount of charge that a given donor is "pushing" towards the acceptor. This effect is distinct and complementary to the HOMO energy change evidenced by electrochemical and UPS techniques.

NMR monitors an increase in the charge transfer character through the chemical shift variations of the perylene core. We consider positions 6 and 6b, as highlighted in **Scheme 3**, particularly meaningful for the

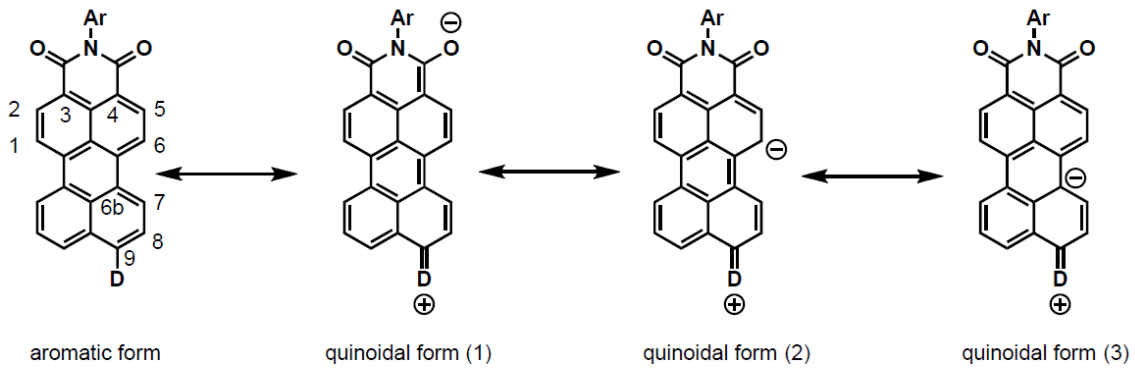

Scheme 12

determination of the donating character of the donor. In fact, according to the relative contribution of the aromatic versus quinoidal canonical description of the PMI ground state, the selected positions will show an upfield shift proportional to the donating strength of the employed donor.

Table 3 summarizes the ^{1}H and ^{13}C NMR data for positions 5,6,7,8 and 6b of the perylene core for the range of PMIs. The detailed inspection of all the data show the same trend, more or less pronounced, for all positions: an upfield shift of the ^{1}H and ^{13}C NMR signals in the order **PMI-DBA**>**PMI-DiBu**t>**PMI-DiPh**>**PMI-Ind**>**PMI-Cbz**. We will discuss in particular the data referring to the ^{13}C signals of positions 6b. This particular carbon is quaternary and unaffected by any possible parasitic through-space effect. Moreover, as is shown in the quinoidal form (3) of Scheme 2, one of the canonical representation of the general structure of our PMIs delocalizes in that position the charge residing on the Donor.

Thus, the ^{13}C signal of position 6b for **PMI-Cbz** (130.40 ppm) is essentially the same as the one corresponding signal for **PMI-Ind** (130.26 ppm). This result reflects again the inefficiency of indolizine to act as a π-Donor, even though such residue is strongly electron rich and easily oxidizable, as determined by DPV. The signal for **PMI-DiPh** (127.64 ppm) is sizably upfield shifted, according to the documented donating capabilities of aromatic amines. This is even truer for **PMI-DiBut** (124.10 ppm). Exactly as in the case of the electrochemical ranking of donating capability, the NMR data confirm that an alkyl amine is a stronger donor with respect to an aryl one.

Finally, derivative **PMI-DBA** shows the highest upfield shift in the series (123.81 ppm) confirming that, at least in solution, the dibenzoazepine residue is a stronger donor than a standard aromatic amine and is at least comparable with aliphatic amines. The inspection of both ^{1}H and ^{13}C signals of positions 6 and 8 shows the same trend, with the only exception of position 8 of derivative 4, upfield shifted with respect to the other compounds in the series. The deviation can be associated with the fact that this derivative is the only one featuring an alkyl substituent and thus unaffected by through space shielding effects that are instead affecting the position 8 of all other compounds.

Electronic UV-Vis characterization

Figure 77 shows the absorption (a) and emission (b) spectra of the materials in $CHCl_3$ and Table 4 summarizes all UV-Vis characterization data. Literature data shows that D-A PMIs are characterized by a broad and featureless absorption band peaking at 500-650 nm, sizeable Stokes shifts (3000-4000 cm^{-1}) and generally low emission efficiency (< 40%).

This holds true for **PMI-DiBut** and **PMI-DiPh**, with the latter outperforming the former in terms of Stokes Shift by 750 cm^{-1}. The absorption spectrum of **PMI-DBA** is also broad but with a distinguishable vibronic structure. The latter feature is connected with a less pronounced charge transfer behavior with respect to both dialkyl and diphenyl compounds, as corroborated by the lower Stokes shift (2560 cm^{-1}). In contrast to all other PMIs, **PMI-Cbz** possesses a vibrationally structured absorption and a broad and featureless emission.

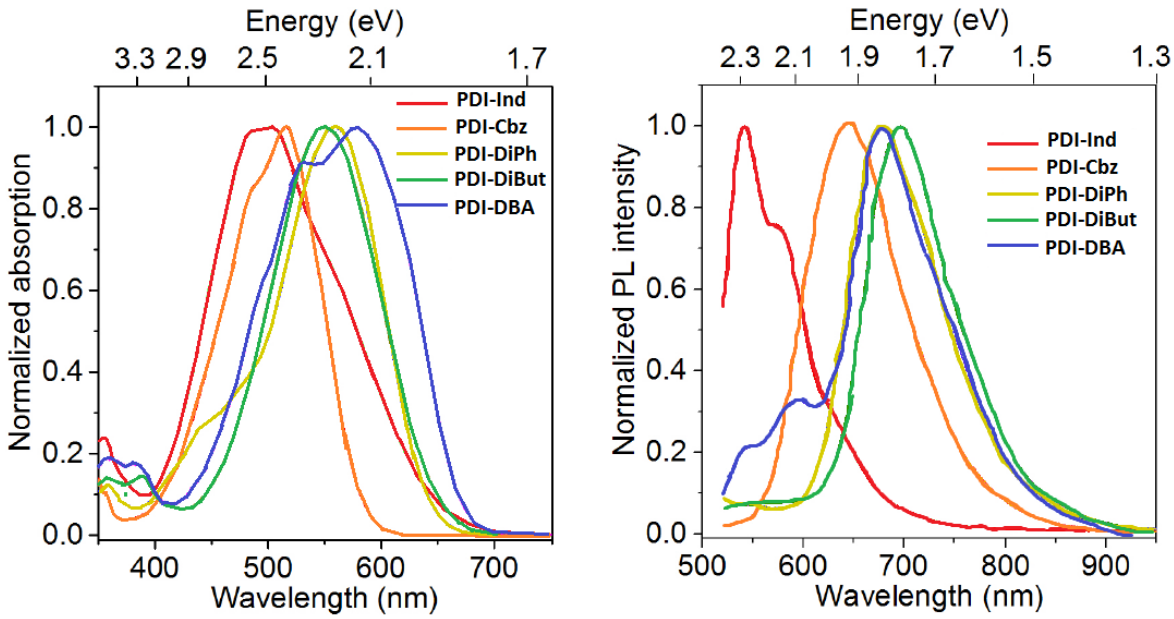

Figure 77: *(left) normalized absorption spectra of the compound series in chloroform; (right) normalized emission spectra of the series in chloroform.*

Also, its Stokes shift (3790 cm^{-1}) is nearly as large as that of **PMI-DiBut** (3814 cm^{-1}), even though carbazole hardly qualifies as a strong donor. Likewise, the carbazole derivatives is the only compound in the series behaving mostly as a TW derivative with very little D-A character. Upon optical excitation, this molecule undergoes a quinoidal distortion enforcing molecular planarity. The resulting major difference between the ground and first excited electronic states is responsible for the particularly large Stokes shift. Derivatives **PMI-Cbz** and **PMI-Ind** exhibit similar torsional features, with the notable difference that indolizine is a strong donor.

This has profound consequences in terms of optical properties and photostability. The close inspection of derivative 1 absorption spectrum shows that its band is made of two contributions, a high energy absorbing, vibrationally structured one peaking at 504 nm and a low energy absorbing shoulder around 570 nm. The Stokes shift is unusually small (1436 cm^{-1}).

We believe that the low energy component of **PMI-Ind**'s absorption corresponds to a through-space photoinduced charge transfer from the indolizine residue to the PMI core with consequent formation of an air unstable indolizine radical cation and a PMI radical anion. While the anion can be reversibly quenched by molecular oxygen, the radical cation undergoes irreversible degradation. Such mechanism is likely to apply for all electron-rich and strongly twisted substituent.

Analysis of the emission efficiencies is also particularly meaningful. First of all, **PMI-DiBut** is the only compound whose (low) emission efficiency does not change appreciably on going from toluene to chloroform solutions. This is essentially a D-A chromophore and thus it exhibits low emission efficiency (39 % and 33 % in toluene and $CHCl_3$ respectively) and a large Stokes Shift.

For all other compounds the emission efficiency is significantly higher in toluene (99, 95 and 73% for **PMI-Cbz**, **PMI-DiPh**, and **PMI-DBA** respectively) than in chloroform (43, 56 and 36% respectively). Indeed,

Table 8: optical characteristics of compound series

Compound	Abs λ_{MAX} (nm)	Em λ_{MAX} (nm)	Φ	ε (L mol^{-1} cm^{-1})	Stokes shift (cm^{-1})
PMI-Ind ($CHCl_3$)	502	541	0.05	25600	1436
PMI-Cbz ($CHCl_3$)	513	578	0.99	32000	2192
PMI-Cbz (toluene)	517	643	0.43	33000	3790
PMI-Cbz (PMMA)			0.93		
PMI-DiPh ($CHCl_3$)	550	629	0.95	31500	2284
PMI-DiPh (toluene)	560	676	0.56	31000	3064
PMI-DiPh(PMMA)	-	-	0.73	-	-
PMI-DiBut ($CHCl_3$)	530	654	0.39	28000	3577
PMI-DiBut (toluene)	550	696	0.33	29000	3814
PMI-DiBut (PMMA)	-	-	0.40	-	-
PMI-DBA ($CHCl_3$)	562	646	0.73	30000	2314
PMI-DBA (toluene)	577	677	0.36	29000	2560
PMI-DBA (PMMA)			0.70		

solvent polarity influences the interplay between D-A and TW regimes, as a polar solvent (chloroform) will enhance the former contribution, while a low polarity one (toluene) will do the opposite. Coherently, for all compounds possessing sizeable torsional angles (see Table 1) between the donor and the acceptor, low polarity solvents leads to higher luminescence quantum yields.

For the purpose of the proposed application, the data in PMMA are particularly meaningful. In this case the emission efficiency will depend on polarity, as in the case of solutions, but also on viscosity. In fact, molecules possessing two conjugated fragments connected by a single bond having restricted rotational freedom, frequently behave as “molecular rotors”.

The most distinctive characteristic of such class of compounds is an increase of the luminescence quantum yield upon increase of the local viscosity. With the sole exception of derivative **PMI-DiBut** (a further confirmation of the purely Donor Acceptor nature of this compound) all emission quantum yields in PMMA are systematically higher than the value in chloroform and generally comparable with those in toluene, even though the polarity of PMMA is even higher than that of chloroform.

The value is particularly high for **PMI-Cbz**, again not surprisingly, as this is almost a purely twisted compound and thus a very efficient molecular rotor. As this compound combines a very high Stokes Shift and the higher quantum yield in the series, we tested its performances as the luminophore in a LSC prototype. A 10^{-4} M solution in PMMA/MMA syrup of **PMI-Cbz** was heated in a cell cast immersed in a water bath at 56°C for 48 h. The cell cast was then annealed at 100°C for 12 h.

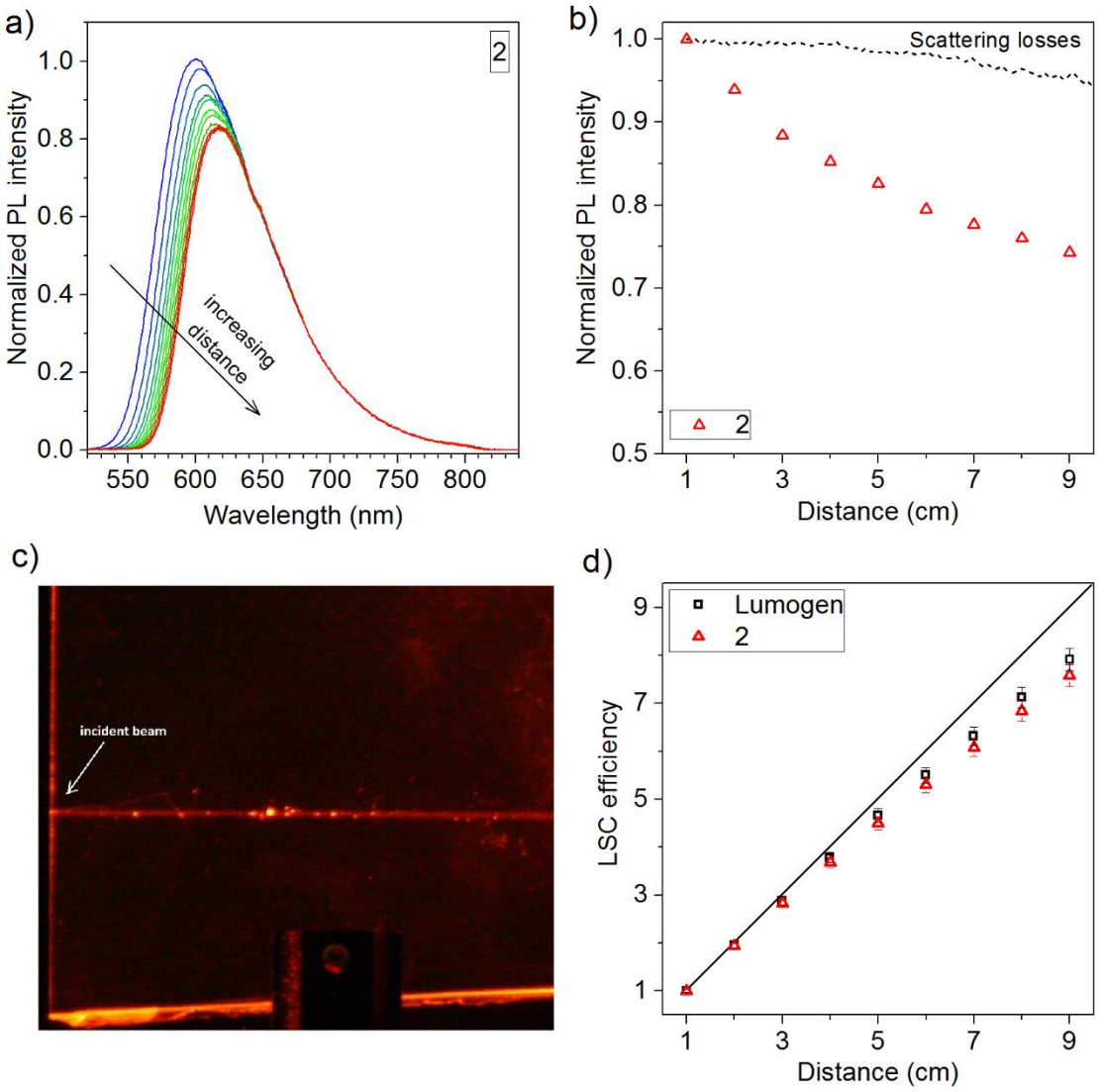

Figure 78: *(a) PL spectra excited at 405 nm at increasing distance (from 1 to 10 cm) between the excitation spot and detection at LSC edge for derivative 2; (b) Integrated PL output signal as a function of the distance from the excitation spot for derivatives 2. For comparison also the scattering losses, obtained from the diffusion of a laser beam at 820 nm travelling through a pure PMMA slab (c), is reported. (d) Total PL output for a linear growth of the slab size for a LSC based on the derivative 2 and for a reference LSC based on Lumogen f 240. The black-line indicates the "hypothetic" PL output increase for an ideal lossless sample.*

During the whole process the sample remained homogeneous, without showing any sign of chemical degradation. The slab was characterized in terms of the solid state quantum yield and re-absorption losses as a function of the distance between the excitation point and the slab edge where emitted light was collected. It is worthwhile to note that the carbazole derivative in PMMA matrix is almost as efficient (93%) as the reference Lumogen f240 orange dye (perylene-3,4,9,11-tetracarboxylic acid bis-(2',6'-diisopropylanilide), quantum yield 99 %).

Several processes including light scattering at the interfaces or inside the slab itself, and photoluminescence re-absorption affect the LSC efficiency. In order to isolate the optical losses due to the reabsorption, strictly related to the active dye efficiency, we plotted the evolution of the normalized

emission spectrum as a function of the distance between the detection at the LSC edge and the excitation spot (laser operating @ 405 nm).

The normalization was carried out on the low-energy tail of the spectrum (λ > 730 nm) where the re-absorption is negligible (**Figure 78a**). The PL spectrum shifts towards lower energies when increasing the distance, but the overall intensity is only slightly attenuated as clearly shown in **Figure 78b**. Thus, for an optical path of 10 cm the LSC based on the **PMI-Cbz** retains about 80% of its initial intensity. **Figure 78b** also reports the scattering losses obtained from the attenuation of a laser @ 820 nm (photon energy below the band gap) traveling through the slab (**Figure 78c**). The scattering contribution is generally very small and constant throughout the sample, a further evidence that any further improvement of LSC performances will mostly depend on the optimization of the luminophore properties in terms of Stokes shift and luminescence quantum yield.

Our findings demonstrate that derivative 2 represents an optimal trade off as it shows both a very large Stokes shift and a high emission quantum yield. This compound represents a significant entry in the field of luminescent materials for LSC and is a valid alternative to the traditional Lumogen dyes for the fabrication of larger area devices. Indeed, **Figure 78d** compares the estimated total PL output as a function of the LSC size for slabs doped with **PMI-Cbz** and with Lumogen f 240 red.

As expected, the tendency of the total emitted light to saturate by increasing the device dimensions is rather small for both LSC devices, whose performances are indistinguishable within the experimental uncertainty. **PMI-Cbz** however features advantages with respect to Lumogen Orange f 240 as its emission spectrum is better matched with high efficiency cells typically employed for concentration devices.

EXPERIMENTAL

Synthesis

Synthesis of **2**

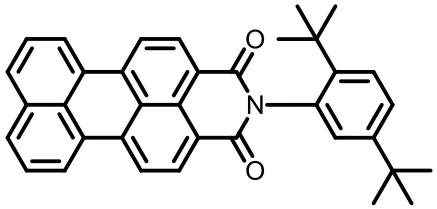

A mixture of Compound **1** (21.96 g, 60.0 mmol), 2,5-di-tertbutylaniline (6.98 g, 34.0 mmol), $Zn(OAc)_2.2H2O$ (2.41 g, 11.0 mmol), imidazole (127 g, 1.86 mol) and water (72 mL) were placed in an autoclave equipped with a pressure gauge. The mixture was stirred at 190 °C, causing a gradual increase in pressure. After 20 h, the pressure gauge showed 15 bar and the reaction mixture was cooled to RT. The mixture was diluted with $CHCl_3$ (1 L), then filtered through celite to remove any insoluble impurities. The filtrate was washed with water (3 × 50 mL), dried on $MgSO_4$ and evaporated under reduced pressure to afford a bright red solid. The crude was dissolved in toluene (4 mL) and purified by column chromatography on silica with gradient elution of increasing portions of CH_2Cl_2 in toluene.

The relevant fractions were collected and the solvent evaporated to give a bright orange solid. The crude was triturated in AcOEt and the insoluble material was collected to yield the product as a bright orange crystalline solid (yield 33%).

^{1}H-NMR ($CDCl_3$ @ 500 MHz): δ 8.59, d, 2H; δ 8.38, d, 4H; δ 8.36, d, 2H; δ 7.87, d, 2H; δ 7.61 ,d, 1H; δ 7.58, d, 2H; δ 7.46, dd, 1H; δ 7.04, d, 1H; δ 1.35, s, 9H; δ 1.31, s, 9H.

^{13}C NMR ($CDCl_3$ @ 126 MHz): δ 165.1, 150.1, 143.9, 137.5, 134.4, 133.2, 132.0, 131.0, 130.4, 129.3, 128.9, 128.0, 127.2, 126.3, 123.9, 121.4, 120.3, 35.8, 34.7, 31.9, 31.4.

Synthesis of **3**

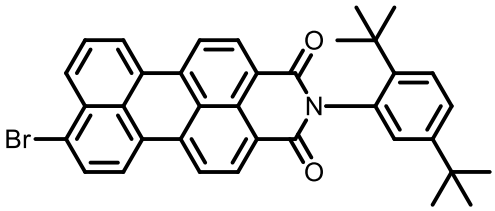

A mixture of compound **2** (2.50 g, 4.91 mmol) and potassium carbonate (2.45 g, 17.7 mmol) in chlorobenzene (50 mL) was heated to 40 °C and then treated rapidly with a solution of bromine (0.58 mL, 1.81 g, 22.6 mmol) in chlorobenzene (10 mL). The mixture is stirred for 2.5 h at 60°C. The solvent is evaporated at reduced pressure and the crude diluted in EtOAc (100 mL). The precipitate is collected, washed with cold EtOAc (100 mL), then recrystallized from EtOH to yield the product as a red solid (yield 91%).

^{1}H-NMR ($CDCl_3$ @ 500 MHz): δ 8.63, d, 1H; δ 8.61, d, 1H; δ 8.40, d, 1H; δ 8.38, d, 1H; δ 8.33, d, 1H; δ 8.25, d, 1H; δ 8.14 (d, 1H; δ 7.84, d, 1H; δ 7.67, dd, 1H; δ 7.60, d, 1H; δ 7.46, dd, 1H; δ 7.05, d, 1H; δ 1.34, s, 9H; δ 1.31, s, 9H.

^{13}C NMR ($CDCl_3$ @ 126 MHz): δ 164.9, 150.2, 143.92, 136.8, 136.7, 133.1, 133.0, 132.1, 131.3, 130.2, 129.2, 128.9, 128.0, 126.7, 126.3, 124.5, 123.8, 121.8, 120.8, 120.5, 35.7, 34.4, 31.9, 31.4.

Synthesis of **PMI-Ind**

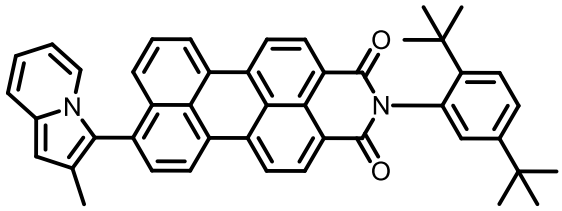

Compound **3** (600 mg, 1.019 mmol), Palladium(II) acetate (3.00 mg, 13.36 µmol), pivalic acid (33 mg, 0.323 mmol), potassium carbonate (211 mg, 1.529 mmol), tricyclohexylphosphine tetrafluoroborate (7.80 mg, 21.18 µmol) and 2-methylindolizine (147 mg, 1.121 mmol) are loaded in a screw-capped tube under Argon atmosphere. The mixture is suspended in anhydrous DMAc (3.5 mL) and then stirred at 100 °C for 44 h. The mixture is poured into water (100 mL) to give a solid precipitate that is isolated by filtration and purified by column chromatography (silica, CH2Cl2/Toluene 10:1) to give the title compound as a purple solid (yield 61%).

^{1}H-NMR ($CDCl_3$ @ 500 MHz): δ 8.70, d, 1H; δ 8.69, d, 1H; δ 8.61, d, 1H; 8.54-8.51, m, 3H; δ 7.73, d, 1H; δ 7.61-7.50, m, 4H; δ 7.46, dd, 1H; δ 7.42, d, 1H; δ 7.04, bs, 1; δ 6.72, t, 1H; δ 6.54, bs, 1H; δ 6.40-6.36, m, 1H; 2.27-2.25, m, 3H; δ 1.34, s, 9H; δ 1.32, s, 9H.

^{13}C NMR ($CDCl_3$ @ 126 MHz): δ 165.8, 150.9, 144.6, 138.4, 138.2, 134.4, 134.0, 133.9, 133.4, 132.9, 131.5, 131.4, 131.2, 130.7, 130.2, 130.1, 130.0, 128.7, 128.4, 127.8, 127.0, 126.1, 124.9, 124.6, 124.0, 122.3, 121.3, 121.2, 120.6, 119.3, 118.2, 110.9, 101.8, 36.4, 35.1, 32.6, 32.1, 13.3.

General procedure for Buchwald-Hartwig aminations between **3** and **amines of interest**

Compound **3** (600 mg, 1.019 mmol), sodium tert-butoxide (141 mg, 1.470 mg) and the corresponding amine (1.0 eq), are loaded in a 100 mL two-neck round bottom flask equipped with a condenser under N2 atmosphere. The mixture is suspended in anhydrous toluene (30 mL) and degassed with few vacuum/N2 cycles. In a 25 mL two-neck round bottom flask, the catalyst is prepared: Pd(dba)2 (30 mg, 0.051 mmol) is suspended in anhydrous toluene (5 mL) and P(tBu)3 (solution 1M in toluene) (0.12 mL, 0.102 mmol) is added.

The mixture is left under stirring 15 min and then it is transferred into the reaction flask by standard cannula technique. The final reaction mixture is reacted under microwave irradiation in nitrogen atmosphere. After the reported reaction time, the solvent is removed from the mixture and the crude solid is purified by column chromatography.

Synthesis of **PMI-Cbz**

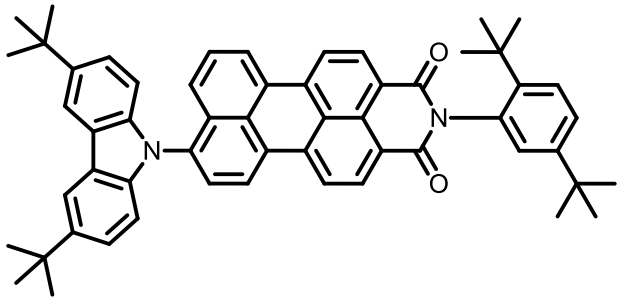

The dark crude solid is purified by column chromatography (silica, toluene/CH2Cl2 1:8) to give the product as a red solid (yield 41%).

^{1}H-NMR ($CDCl_3$ @ 500 MHz): δ 8.72, d, 1H; δ 8.71, d, 1H; δ 8.64, d, 1H; δ 8.57, d, 1H; δ 8.55-8.53, m, 1H; δ 8.23, d, 2H; δ 7.77, d, 1H; δ 7.61, d, 1H; δ 7.61-7.51, m, 3H; δ 7.47, dd, 1H; δ 7.45-7.42, m, 2H; δ 7.05-7.02, m, 3H; δ 1.49, s, 18H; δ 1.34, s, 9H; δ 1.33, s, 9H.

^{13}C NMR ($CDCl_3$ @ 126 MHz): δ 165.8, 150.9, 144.7, 144.1, 141.3, 138.2, 138.1, 137.8, 133.9, 132.9, 132.8, 132.7, 131.2, 130.8, 130.4, 130.3, 129.6, 128.7, 128.6, 128.3, 127.9, 127.8, 127.0, 125.3, 124.8, 124.7, 124.5, 122.6, 121.6, 121.5, 117.3, 110.4, 36.4, 35.7, 35.1, 32.9, 32.6, 32.1.

Synthesis of **PMI-DiPh**

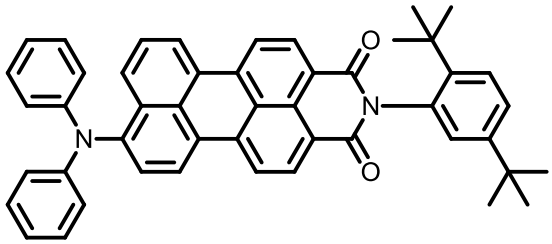

The crude purple solid residue is purified by column chromatography (silica, toluene/AcOEt 9:1) to afford the product as a violet solid (yield 70%).

^{1}H-NMR ($CDCl_3$ @ 500 MHz): δ 8.66, d, 1H; δ 8.65, d, 1H; δ 8.48, d, 2H; δ 8.45, d, 1H; δ 8.39, d, 1H; δ 8.05, d, 1H; δ 7.59, d, 1H; δ 7.49, t, 1H; δ 7.45, dd, 1H; δ 7.41, d, 1H; δ 7.28-7.25, m, 4H; δ 7.10, d, 4H; δ 7.05-7.02, m, 3H; δ 1.33, s, 9H; δ 1.31, s, 9H.

^{13}C NMR ($CDCl_3$ @ 126 MHz): δ 165.9, 150.8, 149.2, 147.9, 144.7, 138.4, 138.3, 134.0, 132.9, 132.8, 132.2, 131.2, 130.7, 130.3, 129.7, 128.7, 128.5, 128.3, 128.0, 127.6, 127.5, 127.0, 125.6, 125.0, 123.8, 123.7, 122.2, 121.7, 121.1, 120.8, 36.4, 35.1, 32.6, 32.1.

Synthesis of **PMI-DiBut**

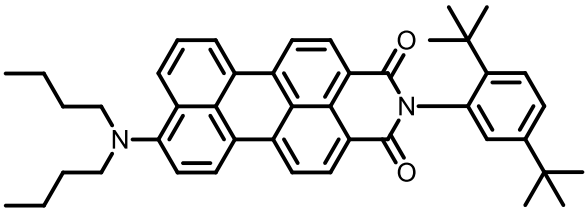

The dark-purple solid residue is purified by column chromatography (silica, AcOEt/petroleum ether 2:8) to give the title compound as a purple solid (yield 46%).

^{1}H-NMR ($CDCl_3$ @ 500 MHz): δ 8.64, d, 1H; δ 8.62, d, 1H; δ 8.50, d, 1H; δ 8.42, t, 2H; δ 8.34, t, 2H; δ 7.63, t, 1H; δ 7.59, d, 1H; δ 7.44, dd; δ 7.6, d, 1H; δ 7.02, d, 1H; δ 3.30, t, 4H; δ 1.61-1.55, m, 4H; δ 1.33, s, 9H; δ 1.30, s, 9H; δ 0.89, t, 6H.

^{13}C NMR ($CDCl_3$ @ 126 MHz): δ 166.0, 165.9, 153.3, 150.8, 144.7, 139.1, 138.9, 134.2, 132.9, 132.7, 131.4, 131.3, 130.4, 130.3, 129.5, 128.8, 128.5, 127.5, 126.9, 126.8, 125.4, 125.0, 124.1, 121.8, 120.6, 120.5, 119.7, 119.2, 54.5, 36.4, 35.1, 32.6, 32.1, 30.2, 21.3, 14.8.

Synthesis of **PMI-DBA**

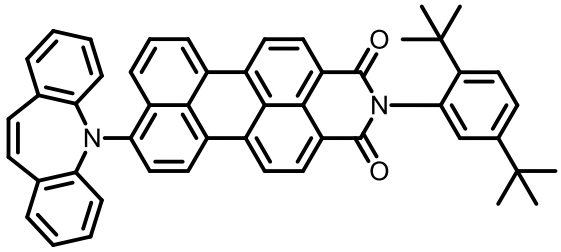

Solvent was removed and the dark residue was taken up with 100 ml of CH2Cl2 and filtered through a plug of silica gel. The dark purple solution was evaporated to dryness to give a solid residue. Trituration in isopropanol (30 ml) gave the pure title compound as a purple powder (yield 75%).

^{1}H-NMR ($CDCl_3$ @ 500 MHz): δ 8.57, d, 1H; δ 8.55, d, 1H; δ 8.30, s, 1H; δ 8.28, t, 1H; δ 8.23, d, 1H; δ 8.17, d, 1H; δ 7.87, d, 1H; δ 7.59, d, 1H; δ 7.52, d, 1H; δ 7.45-7.38, m, 5H; δ 7.29, d, 2H; δ 7.28, t, 1H; δ 7.22, t, 1H; δ 7.02, d, 1H; δ 7.00, s, 1H; δ 1.33, s, 9H; δ 1.30, s, 9H.

^{13}C NMR ($CDCl_3$ @ 126 MHz): δ 165.9, 150.8, 147.7, 146.8, 144.6, 139.0, 138.9, 136.2, 134.2, 133.0, 132.6, 132.4, 131.4, 131.0, 130.8, 130.6, 130.0, 129.5, 129.2, 128.7, 128.2, 128.0, 127.3, 127.2, 126.9, 126.2, 125.5, 124.9, 123.8, 121.6, 120.4, 120.3, 119.4, 119.4, 36.4, 35.10, 32.6, 32.1.

Computational Investigation

All DFT calculations were performed using the Q-Chem software suite. Initial geometry optimizations were performed using the empirical EDF1 functional and 6-31G** basis set, followed by optimization at the hybrid level with B3LYP paired with a 6-31G** basis set. This protocol was followed for both neutral and cationic electronic configurations. The reported ground state dipole moments, HOMO and LUMO Kohn-

Sham orbitals and eigenvalues were obtained from singlepoint B3LYP/6-31G** calculations on the optimized neutral geometries.

Electrochemical Characterization

For the electrochemical characterization all perylene derivatives were dissolved (concentration in the order of 10^{-4} M) in the supporting electrolyte that was a 0.1 M solution of tetrabutylammonium perchlorate (Fluka, electrochemical grade, ≥99.0%) in a solution of anhydrous acetonitrile (Aldrich, 99.8%) and dichloromethane (Aldrich, 99.8%), 2:1 by volume. Cyclic Voltammetries at scan rate of 50 mV/s were carried out using a PARSTA2273 potentiostat in a single chamber three electrodes electrochemical cell in a glove box filled with Argon ([O2] ≤ 1 ppm). The working, counter and pseudo-reference electrodes were a Glassy Carbon (GC) pin (3mm diameter), a Pt flag, and a Ag/AgCl wire, respectively. The GC surface was polished with alumina 0.1 µm suspension, sonicated for 15 min. in deionized water and washed with 2-propanol before using. The Ag/AgCl pseudo-reference electrode was calibrated before and after each measurement using a 1 mM ferrocene solution in the electrolyte.

UPS Characterization

Glass slides (2.5 cm x 1.5 cm) were subsequently cleaned by sonication at 50° C in soapy water, deionized water, isopropanol, ethanol and acetone, then treated in an ozone plasma (residual pressure 400-500 mmHg) for 10 minutes to remove organic residues. After each of the following cleaning and processing steps the slides were flushed with dry 200 nm dust-filtered nitrogen The substrates were then transferred in a nitrogen-filled glove box and 100 nm of silver (Silver slugs Premion 99.999% from Alfa-Aesar) were evaporated at a 0.2 Å/s rate. The various solutions (5 x 10-3 M in anhydrous DCM) were spun-cast at 1500 rpm for 30 seconds. The materials were glued to a sample holder with copper tape, transferred in Desivac and moved to the prechamber of a Thermo Scientific ESCALAB 250Xi. After overnight pumping the substrates were moved to the main chamber and UPS scans measured (base pressure 2 x 10-8 atm, using He-I emission line at 21.22 eV while under -9 V bias). The spectra were collected and processed using Thermo Scientific Avantage 5.35.

Spectroelectrochemical Characterization

For the spectroelectrochemical (SE) characterization perylene derivatives were dissolved (concentration in the order of 10^{-4} M) in the supporting electrolyte that was a 0.1 M solution of tetrabutylammonium perchlorate (Fluka, electrochemical grade, 99.0%) in a solution of anhydrous acetonitrile (Aldrich, 99.8%) and dichloromethane (Aldrich, 99.8%), 2:1 by volume. Potentiostatic pulse were applied using a PARSTA2273 potentiostat with a single chamber three electrodes SE optical cuvette in a glove box filled with Nitrogen ([O2, H2O] < 0.1 ppm). The working, counter and pseudo-reference electrodes were a gold mesh ($1cm^2$), a Pt wire and a Ag/AgCl wire, respectively. The Ag/AgCl pseudo-reference electrode was calibrated before and after each measurement using a 1 mM ferrocene solution in the electrolyte. Optical SE cuvette has an optical path of 1mm. Spectra are taken using an Als Co. SEC2000 spectrophotometer. All the spectra are taken after the applications of a potential bias for a time long enough, minimum 30s, to reach the optical equilibrium state for that applied potential.

Transient Absorption

Femtosecond transient absorption spectroscopy experiments were conducted using a regeneratively amplified Ti:sapphire laser system and an optical detection system (Spectra-Physics), which produces the

source for the pump and probe pulses from the fundamental output: 1 kHz pulse train centered at 827 nm with 1 mJ/pulse. The pump beam was attenuated at around 1 μJ/pulse with a spot size of 0.1 mm diameter at the sample cell, where it was merged with the white probe pulse. The probe beam after passing through the 2 mm sample cell was focused on a fiber optic cable which was connected to a CCD spectrograph.

Kinetic traces at appropriate wavelengths were assembled from the time-resolved spectral data. The excitation of the samples was performed with the excitation pulse at 480 nm. All measurements were recorded at 298 K.

LSC preparation

In a typical procedure, 100 mg of AIBN were dissolved in 100 ml of freshly distilled MMA. The solution was placed in a beaker and slowly heated on a hot plate until the temperature of 80 °C was reached. This temperature was maintained for 5 minutes, during which time viscosity increased substantially. The solution was immediately transferred in an ice bath and cooled at 20°C. A solution of the appropriate perylen dye in freshly distilled MMA (60 ml) was added along with 15 mg of lauryl peroxide. The viscous syrup thus obtained was poured in a mold of 7 mm thickness and 100 cm^2 area and heated in a water bath at 56°C for 48 h. At the end of this thermal treatment the syrup turns into a solid slab that is further cured at 95°C for 24 h. After cooling, the slab can be easily separated by the glass mould and polished for optical measurements.

BIBLIOGRAPHY

1. Shelby, R. A., Smith, D. R. & Schultz, S. Experimental verification of a negative index of refraction. *Science* **292,** 77–9 (2001).

2. Schuster, S. A. *An introduction to the theory of optics*. 340 (E. Arnold, 1904). at <http://books.google.com/books?vid=OCLC03146755&pgis=1>

3. Goldschmidt, J. C. *et al.* Increasing the efficiency of fluorescent concentrator systems. *Sol. Energy Mater. Sol. Cells* **93,** 176–182 (2009).

4. Lakhtakia, A. Would Brewster recognize today's Brewster angle? *Opt. News* **15,** 14 (1989).

5. Gispert, J. R. *Coordination Chemistry*. 600 (Wiley, 2008). at <http://books.google.com/books?id=9d893122U6kC&pgis=1>

6. Goetzberger, A. & Wittwer, V. Fluorescent planar collector-concentrators: A review. *Sol. Cells* **4,** 3–23 (1981).

7. Born, M. & Wolf, E. *Principles of Optics: Electromagnetic Theory of Propagation, Interference and Diffraction of Light*. 986 (CUP Archive, 2000). at <http://books.google.com/books?id=oV80AAAAIAAJ&pgis=1>

8. Keil, G. Design principles of fluorescence radiation converters. *Nucl. Instruments Methods* **89,** 111–123 (1970).

9. Goetzberger, A. & Greube, W. Solar energy conversion with fluorescent collectors. *Appl. Phys.* **14,** 123–139 (1977).

10. Thomas, W. R. L., Drake, J. M. & Lesiecki, M. L. Light transport in planar luminescent solar concentrators: the role of matrix losses. *Appl. Opt.* **22,** 3440 (1983).

11. Bakr, N. A., Mansour, A. F. & Hammam, M. Optical and thermal spectroscopic studies of luminescent dye doped poly(methyl methacrylate) as solar concentrator. *J. Appl. Polym. Sci.* **74,** 3316–3323 (1999).

12. Ballato, J., Foulger, S. H. & Smith, Jr., D. W. Optical properties of perfluorocyclobutyl polymers. II. Theoretical and experimental attenuation. *J. Opt. Soc. Am. B* **21,** 958 (2004).

13. Sansregret, J., Drake, J. M., Thomas, W. R. L. & Lesiecki, M. L. Light transport in planar luminescent solar concentrators: the role of DCM self-absorption. *Appl. Opt.* **22,** 573 (1983).

14. Goldschmidt, J. C. *et al.* Theoretical and experimental analysis of photonic structures for fluorescent concentrators with increased efficiencies. *Phys. status solidi* **205,** 2811–2821 (2008).

15. Verbunt, P. P. C. *et al.* Controlling Light Emission in Luminescent Solar Concentrators Through Use of Dye Molecules Aligned in a Planar Manner by Liquid Crystals. *Adv. Funct. Mater.* **19,** 2714–2719 (2009).

16. Zastrow, A. The physics and applications of fluorescent concentrators: A review. in *Opt. Mater. Technol. Energy Effic. Sol. Energy Convers. XIII* (Wittwer, V., Granqvist, C. G. & Lampert, C. M.) 534–547 (International Society for Optics and Photonics, 1994). doi:10.1117/12.185397

17. Mansour, A., El-Shaarawy, M., El-Bashir, S., El-Mansy, M. & Hammam, M. Optical study of perylene dye doped poly(methyl methacrylate) as fluorescent solar collector. *Polym. Int.* **51,** 393–397 (2002).

18. Reisfeld, R. Prospects of sol–gel technology towards luminescent materials. *Opt. Mater. (Amst).* **16,** 1–7 (2001).

19. Batchelder, J. S., Zewail, A. H. & Cole, T. Luminescent solar concentrators. 2: Experimental and theoretical analysis of their possible efficiencies. *Appl. Opt.* **20,** 3733–54 (1981).

20. Du, H. *et al.* Optical Properties of Colloidal PbSe Nanocrystals. *Nano Lett.* **2,** 1321–1324 (2002).

21. Lomascolo, M., Cretì, A., Leo, G., Vasanelli, L. & Manna, L. Exciton relaxation processes in colloidal core/shell ZnSe/ZnS nanocrystals. *Appl. Phys. Lett.* **82,** 418 (2003).

22. Sark, W. G. J. H. M. van *et al.* Luminescent Solar Concentrators - A review of recent results. *Opt. Express* **16,** 21773 (2008).

23. Duarte, F. J. Organic Dye Lasers: Brief History and Recent Developments. *Opt. Photonics News* **14,** 20 (2003).

24. Long, L. *et al.* A coumarin-based fluorescent probe for biological thiols and its application for living cell imaging. *Org. Biomol. Chem.* **11,** 8214–20 (2013).

25. Zhao, Y., Meek, G. A., Levine, B. G. & Lunt, R. R. Near-Infrared Harvesting Transparent Luminescent Solar Concentrators. *Adv. Opt. Mater.* **2,** 606–611 (2014).

26. Weil, T., Vosch, T., Hofkens, J., Peneva, K. & Müllen, K. The rylene colorant family--tailored nanoemitters for photonics research and applications. *Angew. Chem. Int. Ed. Engl.* **49,** 9068–93 (2010).

27. Melucci, M. *et al.* Silk doped with a bio-modified dye as a viable platform for eco-friendly luminescent solar concentrators. *RSC Adv.* **2,** 8610 (2012).

28. Baumberg, I. *et al.* Effect of polymer matrix on photo-stability of photo-luminescent dyes in multi-layer polymeric structures. *Polym. Degrad. Stab.* **73,** 403–410 (2001).

29. Amdursky, N., Erez, Y. & Huppert, D. Molecular rotors: what lies behind the high sensitivity of the thioflavin-T fluorescent marker. *Acc. Chem. Res.* **45,** 1548–57 (2012).

30. López-Duarte, I., Vu, T. T., Izquierdo, M. A., Bull, J. A. & Kuimova, M. K. A molecular rotor for measuring viscosity in plasma membranes of live cells. *Chem. Commun. (Camb).* **50,** 5282–4 (2014).

31. Sanguineti, A. *et al.* High Stokes shift perylene dyes for luminescent solar concentrators. *Chem. Commun. (Camb).* **49,** 1618–20 (2013).

32. Langhals, H. & Hofer, A. Controlling UV/vis absorption and Stokes shifts in highly fluorescent chromophores by molecular dynamics in targeted construction of dyads. *J. Org. Chem.* **77,** 9585–92 (2012).

33. Li, C. *et al.* Rainbow perylene monoimides: easy control of optical properties. *Chemistry* **15,** 878–84 (2009).

34. Zoon, P. D. & Brouwer, A. M. A push-pull aromatic chromophore with a touch of merocyanine. *Photochem. Photobiol. Sci.* **8,** 345–53 (2009).

35. H�ckel, E. Quantentheoretische Beitr�ge zum Benzolproblem. *Zeitschrift f�r Phys.* **70,** 204–286 (1931).

36. Reetz, M. T., H�tte, S., Goddard, R. & Minet, U. Tetrabutylammonium salts of carbazole and dibenzoazepine: synthesis, crystal structures and use in anionic polymerization. *J. Chem. Soc. Chem. Commun.* 275 (1995). doi:10.1039/c39950000275

37. Feiler, L., Langhals, H. & Polborn, K. Synthesis of perylene-3,4-dicarboximides — Novel highly photostable fluorescent dyes. *Liebigs Ann.* **1995,** 1229–1244 (1995).

38. Nagao, Y., Abe, Y. & Misono, T. Synthesis and properties of N-alkylbromoperylene-3,4-dicarboximides. *Dye. Pigment.* **16,** 19–25 (1991).

39. Liégault, B., Lapointe, D., Caron, L., Vlassova, A. & Fagnou, K. Establishment of broadly applicable reaction conditions for the palladium-catalyzed direct arylation of heteroatom-containing aromatic compounds. *J. Org. Chem.* **74,** 1826–34 (2009).

40. Surry, D. S. & Buchwald, S. L. Dialkylbiaryl Phosphines in Pd-Catalyzed Amination: A User's Guide. *Chem. Sci.* **2,** 27–50 (2011).

41. *Electroanalytical Methods: Guide to Experiments and Applications*. **28,** 359 (Springer Science & Business Media, 2009).

42. Wilson, L. R. Luminescent solar concentrators : a study of optical properties, re-absorption and device optimisation. (2010). at <http://www.ros.hw.ac.uk/handle/10399/2336>

43. Rowan, B. C., Wilson, L. R. & Richards, B. S. Advanced Material Concepts for Luminescent Solar Concentrators. *IEEE J. Sel. Top. Quantum Electron.* **14,** 1312–1322 (2008).